Charged Vector Boson ($W^{\pm}$) production in simulated proton-proton collisions at $\sqrt{s} = 5.36$ TeV.

Author: Stephan Potgieter

Supervised by: Prof. Zinhle Buthelezi, Dr. Siegfried Förtsch, Ass. Prof. Thomas Dietel

2025

Abstract

In this work, the focus is on the charged vector boson ($W^{\pm}$) production in the forward rapidity region of simulated relativistic proton-proton collisions, where the POWHEG and Pythia Monte Carlo (MC) event generators are used to simulate the events of interest for the analysis. The $W^{\pm}$ boson production is studied via the muonic decay channel as $W^{\pm} \rightarrow \mu^{\pm} + \overset{(-)}{\nu}_{\mu}$. It is theoretically motivated in the work that this process can serve as a probe of the initial state of the collision, since the $W^{\pm}$ boson is produced in the hardest partonic interaction and neither the $W^{\pm}$ boson nor the $\mu^{\pm}$ have a colour charge. The muonic decay of heavy-flavour (HF) mesons in the same forward rapidity region is also investigated, where it is shown that these processes serve as the dominant background for the muon production from $W^{\pm}$ boson decays. The primary charged-particle multiplicity is also introduced as an observable of interest, where the self-normalised $W^{\pm}$ boson production as a function of the normalised multiplicity is defined and studied specifically. For this observable, it is shown that a linear trend is obtained when estimating the multiplicity in the central rapidity region and using the default Monash Tune. The choice of the central region for the multiplicity estimation is clearly motivated by looking at auto-correlation effects - which are shown to effect the slope of the multiplicity observable. In addition, it is shown that the slope of the multiplicity observable is also sensitive to the multi-parton interaction (MPI) and colour reconnection (CR) models - which motivates the use of the observable to probe the initial-state of the collision. Finally, a feasibility study is also performed to investigate whether the same study can be done with the ALICE Run 3 proton-proton reference data at the same centre-of-mass energy - where an estimation of the available statistics for the $W^{\pm} \rightarrow \mu^{\pm} + \overset{(-)}{\nu}_{\mu}$ process is presented. Through the work, it is also argued that the study in proton-proton collisions can serve as a meaningful baseline measurements for other collision systems - such as proton-lead and lead-lead.

Contents

Acknowledgements

This work is dedicated to all of my friends and loved-ones. I would not have been able to reach this point in my career without their unwavering support and unconditional love. With a special mention to my parents, who have always encouraged me to pursue my interests and embrace myself for who I am, without any judgement.

I would also like to thank my co-supervisors, Prof. Zinhle Buthelezi and Dr. Siegfried Förtsch, for taking me under their wing without any hesitation and guiding me through this project with patience and kindness. The thanks can also be extended to the whole South Africa ALICE group, for their commitment to our research and providing support in a variety of ways.

A special mention to Ass. Prof. Thomas Dietel, who presented me with the opportunity to enter this field and participate in international research. As well as being willing to continue providing support as a supervisor, despite no longer being officially contracted by the university.

A shout-out to my fellow University of Cape Town postgraduate students, who were always willing to lend an ear during lunch times and coffee breaks. Their understanding and wisdom served as a boost of confidence and energy during the most challenging of times.

Finally, I would like to thank the South Africa CERN group (under the Department of Science, Technology and Innovation) for their continued support in providing the financial and administrative basis to pursue my dreams of pursuing scientific research. I am deeply honoured to represent my beautiful country in the scientific domain and hope to one day give back, by providing others with the same opportunities I have received.

1 Introduction

1.1 Aim of the Analysis

1.1.1 Approach and Layout

The aim in this work is to simulate and analyse in-elastic processes in relativistic proton-proton collisions, with a specific focus on the production of muons from the leptonic decay of the Charged Vector Boson ($W^{\pm} \rightarrow \mu^{\pm} + \overset{(-)}{\nu_{\mu}}$). The dominant background for this process will be from the semi-leptonic decays of mesons containing charm and bottom quarks. The processes of interest will be mainly studied in the forward rapidity region ($2.5 < y < 4.0$) of the collision, since the ALICE Muon Spectrometer is located in this region for the experimental measurement of the production of decay muons. The simulated proton-proton collisions will be considered at the centre-of-mass energy of the proton-proton reference runs during the Large Hadron Collider's (LHC) Run 3 data-taking period at $\sqrt{s} = 5.36$ TeV, where $\sqrt{s} = 5.02$ TeV will also be included in some cases to compare to results from Run 2 data. For the simulations, both POWHEG and Pythia will be used - with the Monash 2013 Tune set in most cases.

In this section, the physics motivations of the study will be introduced. In section 1.2, a more detailed introduction of the relevant physics background and context will be given. To also provide experimental context, the ALICE detector and physics motivations of the collaboration will be briefly introduced in section 1.3. After this, the more theoretical aspects of the fundamental physics processes and proton-proton collision models will be discussed in sections 2.1 and 2.2, respectively. To move in the direction of the analysis results, the relevant software and configurations used will firstly be discussed in section 3. Finally, all of the obtained results and interpretations thereof will be presented in section 4 - after which the work will be concluded in section 5.

1.1.2 Physics Motivation

The core process that will be studied in this work, namely $W^{\pm} \rightarrow \mu^{\pm} + \overset{(-)}{\nu_{\mu}}$, is physically interesting for a variety of reasons. The most notable is that it is always produced during the hard partonic scattering stage of the collision, where it will still be motivated that this can be analytically calculated with perturbation theory. Since the products of the process also carry no colour charge, there will be no other non-perturbative QCD effects involved in this process - making it a "clean" probe of properties of the initial state of the collision. Thus, studying this process is also physically meaningful in proton-lead and lead-lead collisions, where the study in proton-proton collisions can serve as a meaningful baseline measurement - to aid in isolating initial-state model effects.

The main observable of interest will be the normalised charged-particle multiplicity dependence of the self-normalised production of muons from $W^{\pm}$ boson decays, which will be defined more clearly in section 4.3.3. Contrary to the $W^{\pm} \rightarrow \mu^{\pm} + \overset{(-)}{\nu_{\mu}}$ process, the charged-particle multiplicity production is dominated by non-perturbative QCD processes - such as hadronic showers. Thus, when aiming to capture the physics of the full collision event, models are required that can not be derived from first principles - such as multi-parton interactions (MPI) and colour reconnections (CR). It will be motivated in this work that studying the $W^{\pm}$ boson production as a function of the charged-particle multiplicity can aid in constraining these models.

1.1.3 Outlook for Data Analysis

In ALICE, the charged vector boson production in the forward rapidity region ($2.5 < y < 4.0$) has already been experimentally measured in proton-lead and lead-lead collisions at $\sqrt{s} = 5.02$ TeV, using the Run 2 data [1] - expanded on in section 1.3. With the ongoing Run 3 data-taking period, which is at slightly higher centre-of-mass energies and larger luminosities than Run 2 for each respective collision system. This provides the opportunity to study the mentioned processes of interest in proton-proton, proton-lead and lead-lead collisions - with more statistics available than before. Thus, this work will also serve as a feasibility study, where the possibility of performing the same analysis with Run 3 data from the ALICE Muon Spectrometer will be investigated. An estimation of the available statistics in the collected Run 3 proton-proton reference data at $\sqrt{s} = 5.36$ TeV will be done - where the available recorded data in ALICE is shown in Figure 1. As already mentioned, the analysis of proton-proton collisions at this energy can also serve as a reference study for the same analysis to be done in proton-lead and lead-lead collisions at the same centre-of-mass energy - which will be further motivated and emphasized throughout the work.

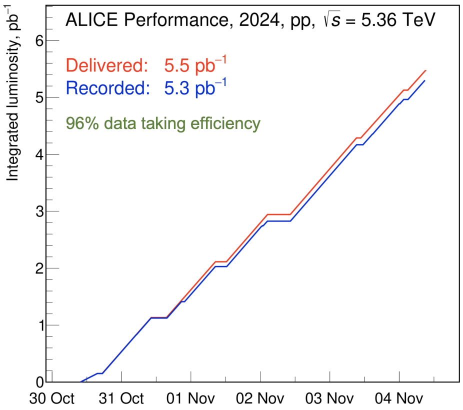

Figure 1: Integrated luminosity of recorded proton-proton reference data at $\sqrt{s} = 5.36$ TeV in ALICE during the Run 3 data-taking period [2].

1.2 Physics Background and Context

1.2.1 Standard Model of Particle Physics

One of the biggest achievements of modern day physics is the Standard Model of Particle Physics, as it can successfully describe nearly all of the current experimental data [3] - to the extent that the theory can be successfully applied to be meaningfully compared to data. The Standard Model aims to mathematically describe and make quantitative predictions about the matter and interactions which are observable and measurable in our universe, via the interaction of fundamental particles and forces.

The four known fundamental forces are namely the electromagnetic, weak nuclear, strong nuclear and gravitational forces [3]. The first three forces, respectively, form part of the Standard Model and are described mathematically via quantum field theories (QFTs), which are well established mathematical descriptions to unify quantum mechanics and special relativity. The gravitational force is mathematically described via general relativity and is not yet incorporated into the Standard Model, which is one of the biggest ongoing problems in modern physics today. There are many attempts at beyond Standard Model theories currently under investigation by both theoretical and experimental physicists, with the hope to unify gravity with the rest of the Standard Model description. The influence of gravity will not be of much relevance in this thesis, as the focus will be on the interactions of fundamental particles at high energies - where the gravitational force can be considered negligible [3].

As depicted by the Standard Model in Figure 2, the fundamental particles are divided into two groups - fermions and bosons. For the fermions, the quark and lepton sub-groups are made up of six fundamental particles each - which are known as the different “flavours”. The fermion sub-groups can also be divided into associated pairs known as the “generations”. The first generation, namely the electron and electron-neutrino for the leptons, are the lightest of the group and therefore also the most stable. The “heavier” generations are less stable and will have a “short” lifetime of decaying into a lighter and more stable generation [4]. For example, the electroweak decay of the charm quark into the down quark (also emitting a lepton and neutrino) will be of relevance in the analysis of Heavy-Flavour (charm and bottom) quarks - discussed in section 1.2.5.

In Table 1 it is shown which of the three Standard Model forces act on which of the groups of fermions.

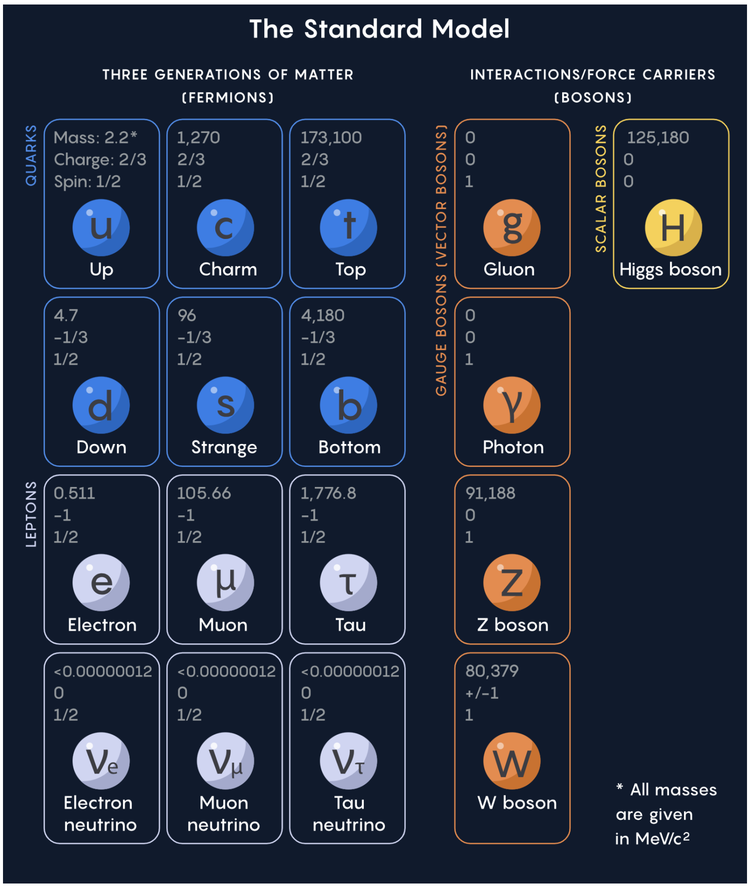

Figure 2: Standard Model of Particle Physics [5].

The quarks are the only fermions that carry a "colour" charge, which is the conserved quantity given by the symmetry of the strong interaction. This is mathematically modelled and described by the QFT known as Quantum Chromo Dynamics (QCD) - the finer theoretical details of relevance in this work will be discussed later in section 2.1.4. Due to the nature of the strong interaction, quarks are always found in nature as colourless bound states (referred to as confinement) known as hadrons, which can be further sub-divided into mesons (two valence quarks) and baryons (three valence quarks). At very high energy and temperature densities, the quarks can undergo de-confinement to form what is known as the Quark-Gluon Plasma (QGP) [6] - the study of this phenomenon will not be a focus in this work.

Unlike the quarks, the leptons do not experience the strong interaction and lepton-neutrinos have no net electric charge, so they do not experience the electromagnetic interaction either. In the classical representation of electromagnetism, the electrostatic force is a conservative vector field that is described as the gradient of an electric scalar potential. However, this representation does not account for the observed interaction of electrons scattering off the electrostatic potential of a proton nucleus, where there is a transfer of momentum that seemingly happens "at a distance" [3]. In the context of the standard model, the electromagnetic force is described by the QFT known as Quantum Electrodynamics (QED) - where the force is explained through the interaction and exchange of fundamental particles.

The weak interaction was developed in order to describe the observed phenomenon of β-decay in radioactive isotopes, as well as fusion processes that fuel stars in the universe - this is described by the QFT known as Quantum Flavour-Dynamics (QFD). In 1979, the nobel prize in physics was shared by Glashow, Salam and Weinberg for unifying the electromagnetic and weak interaction into a single theory, the electroweak

Table 1: The Fundamental Forces experienced by the Fermions.

	Strong	Electromagnetic	Weak
Quarks	×	×	×
Charged Leptons		×	×
Neutrino Leptons			×

interaction [7] - this will also be discussed in more detail in section 2.1.3.

The Standard Model forces mentioned thus far are mediated through the exchange of the "force-carrier" fundamental particles - known as the bosons. The most well-known boson classically is the photon, which is the mediating particle of the electromagnetic interaction. The exchange of a photon, described by QED, succeeds in explaining the interaction "at a distance" mentioned previously in the example of an electron scattering off a nucleus. The gluon was discovered experimentally in 1979 at the DESY laboratory in Germany, after being postulated theoretically around 1962, and serves as the mediating particle of the strong interaction [8]. The name given to these bosons refers to how they "glue" quarks together into colourless hadronic bound states as mentioned before. The Higgs boson was announced as a discovery by CERN on 4 July 2012, which makes it the most recent addition to the Standard Model of particle physics. The Higgs field is responsible for the interaction that gives other particles their mass, known as the Brout-Englert-Higgs mechanism [9] - for which the Nobel prize in physics was awarded in 2013 [10]. There are many ongoing experimental studies to understand the Higgs boson and its properties better, which will not be of relevance in this work.

The only bosons left to talk about are those that mediate the weak interaction, namely the $W^{\pm}$ and Z^0 bosons. The discovery of the charged vector boson ($W^{\pm}$) was announced by CERN on 25 January 1983. Being the only boson that has an electric charge (either +1 or -1), it has the unique property of changing the flavour of the fermions - making it responsible for many of the observed nuclear processes in the universe. For example, the burning of stars to create heavier elements that are emitted into space when the star dies. This allows for the formation of planets - and even humans [11]! Studying the production of the charged vector boson in proton-proton collisions will be a central focus in this work, which will be discussed in more detail in section 1.2.6.

1.2.2 High-energy Collider Experiments

It was mentioned in the previous section that the Standard Model can describe the currently available experimental data fairly well. In this section, the set-up of the main experiments that produce the data which is used to test the Standard Model's theoretical predictions will be briefly discussed. The focus will be on collision experiments that probe the high-energy regime, as this is also the physics context of interest in this work.

When it comes to nuclear and particle physics, two of the main methods of experimentation are namely fixed-target and particle-particle collision experiments [3]. In the case of fixed-target experiments, a beam of particles (leptons or hadrons) are fired with some set energy at a stationary target, to observe how the beam interacts with the target nuclei - for example, measuring the scattering angles by which the beam particles are deflected off the target. One of the important fixed-target experiments in the history of the Standard Model is the MIT-SLAC experiment, where a beam of electrons (with an energy of up to 20 GeV) was fired at a target of liquid hydrogen (and later also deuterium) [12]. By measuring the energies and angular distributions of the scattered electrons from the target, they were able to observe that the electrons were scattering off a hard "core" inside the fixed-target hadrons. After excluding other interpretations, this served as evidence that protons/neutrons are made up of constituents that we now know as quarks. This was later awarded the Nobel prize for physics in 1990, which was shared by Jerome I. Friedman, Henry W.

Kendall and Richard E. Taylor [13].

The analysis in this work will be focused on simulated proton-proton collisions at a centre of mass energy of 5.36 TeV. This is an example of a particle-particle collision, where two beams of either leptons or hadrons are accelerated with electric fields in opposite directions and then "steered" with magnetic fields to overlap and collide with each other. The advantage this has over fixed-target collisions is that each beams carries an energy (large momentum from being accelerated), which allows for a higher interaction energy in the centre-of-mass frame of the collision. When the goal is to investigate interactions at relativistic energies, this is clearly the experimental method of choice. The centre-of-mass energy of the collision $\sqrt{s}$ is given by taking the square-root of the Lorentz-invariant quantity s, which is calculated from the energy (E) and momentum ($\vec{p}$) of the interacting initial-state beam particles as [3],

$$s = \left(\sum_{i=1}^{2} E_i\right)^2 - \left(\sum_{i=1}^{2} \vec{p}_i c\right)^2 . \tag{1}$$

In order to create massive particles, like the vector boson that has a mass of approximately 80 GeV/c^2 (as seen in Figure 2), it is clear that collisions at ultra-relativistic centre-of-mass energies are required to produce these heavier particles to study them. The Large Hadron Collider (LHC) at CERN [14] is the accelerator that has managed to reach the highest laboratory interaction energies in history, currently colliding protons at $\sqrt{s} = 13.6$ TeV and lead-ions at $\sqrt{s} = 5.36$ TeV. This is achieved by accelerating the two beams in opposite directions in separate beam pipes, which are tubes kept at an ultra-high vacuum. These beam pipes form a ring that is 27-kilometres in diameter and are surrounded by superconducting magnets (cooled down to -271.3°C with liquid helium) and accelerating devices.

In order to detect information about the collisions and gather the data for physics analysis, the LHC has four main detectors that are located at the interaction points of the particle beams. Each detector is associated with a different experiment, where the structure of the detector is designed to suit the physics objectives of the experiment. One of the most famous is the ATLAS (A Toroidal LHC Apparatus) experiment [15], which was jointly responsible for the discovery of the Higgs boson that was mentioned in the previous section. The ATLAS experiment can be viewed as a general-purpose particle physics experiment, where much of the focus is on studying the top quark and Higgs boson - as well as beyond standard model physics. The CMS (Compact Muon Solenoid) experiment has mostly the same physics goals and shared the Higgs boson discovery with ATLAS, where the main differences between the two experiments are with technical aspects of the detector design [15]. The LHCb (Large Hadron Collider beauty) experiment [16] specializes in studying the bottom quark, with the overarching physics goal of investigating the matter/anti-matter asymmetry that is observed in the universe. The physics goals and detector design of ALICE (A Large Ion Collider Experiment) [17] will be the main experiment of importance in this work. Thus, it will be discussed separately in more detail in section 1.3.

The LHC is designed to accelerate and collide hadrons, which are bound states of quarks and gluons. Protons are the lightest form of hadrons that are collided at the LHC, where proton-proton collisions form the largest part of the LHC beam time. Lead nuclei are the heaviest hadrons that are collided at the LHC, where the combination with protons is referred to as proton-lead collisions. The 27-kilometre long tunnel that now houses the LHC was originally used for the Large Electron-Positron Collider (LEP) [18], where electrons and positrons (leptons) were the beams that were being collided in order to study the electroweak interaction. Clearly, there are many different collision systems of choice when performing a high-energy collision experiment, where the initial state and resulting physics of each system will be different. For example, when moving from lepton to hadron collisions, colour charge is introduced into the initial state of the collision. Hadron collision models also require input from Parton Distribution Functions (PDFs) in order to relate the momentum of the individual quarks/gluons (partons) to the momentum of the bound hadron [19]. Within the context of hadron collisions, moving from the smaller system size of proton-proton collisions to larger systems such as lead-lead collisions also introduces many additional complexities to the system. The modelling of the initial state and evolution of hadronic collision systems will be a key concept in this work, where the focus will be on proton-proton collisions. It will be discussed in more detail in section 2.2.

1.2.3 Production Cross Section

In order to understand how meaningful information is extracted from the mentioned collider experiments to compare with the theoretical predictions of the Standard Model, it is necessary to look at some of the commonly used and relevant observables. It is important to mention that a lot of the physics that happens during the collision is "hidden" to the detectors, since the interactions happen at such small distance and time scales. Thus, the possible observables are limited to what can be inferred from the particles that are long-lived enough to reach the detectors. Constructing meaningful and interesting observables from the detectable particles of the collision is an important task of both experimental and theoretical high-energy physicists. In the following sections, the main observables of interest in this work will be discussed.

The most obvious one is the production cross-section (σ) of a process of interest. Due to the quantum mechanical nature of the collision, it is necessary to measure average rates or relative probabilities of processes rather than "exact" quantities. The cross-section is thus defined as a measure of the quantum mechanical probability for the process of interest to occur, which depends theoretically on the the fundamental physics involved in the Feynman diagrams that contribute to the process [[3], p.26] - this will be discussed in more detail in section 2.1. The cross-section has units of barns, which is just a unit of area given by 10^{-28} m^2. This can be interpreted as an "effective" area of a target for the incoming particle beam to pass through and then interact [20]. Thus, a larger cross-section corresponds to a larger "effective" area, which can be interpreted as a larger probability for the process to occur. The reason the cross-section is defined in this way is theoretically motivated and will be discussed more in section 2.1.2.

In the context of a collision experiment, the number of expected occurrences of a process of interest can then be determined as [20],

$$N_{occur} = \sigma_{process}\,\mathcal{L}_{int} \tag{2}$$

where $\mathcal{L}_{int} = \int \mathcal{L}\,dt$ is the integrated luminosity of the performed collisions. When many collisions of the target beams are performed, each bunch crossing between the particle beams is known as an 'event'. The experimental rate of events that occur per unit time is given by the instantaneous luminosity ($\mathcal{L}$), which has units of inverse barns. As already shown, the integrated luminosity can then be determined by integrating the instantaneous luminosity over the full time interval of the running of the collision experiment. In real-life experiments, the luminosity can be measured in different ways, where one of the common methods is known as a van der Meer scan (vdM) - named after the inventor of the method [20]. This is the method of choice in all the mentioned LHC experiments, where it can also be used to determine the beam sizes at the interaction point in addition to an absolute measurement of the luminosity [21].

In this work, the focus will be on the theoretical/computational simulation of proton-proton collisions. In this context, the concept of luminosity is not well defined, as the rate of collisions is not a physical parameter here. The number of simulated events per unit time is proportional to the available computational resources, where events are simulated in isolation from one another. In this work, computational methods will even be employed to generate independent events at the same time in parallel - this will be discussed in more detail in section 3. One of the aims of the simulations will be to numerically determine the cross-sections of processes of interest from the current theoretical models - which will comprise some of the core results presented in this study. In contrast, in real-life experiments the cross-sections can not be measured directly. The main goal is thus to measure the number of events of interest and from this obtain the measured cross-section as shown in equation 2, which can then be compared to the theoretical cross-sections - after accounting for detector effects. The production cross-section of a process will depend on the collision system and centre-of-mass energy of interest. Thus, it needs to be uniquely determined for each case.

1.2.4 Charged-Particle Multiplicity

Another important observable to discuss in the context of this work, is the primary charged-particle multiplicity of an event. The definition is quite straight-forward and intuitive in the theoretical/simulation context, it is merely the count of primary charged particles in the final state that are produced in an event of interest. The charged-particle multiplicity is a physically interesting observable to look at in proton-proton collisions, as it provides information about underlying mechanism/models of the collision, like properties of the initial-state - exploring this will be at the heart of this work. For example, in Figure 3 it is shown how the simulated distribution of the charged-particle multiplicity in proton-proton collisions strongly depends on the inclusion of two of the underlying mechanisms currently used to model these collisions - namely multi-parton interactions (MPI) and colour reconnections (CR). Investigating the effects of these mechanisms will be a focus in this work, so their technical aspects will be discussed in more detail in section 2.2.

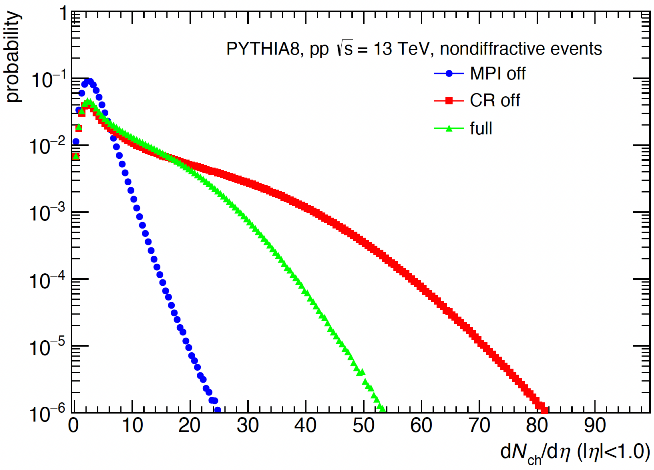

Figure 3: The primary charged-particle multiplicities at mid-rapidity ($|\eta| < 1$) in simulated proton-proton collisions, at $\sqrt{s} = 13$ TeV with Pythia using the full Monash Tune - showing the effects of turning off MPI and CR [22].

In the experimental context, the primary charged-particle multiplicity can be estimated, but there are restrictions given by the acceptance regions of the detectors. Thus, in this work the ALICE definition of primary charged-particles [23] specifically will be followed in order to make simulated predictions that can be compared with experimental results from ALICE. This definition is primarily based on the lifetime of the charged particles, as short-lived charged particles will decay before reaching the detector responsible for estimating the multiplicity, and charged particles that originated as decay products from long-lived particles will only be produced outside the range of the detector. How this is implemented will be discussed in more detail in section 4.2.2. In Figure 4, it is shown how the amplitude from the V0M detector in ALICE can be used to estimate the primary charged-particle multiplicity classes in the forward rapidity region, where the comparison to the theoretical prediction from Pythia is also given.

In the context of heavy-ion collisions, the charged-particle multiplicity can also be used to investigate the initial-state parameters of the collision. As the nuclei of heavy-ions are made up of multiple protons and neutrons, they are larger and more complicated to model than protons. For example, the degree of geometric overlap of the nuclei as they collide (known as centrality) and the number of binary nucleon-nucleon interactions become important parameters to consider. As heavy-ion collisions are not a central

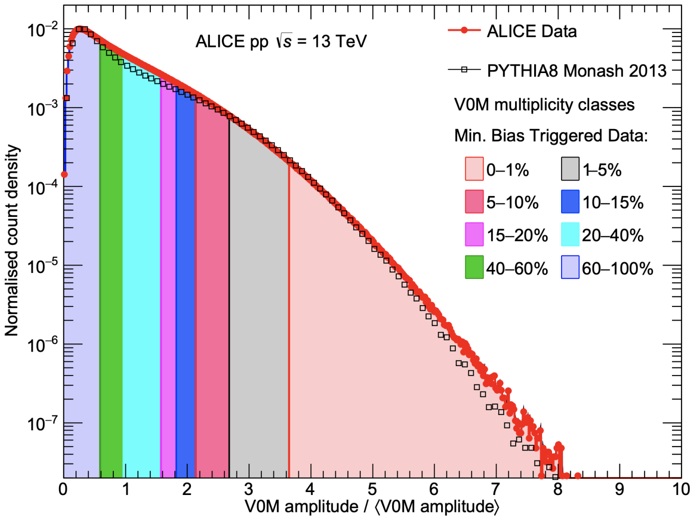

Figure 4: The scaled V0M distribution in proton-proton collisions at $\sqrt{s} = 13$ TeV in ALICE, compared to the theoretical prediction given by Pythia [24].

focus in this work, the technicalities will not be discussed in much more detail. It only needs to be noted that a multiplicity study done in proton-proton collisions can serve as a reference for a similar study in heavy-ion collisions, as it can give insight into how the initial state changes when moving from a smaller to larger hadronic collision system.

1.2.5 Heavy-Flavour Quarks

The charm and bottom quarks, two of the standard model quarks shown in Figure 2, are collectively known as the Heavy-Flavour (HF) quarks. As these two quarks are not found as valence quarks in protons or neutrons, they are produced as products of QCD processes in high-energy collisions. Due to their masses being much larger than the other light quarks (up, down, strange), the centre-of-mass energy of the collision needs to be large enough for them to be produced in a significant amount. Having a larger mass also leads to the advantage that the production cross-section can by calculated theoretically using perturbative QCD - excluding the low p_T limit as will be shown in section 2.1.4. It can also be seen in Figure 2 that the top quark has a mass on the order of 10^2 times more than the HF quarks, making it the heaviest fundamental particle. Thus, it is studied separately from the HF quarks and will not be considered in this work.

In Figure 5, it is shown how the production cross-section of charm and bottom quarks scale with the centre-of-mass energy of proton-proton collisions. At the LHC energies of interest in this work, HF quarks are produced in "abundance" and can thus be used as a probe in proton-proton collisions to investigate interesting properties of the collision, such as hadronisation mechanisms (discussed more in section 2.2.5), and as a test for perturbative QCD [25]. Measuring HF production in proton-proton collisions can also serve as a reference baseline when studying their production in heavy-ion collisions. Since HF quarks have a colour charge, they are expected to interact with any strongly-interacting medium that is formed in the collision, such as the previously mentioned QGP. This makes them a great candidate to investigate how the production changes when moving from proton-proton to heavy-ion collisions, which can help give insight into the nature of the QGP.

As already mentioned for HF quarks, the production mechanisms can be calculated with perturbative QCD. In hadron-hadron collisions, at leading order (LO) the graphs are given as $q\bar{q} \rightarrow Q\bar{Q}$ and $gg \rightarrow Q\bar{Q}$; where q/g refer to quark and gluon partons of the colliding hadrons and $Q/\bar{Q}$ are the produced HF quark/anti-quark pairs. It is clear that the HF quarks are always produced in pairs at LO, where the pairs will be back-to-back in azimuthal angle to conserve momentum when the hard partonic scattering of the collision

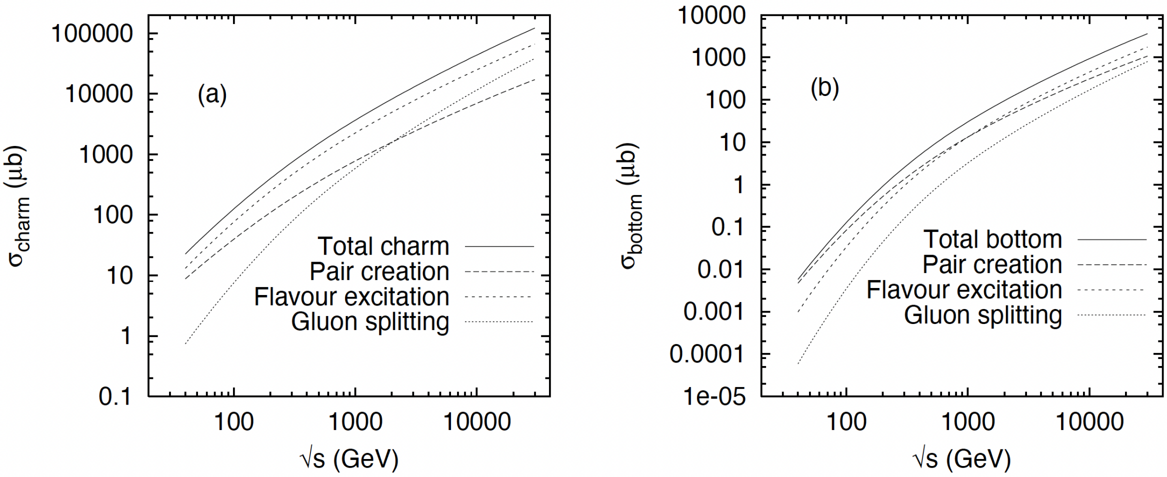

Figure 5: The production cross-section of charm (a) and bottom (b) quarks in proton-proton collisions as a function of the centre-of-mass energy, also showing the contributions from the different production mechanisms [25].

is one of the LO processes given - this is known as the pair creation class. With the available calculation tools in the Monte Carlo simulations of interest in this work, the next-to-leading order (NLO) approach of considering HF production mechanisms is not well suited. Instead, a parton-shower (PS) approach is used, where the partonic interaction processes of the colliding hadrons is subdivided into three stages: initial-state cascades, hard partonic scattering and final-state cascades. The initial and final state cascades then allow for two new classes of HF production, known as flavour excitation and gluon splitting [25]. In Figure 5, it is also shown how the three classes of HF production in the PS approach contribute to the total production of HF quarks, as a function of the centre-of-mass energy of the collision. The PS approach will be discussed in more detail in section 2.2.

It has already been mentioned that quarks are not observed or measured in isolation, but rather as bound states known as hadrons. The HF mesons, containing only a single HF valence quark, are known as D and B mesons for charm and bottom quarks, respectively. There are also mesons made up of two valence HF quarks known as Quarkonia, which are usually studied separately and will not be a focus in this work - the full list of known hadrons is listed in [26]. Since the production mechanisms for HF only explain how the quarks are produced in isolation, additional models are required to explain the hadronisation process from the stand-alone quarks into the colourless hadronic bound states. In this work, the Lund string fragmentation model implemented in Pythia will be used in the relevant simulations to describe the non-perturbative hadronisation - this model will be explained in more detail in section 2.2.5.

Due to the HF hadrons being short-lived (D^+ has a decay length of approximately 311.8μm [26]), they are not directly measured in the detectors. Thus, it is necessary to look at the decay products of the HF hadrons. The full list of decay channels for the D/B mesons is also listed in [26], with their respective branching ratios. In this work the focus will be on the leptonic and semi-leptonic decay channels, where a lepton-neutrino pair is produced in both cases - as shown for the pure leptonic decay of a D^+ meson in Figure 6. It is important to mention that in the semi-leptonic case, a lighter hadron is also produced as a decay product. Thus, when a B meson decays semi-leptonically it can produce a D meson as a decay product that can in turn decay to produce another lepton-neutrino pair. This will be important when considering the inclusive production cross-section of HF hadrons.

In the context of ALICE, the decay leptons can be measured in different detectors that cover different rapidity regions. For example, in the central region it is possible to detect and identify electrons fairly

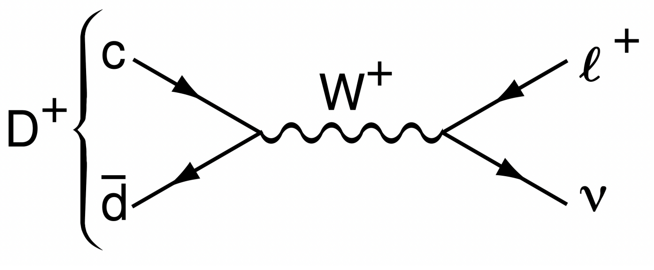

Figure 6: The Feynman diagram of the pure leptonic decay of D^+ meson [26].

accurately; whereas in the forward region muons can be identified and measured using the Muon Spectrometer - the ALICE detectors will be discussed in more detail in section 1.3.2. It is important to note that the neutrinos that are also produced can not be detected. Thus, the constructed HF analysis needs to infer all possible physics information of the HF hadrons from the decay leptons alone. In this work, the focus will be on muons produced in the forward region specifically. From now on, when talking about the HF$\rightarrow \mu$ production cross-section, it is specifically referring to the inclusive case of $c \rightarrow D \rightarrow \mu$, $b \rightarrow B \rightarrow \mu$ and $b \rightarrow B \rightarrow D \rightarrow \mu$. The HF$\rightarrow \mu$ production cross-section has already been measured by ALICE for proton-proton collisions at $\sqrt{s} = 5.02$ TeV during the Run 2 data taking period [27], which serves as the baseline measurement for heavy-ion collisions at the same energy - this will be an important reference in this work. It is important to investigate the HF production in the physics context of this work, as it will still be shown that it serves as the dominant background process when studying the charged vector boson production in the forward region, which will be discussed in the following section.

1.2.6 The Charged Vector Boson

The main focus of this work will be to study the production of charged vector bosons ($W^{\pm}$) in the forward region of the ALICE muon spectrometer. Due to their large mass of approximately 80 GeV/c^2, charged vector bosons are similarly produced in the hard partonic scattering of the collision and their production cross-sections can be calculated using perturbation theory up to next-to-next-to-leading-order (NNLO) [1]. Thus, measuring the experimental cross-section of $W^{\pm}$ boson production already serves as a good test for the theoretical calculations and models. At leading-order, the $W^{\pm}$ boson production is given by the quark and anti-quark annihilation process, as depicted in the left-most vertex of the diagram in Figure 7. Unlike the case of the Z^0 boson, the $W^{\pm}$ boson production mixes the flavour of the quarks. Thus, in high-energy proton-proton collisions the leading order production is dominated by the $u\bar{d} \rightarrow W^+$ and $d\bar{u} \rightarrow W^-$ processes [28] - as shown in Figure 8. It can also be seen in Figure 7 that there is a charge asymmetry that arises in the W^+ and W^- boson production at high centre-of-mass energies in proton-proton collisions, due to the uneven distribution of up/down quarks in the proton, which will be of physical interest. As also shown in Figure 7, the $W^{\pm}$ bosons can similarly decay to a lepton and neutrino pair as with the discussed case of HF hadrons. Thus, experimentally the muon spectrometer in ALICE can be used to estimate the production cross-section of $W^{\pm}$ bosons in the forward region, for which it will be shown that HF meson decays serve as the main contributing background.

Unlike the case of HF quarks discussed before, $W^{\pm}$ bosons have no colour charge and are therefore unaffected by the strong nuclear force. This means that their production should be independent of any of the soft-QCD processes in the collision, such as hadronisation mechanisms and colour-reconnection models. They will also not interact with any strongly-interacting medium that may be formed in the collision - such as the QGP in heavy-ion collisions. This makes $W^{\pm}$ bosons, that decay leptonically, excellent probes for the initial state of the collision. For example, since the charge ratio of the vector boson production will be sensitive to the distribution of quarks and gluons in the proton, this makes the $W^{\pm}$ boson a clean probe to study light quark PDFs at large energy scales of $Q^2 \approx M_W^2$ [6]. The theoretical electroweak input parameters for the $W^{\pm}$ boson cross-section (calculated to NNLO in perturbative-QCD) are also known to high accuracy, so the main uncertainty will arise from the input PDFs, making the $W^{\pm}$ boson cross-section sensitive to the

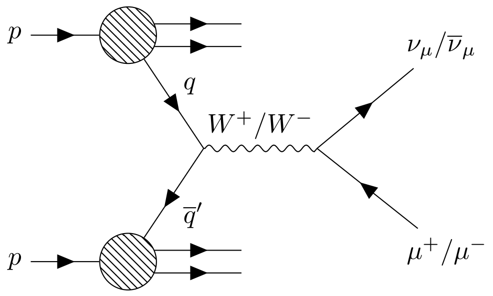

Figure 7: Diagram of the leading-order production and leptonic decay of a charged vector boson in a proton-proton collision.

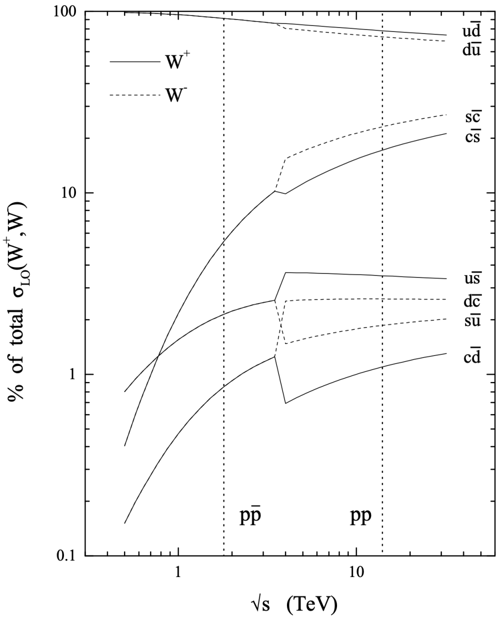

Figure 8: Production cross-sections of vector bosons in proton-proton and proton-anitproton collisions as a function of the centre-of-mass energy, showing the contributions from the different flavour partonic interactions [28].

PDF uncertainties [28]. The measurement of the $W^{\pm}$ boson production in the forward region can thus help to constrain the nuclear PDFs at small Bjorken-x in different collision systems, where Bjorken-x is simply the fraction of the proton's four-momentum carried by the interacting partons - which will be elaborated on in section 2.2.2. Improving the understanding of how the initial state changes from proton-proton to heavy-ion collisions is currently an important objective in the modelling of these collisions. It is known that PDFs of larger nuclei are significantly modified compared to free parton PDFs of protons. For example, nuclear PDFs at Bjorken-x $< 10^{-2}$ show a clear suppression compared to the proton PDFs - which is known as nuclear shadowing [6].

In section 1.2.4, it has already been shown how the primary charged-particle multiplicity distribution in simulated proton-proton collisions is affected by the inclusion of models such as MPI and CR. Since the $W^{\pm}$ boson is colour-neutral, it's production should not be sensitive to the effects of CR, but only to the initial-state effects and parameters such as MPIs. In Figure 9, it is shown how the self-normalised charged-particle multiplicity, in the central region, scales as a function of the self-normalised number of MPIs in simulated proton-proton collisions and vice-versa - with both the inclusion and exclusion of CR models in the simulation. Since it is not possible to experimentally measure the number of MPI, and since it has already been motivated that the vector boson production is sensitive to these initial state conditions, it is meaningful to study the production of vector bosons as a function of the charged-particle multiplicity - this will be one of the primary objectives in this work. This can aid in discerning how much the initial-state hard interaction scales contribute to the final state multiplicity of the collision.

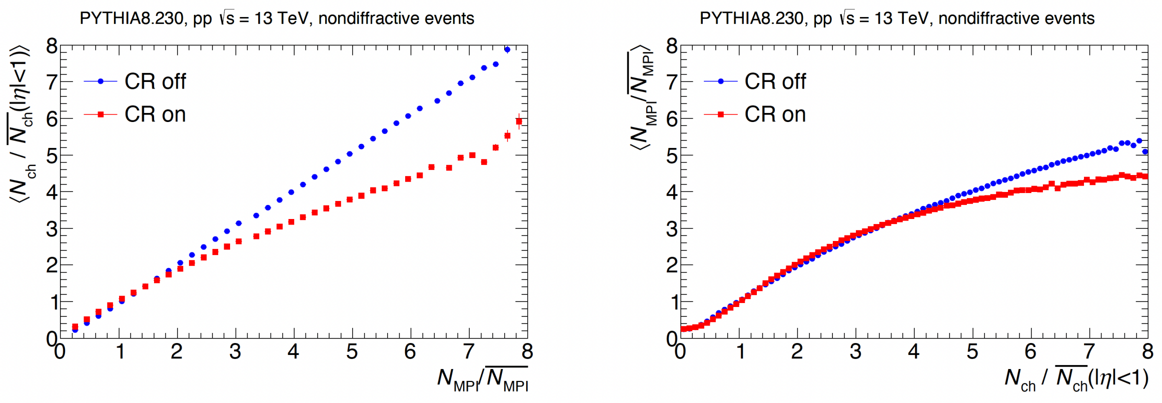

Figure 9: Self-normalised charged-particle multiplicity as a function of the self-normalised number of MPI in a simulated proton-proton collision at $\sqrt{s} = 13$ TeV shown on the left, and vice-versa on the right [22].

1.3 A Large Ion-Collider Experiment (ALICE)

It was motivated in section 1.1.3 that the simulation study presented in this work will also serve as a feasibility study for the analysis to be done with Run 3 data from the ALICE detector. Aspects of the ALICE detector will already be incorporated into the simulation analysis, such as the rapidity coverage of the relevant detectors. Thus, in this section ALICE will be briefly introduced, with a focus on the physics motivations of the experiment and a look at the relevant detectors. The section will closely follow what is laid out in [6], which provides a detailed summary of the history and progression of ALICE.

In Table 2, it shows a summary of all the data collected by ALICE for each collision system, during the LHC's Run 1 and 2 data-taking period. It is clear that the focus of ALICE goes beyond exclusively considering heavy-ion collisions, with data also being collected for proton-proton and proton-lead collisions - how this ties in with the physics objectives of the collaboration will be discussed next. The Run 3 data-taking period is currently still ongoing, where the proton-proton reference run at $\sqrt{s} = 5.36$ TeV has already been concluded - with the final collected statistics shown in Figure 1.

1.3.1 Physics Objectives and Results

In 1993, ALICE (A Large Ion Collider Experiment) was proposed as a LHC experiment. It was motivated as a dedicated experiment to study strongly-interacting matter at high temperatures and energy densities. The physics program was initially focused on studying the existence and properties of the Quark Gluon Plasma (QGP), as introduced in section 1.2.1. Later, this was extended to also cover a broader scope of observables related to studying QCD. As ALICE is the only LHC experiment dedicated to studying the QGP, it was specifically designed in a way to access observables in a wide p_T-range (from the soft-QCD to hard-QCD scales), with the goal to investigate the evolution of heavy-in collisions - from the initial stage to the observed hadronic matter, passing through the QGP phase.

In addition to heavy-ion collisions, physics studies in proton-proton collisions also formed a part of the ALICE program, which gained progressively more importance throughout the lifetime of the experiment. In the initial state of proton-proton collisions, nuclear effects are not relevant, as the number of participating

System	Year(s)	$\sqrt{s_{\mathrm{NN}}}$ (TeV)	L_{int}	N_{MB}
Pb–Pb	2010, 2011	2.76	75 $\mu\mathrm{b}^{-1}$	1.3×10^8
Pb–Pb	2015, 2018	5.02	800 $\mu\mathrm{b}^{-1}$	6×10^8
Xe–Xe	2017	5.44	0.3 $\mu\mathrm{b}^{-1}$	1.1×10^6
p–Pb	2013, 2016	5.02	18 nb^{-1}	8×10^8
p–Pb	2016	8.16	25 nb^{-1}	1.3×10^8
pp	2009	0.9	200 $\mu\mathrm{b}^{-1}$	0.5×10^6
pp	2011	2.76	100 nb^{-1}	1.3×10^8
pp	2010, 2011	7	1.5 pb^{-1}	1.6×10^9
pp	2012	8	2.5 pb^{-1}	3.1×10^8
pp	2015, 2017	5.02	1.3 pb^{-1}	10^9
pp	2015–2018	13	36 pb^{-1}	6×10^9

Table 2: Data collected by ALICE for different collision systems during the Run 1 and 2 data-taking period, showing the centre-of-mass energy for each respective collision system ($\sqrt{s_{NN}}$), integrated luminosity (L_{int}) and number of minimum-bias events (N_{MB}) [6].

nuclei is always two. This means that proton-proton collisions can provide many analysis opportunities to the ALICE physics program, such as serving as a reference for heavy-ion collisions and the study of QCD interactions in few-body systems. For example, it has already been mentioned in section 1.2.5 that measuring the HF cross-section can serve as a meaningful test for perturbative-QCD. In the same light, proton-lead collisions also play a role by serving as a reference system for heavy-ion collisions, where it is expected that some nuclear effects will be present without the formation of the QGP. In section 1.2.6, it was motivated that the $W^{\pm}$ boson can serve as a meaningful probe to aid in studying the role of the initial state in the different collision systems.

In ALICE, the electroweak bosons (which carry no colour charge) are used as probes in heavy-ion collisions to isolate the non-QGP effects in the initial-state, such as the nuclear-PDF and number of participating nucleons, from the QGP induced effects - as already motivated in section 1.2.6. For this, the $W^{\pm}$ and Z^0 boson productions have been measured by ALICE in the forward rapidity region with Run 2 data, for both proton-lead and lead-lead collisions [6]. Thus, performing the same measurement with the upcoming Run 3 data is an open opportunity in all collision systems. The production has also been measured in the central rapidity region of proton-proton collisions at $\sqrt{s} = 13$ TeV, via the electron decay channel - where the multiplicity dependence was also investigated [29]. The core result from the study is shown in Figure 10, where it is seen that a linear trend is obtained for the self-normalised electron production from $W^{\pm}$ decays as a function of the normalised charged-particle pseudorapidity density - which is accurately predicted by Pythia. This serves as an important reference in this work, as the same simulation study will be done for muonic decay channel ($W^{\pm} \to \mu^{\pm} + \overset{(-)}{\nu_{\mu}}$) in the forward rapidity region - at $\sqrt{s} = 5.36$ TeV using Pythia. The advantage that the study in this work provides, is that it can additionally serve as a reference measurement for lead-lead collisions at the same centre-of-mass energy. The feasibility study will then also be done, as an outlook to perform the same measurement with Run 3 data.

1.3.2 The ALICE Detector

The full ALICE detector, after the upgrades during the LHC long shutdown 2 (LS2), is shown in Figure 11. It is seen that the detector is comprised of many sub-detectors, where each serves a specific goal in the larger physics objective of the experiment. Most of the detectors cover the full polar angle, but are located in different rapidity regions w.r.t the beam axis. The central barrel, covering the $|\eta| < 0.9$ region, is designed to provide robust particle identification (PID) of tracks in the transverse momentum region of roughly $0.15 < p_T < 20$ GeV/c - as well as providing the capability to accurately determine primary and secondary vertices. The main detectors used for PID in the central barrel are the Inner Tracking System

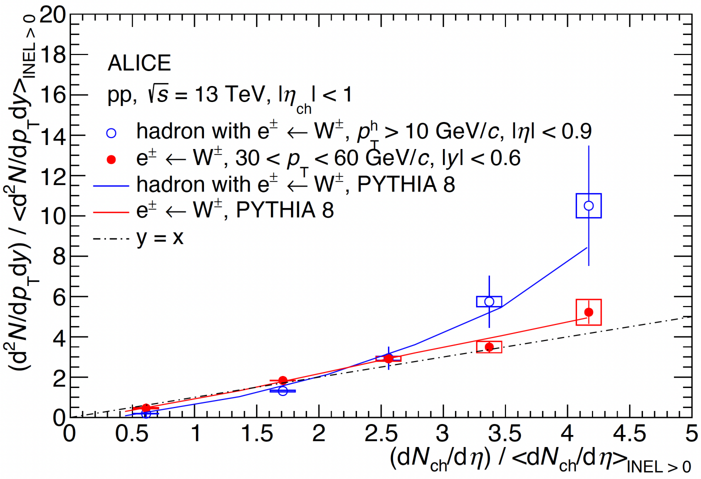

Figure 10: The self-normalised yields of $W^{\pm} \rightarrow e^{\pm}$ and associated hadrons as a function of the normalised charged-particle pseudorapidity density in the central region of proton-proton collisions at $\sqrt{s} = 13$ TeV, compared with the expectations from Pythia simulations - including both MPI and CR effects [29].

(ITS) and Time Projection Chamber (TPC), via the measurement of the specific energy loss (dE/dx) of charged-particles passing through the detectors. The Time Of Flight system (TOF) also compliments the PID by helping to distinguish between ambiguously identified tracks. The Transition Radiation Detector (TRD) also provides additional PID capabilities, with a focus on identifying electrons - which are challenging to distinguish from pions with the other mentioned PID detectors.

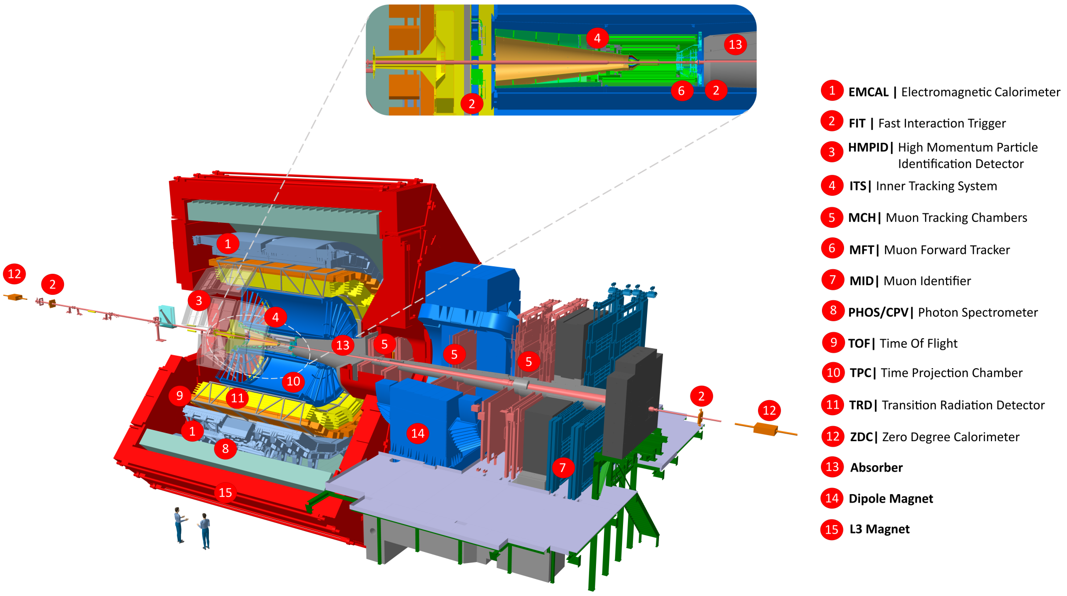

Figure 11: The ALICE Detector, after the upgrades for the Run 3 data-taking period [30].

The ITS 2 is made up of seven total tracking layers, which can be divided into the inner barrel with three layers and the outer barrel with two double layers [30] - which can be use to estimate the multiplicity in the central rapidity region ($|\eta| < 1.0$). To similarly estimate the charged-particle multiplicity in the forward rapidity regions and serve as a trigger, the Fast Interaction Trigger (FIT) detectors are used - which were introduced as an upgrade to the T0 and V0 detectors for Run 3 [30]. In this work, the forward rapidity region of the Run 2 V0C ($1.7 < \eta < 3.7$) will still be used merely to illustrate auto-correlations in 4.3.4 - this should not effect the physics of the results, as the multiplicity will be normalised. It is important to note that the rapidity coverage of the V0C overlaps with the Muon Spectrometer, which is located in $2.5 < \eta < 4.0$ - which will be relevant in section 4.3.4. The remaining ALICE detectors in the central region will not be of much relevance in this work. It is important to mention that the central barrel is surrounded by a L3 solenoid magnet, which provides a strong magnetic field of up to 0.5 Tesla - which is critically required to measure the momentum of electrically charged tracks.

The ALICE Muon Spectrometer is schematically shown in Figure 12, where the different categories of reconstructed muon tracks are also presented as an example. The Muon Spectrometer can be divided into four distinct parts. Starting from the left, which is closest to the interaction point, is the Muon Forward Tracker (MFT). The MFT was added as an upgrade during LS2 for Run 3, with the intention to improve the primary and secondary vertex finding for reconstructed muon tracks [30]. This upgrade was primarily required due to the Absorber, which is located between the MFT and the Muon Tracking Chambers (MCH). Even though the absorber is necessary to eliminate a lot of the hadronic background, it reduces the vertex finding and momentum resolution - through Coulomb scatterings of the muon tracks passing through the absorber. The MCH and Muon Identifier (MID) are the primary detectors that reconstruct and identify muon tracks in the forward region, where there is an additional absorber placed between them. There are ongoing attempts to improve the matching between the stand-alone charged tracks in the MFT and the stand-alone muon tracks in the MCH+MID, where one of the primary methods currently used is machine learning - as done in [31]. The Muon Spectrometer can be used to measure the single-muon production originating from HF and $W^{\pm}$ boson decays in the forward rapidity region [6], which motivates selecting this region for the analysis in this work.

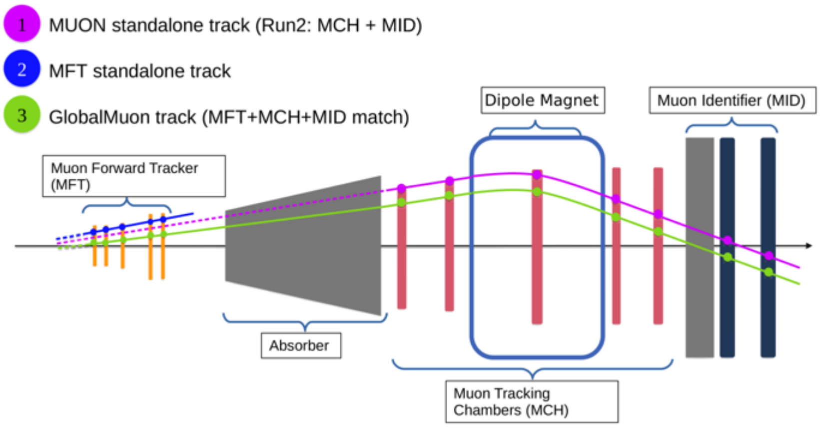

Figure 12: The ALICE Muon Spectrometer, showing the Muon Forward Tracker (MFT), Muon Chambers (MCH) and Muon Identifier (MID) - with example reconstructed muon tracks [31].

2 Theory

In the introduction, a bigger picture overview was given about the physics context and motivations in this work. In this section, the focus will be on a more detailed look at some of the general theoretical aspects of relevance. In section 2.1, the particle physics theory used to describe the interactions of fundamental particle will be briefly introduced - where [3] and [32] will be closely followed. In section 2.2, it will then be built upon to have a closer look at the specific case of modelling relativistic proton-proton collisions. The focus will be on the models implemented in the simulations used in the analysis of this work, so [19] will be closely followed. It has already been mentioned that the processes of interest are quantum mechanical and relativistic in nature. Thus, it is necessary to briefly look at the basic principles of the quantum field theory (QFT) calculations that are used to determine the theoretical cross-sections of the various processes - as the production cross-sections will be one of the key observables in this work.

2.1 Particle Physics

2.1.1 Fundamental Particle Interactions

Before considering the more complicated system of colliding hadrons, which have been mentioned to be composite states of quarks/gluons, it is necessary to look at the simpler case of interactions of the fundamental particles first - which is governed by the three fundamental forces of the Standard Model. The nature of how the fermions are affected by the different forces is determined by the unique properties of the "force-carrying" bosons, which are described by the associated QFTs. This coupling of the fermions to the bosons is given by the interaction vertices, as depicted in Figure 13. For each different boson's interaction vertex, there is an associated coupling strength - denoted here with g. For example, the coupling strength of the electromagnetic interaction is simply given by the charge of the electron as $g_{QED} = e$. It is important to note that only particles that carry the relevant charge of the force will couple to the associated boson. For example, it has already been mentioned that the vector bosons and leptons have no colour charge. Thus, they will not couple and interact with the strong nuclear force boson (gluon). Each interaction vertex will also satisfy conservation requirements, such as the conservation of energy/momentum and charge, which places physical restrictions on the vertices that can exist [3].

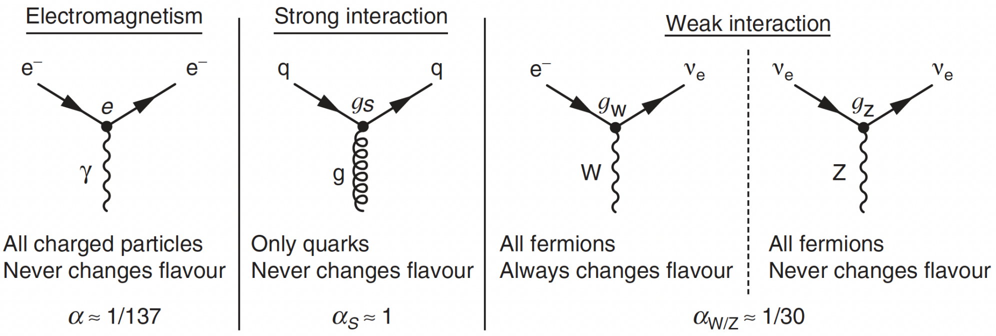

Figure 13: The interaction vertices of the fundamental forces of the Standard Model [3].

Now that the fundamental interaction vertices are described for each Standard Model force, it is possible to join them together to consider the structure and evolution of complete processes. Figure 14 depicts the general scattering process of fermions through the exchange of a boson, by combining two of the fundamental interaction vertices. In order to extract meaningful physics information from these process diagrams, it is necessary to consider all the time orderings in which the processes can occur. This is done through what is known as Feynman diagrams, as depicted for a general 2 → 2 scattering process in Figure 15. On a more fundamental level, Feynman diagrams represent the transition between states (such as a scattering process) in the QFT description, by representing all the possible time orderings of the process of interest [3]. Feynman diagrams are particularly useful, as once it has been constructed for a specific process, it can then be used to write down the quantum mechanical transition matrix amplitude without having to calculate each process with QFT from first principles. It is important to mention that Feynman diagrams do not represent the physical trajectory of the particles, but are merely a pictorial representation for a number which can be calculated from the derived Feynman rules for a particular QFT. A simplified example of how the matrix amplitude is calculated is presented in 6.1.

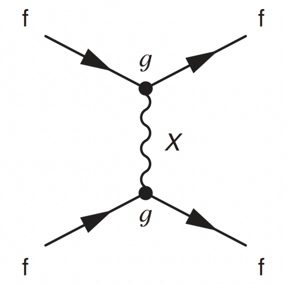

Figure 14: The t-channel scattering process of fermions (f), through the exchange of a boson (X) [3].

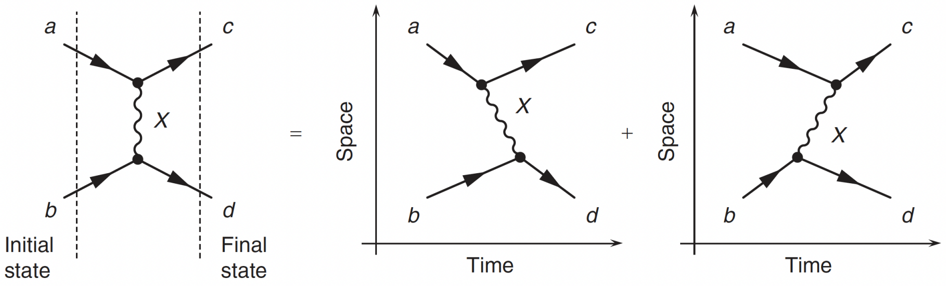

Figure 15: The Feynman diagram for a general 2 → 2 scattering process, showing the two time ordering contributions [3].

2.1.2 Theoretical Cross Section

In section 1.2.3, it was described how the production cross-section of a process is an observable of interest in the context of scattering experiments. In this section, the goal will be to briefly discuss how the cross-sections can be theoretically calculated in the framework of relativistic quantum mechanics. It is often easier to work with a differential cross-section ($d\sigma/d\Omega$) in this case. The interpretation of the differential cross-section is illustrated in Figure 16 in the context of a fixed-target scattering experiment, where the incident beam passes through an infinitesimal target area $d\sigma$ and then scatters into a resulting solid angle $d\Omega$. The differential cross-section is then the proportionality factor D given as $d\sigma = D(\theta)d\Omega$, where D is determined by the physics of the relevant processes involved. In the context of collision experiments as discussed before, equation 1.2.3 can be written in differential form as $dN = \mathcal{L}d\sigma$ - from which equation 2.1.2 can then be obtained [32]. This shows that the differential cross-section can be experimentally measured by considering the rate of particles reaching a detector that is located in a solid angle region $d\Omega$.

$$\frac{d\sigma}{d\Omega} = \frac{1}{\mathcal{L}}\frac{dN}{d\Omega} \tag{3}$$

To considered how the cross-section is calculated theoretically, it is necessary to start by looking at Fermi's Golden Rule. Simply put, the rule says that the transition rate Γ of a process of interest is given

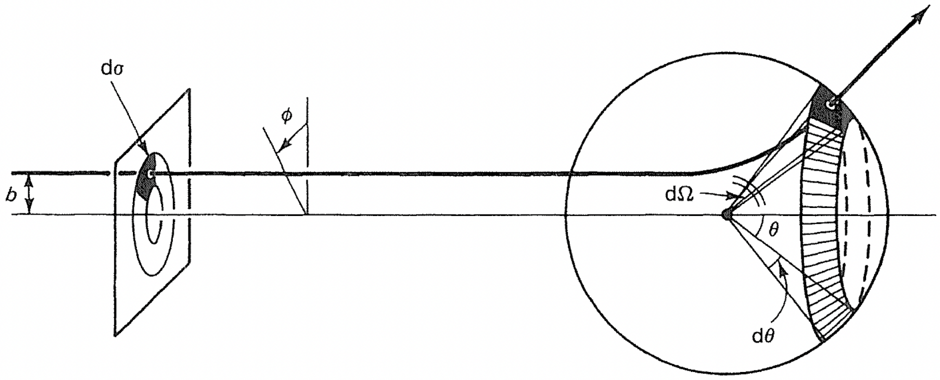

Figure 16: Diagram showing the differential scattering angle $d\Omega$ for an incident particle in area $d\sigma$ [32].

by the product of the phase space and the square of the matrix amplitude (M) [32]. The dynamics of the process is fully given by M, which is calculated from the Feynman diagrams as mentioned before. For the case of a general two-body scattering process ($1+2 \rightarrow 3+4$), it can be shown from Fermi's Golden Rule that the cross-section of this process (in the centre-of-mass frame) can be obtained as [32],

$$\sigma = \frac{S\hbar^2 c}{64\pi^2(E_1+E_2)|\mathbf{p}_1|}\int |M|^2 \frac{\delta^4(p_1+p_2-p_3-p_4)}{\sqrt{\mathbf{p}_3^2+m_3^2c^2}\sqrt{\mathbf{p}_4^2+m_4^2c^2}} d^3\mathbf{p}_3 d^3\mathbf{p}_4, \tag{4}$$

where S is a statistical factor that prevents double counting when having identical particles in the final state. The phase space factor is constructed by integrating over the four-momenta of the outgoing particles and including kinematic constraints - such as ensuring energy and momentum conservation. After carrying out the integrals, it can be shown that the differential cross-section of the two-body scattering process is given as [32],

$$\frac{d\sigma}{d\Omega} = \left(\frac{\hbar c}{8\pi}\right)^2 \frac{S|M|^2}{(E_1+E_2)^2}\frac{|\mathbf{p}_f|}{|\mathbf{p}_i|}, \tag{5}$$

where $|\mathbf{p}_f|$ and $|\mathbf{p}_i|$ refer to the magnitudes of the either of the outgoing or incoming momenta respectively. It is possible to reach the level of simplification of equation 2.1.2 without explicitly evaluating and knowing the functional form of M. In the more general case, if there are n particles involved in the process of interest, the units of M is given by $[M] = (mc)^{4-n}$. It can be shown that this will result in the cross-section having units of barns, as defined in section 1.2.3.

2.1.3 The Weak Interaction

One of the aims of this work is to investigate the charged vector boson ($W^{\pm}$) production in relativistic proton-proton collisions, as already motivated in the previous sections. Thus, it is necessary to briefly look into the basic theoretical aspects of the weak interaction. There exists two kinds of weak interactions, namely the charged version mediated by the $W^{\pm}$ bosons and the neutral version mediated by the Z^0 boson [32]. Experimentally, these two interactions are mostly studied independently and the focus in this work will be purely on the charged interaction. The $W^{\pm}$ boson is a massive spin-1 gauge boson, as opposed to the massless bosons of the electromagnetic (photon) and strong (gluon) interactions. The mass of the $W^{\pm}$ boson (M_W) has been measured by multiple experiments, with the most precise result being recently published by CMS in proton-proton collisions at $\sqrt{s} = 13$ TeV. It was obtained as $M_W = 80360.2 \pm 9.9$ MeV [33], where there is ongoing work to accurately predict the mass from the theory of the Standard Model [34].

It has been experimentally shown that the weak interaction does not conserve parity, as opposed to the electromagnetic and strong interactions that do. The parity operator ($\hat{P}$) is defined to invert space through the origin as $\mathbf{x} \to -\mathbf{x}$, which ends up to be a Hermitian operator with eigenvalues ± 1. In the context of the Dirac formalism, it can be shown that the parity operator is simply γ_0 for Dirac spinors [3] - a clear definition of spinors can be found in 6.2. It can also be shown that spin-half particles and anti-particles have opposite intrinsic parities, where it is chosen by convention for anti-particles to have negative intrinsic parity. Similarly, the force-carrying bosons all have a negative intrinsic parity. Parity conservation for an interaction arises mathematically from how the parity operator acts on the spinor four-vector currents contained in the matrix amplitude. For example, in QED and QCD interactions, the four-vector currents have the form $j^\mu = \bar{u}(p')\gamma^\mu u(p)$ - which mathematically are vectors that lead to parity conservation at a vertex. These requirements lead to the vector minus axial-vector (V-A) form of the weak interaction, where the four-vector current is given as $j^\mu = \bar{u}(p')\frac{1}{2}\gamma^\mu(1-\gamma^5)u(p)$. The vertex factor of the weak charged current, through the exchange of a $W^\pm$ boson, is then given as

$$\frac{-ig_W}{\sqrt{2}}\frac{1}{2}\gamma^\mu(1-\gamma^5), \tag{6}$$

where g_W is the weak interaction coupling constant - as introduced in section 2.1. Furthermore, every spinor can be decomposed into left- and right-handed chiral components when using the chiral projection operators defined as $P_R = \frac{1}{2}(1+\gamma^5)$ and $P_L \frac{1}{2}(1-\gamma^5)$. Chirality is an intrinsic quantum mechanical property of fundamental particles, which will not be discussed in detail in this work. It is only important to mention that the V-A form of the weak interaction directly leads to it coupling only to left-handed chiral particle and right-handed chiral anti-particle states.

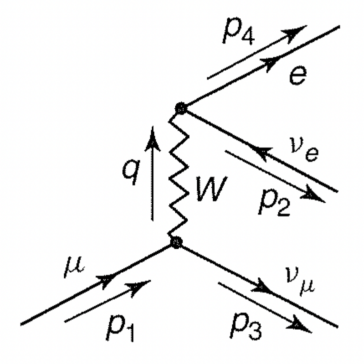

Figure 17: Feynman diagram for the weak interaction process of muon decay $\mu \to e + \nu_\mu + \bar{\nu}_e$ [32].

Now it is possible to briefly look at the cleanest weak interaction process, both theoretically and experimentally, which is muon decay ($\mu \to e + \nu_\mu + \bar{\nu}_e$) - shown in Figure 17. In the case where $q^2 << M_W^2 c^2$, the matrix amplitude for the muon decay process can then be given as [32],

$$M = \frac{g_W^2}{8(M_W c)^2}[\bar{u}(p_3)\gamma^\mu(1-\gamma^5)u(p_1)][\bar{u}(p_4)\gamma_\mu(1-\gamma^5)u(p_2)]. \tag{7}$$

Following the procedure laid out in section 2.1.2, the matrix amplitude can then be used to obtain the theoretical differential cross-section of the decay process. It will then be shown in section 2.2.1 how the differential cross-section can be used to then obtain the cross-section of the same process, but in the context of relativistic proton-proton collisions. This serves as an introductory basis of the theoretical framework used to obtain the simulated cross-sections that will be presented in the results of this work.

2.1.4 Quantum Chromo-Dynamics

In the context of Quantum Electrodynamics (QED), the requirement that the physics should be invariant under local U(1) phase transformations leads to the existence of a gauge field that couples to the Dirac particles - which resembles the photon. In the same way, Quantum Chromodynamics can be obtained from requiring that the physics is invariant under SU(3) local phase transformations as [3],

$$\psi(x) \to \psi'(x) = exp[ig_S \boldsymbol{\alpha}(x) \cdot \hat{\mathbf{T}}]\psi(x),$$

where g_S is the known strong coupling constant, $\hat{\mathbf{T}} = \{T^a\} = \{\frac{1}{2}\lambda^a\}$ are the generators of the SU(3) group related to the Gell-Mann matrices (λ^a) as shown, and $\alpha^a(x)$ are functions of the space-time coordinates. Since the SU(3) generators are represented by 3×3 matrices, this requires the wavefunction to include three additional degrees of freedom given by a three-component vector - this is known as "colour", where the three states are labelled with red (r), green (g) and blue (b). The SU(3) local phase transformations are then given by "rotating" the states within this colour space. The required gauge invariance under these transformations can then be enforced through introducing eight new fields $G^a_\mu(x)$, where each corresponds to one of the mentioned generators of the SU(3) group - these fields then represent the gluons of QCD. Since the generators of SU(3) do not commute, this results in QCD being a non-Abelian theory that gives rise to gluon self-interactions.

It has been mathematically motivated that the strong force is mediated by eight massless gluons, which correspond to the generators of the SU(3) group in QCD. This gives rise to the conserved colour charges (r, g and b), where only particles with a non-zero colour charge will interact strongly - this includes only quarks and gluons. Similar to QED, antiparticles will carry the opposite colour charge ($\bar{r}, \bar{g}$ and $\bar{b}$) to their associated particle. In order to account for the additional degrees of freedom given by the colour charge, it is no longer sufficient to represent the quark wavefunction as a Dirac spinor. This can be resolved by adapting the spinor representation for the quark wavefunction as,

$$u(p) \to c_i u(p),$$

where c_i represents one of the possible three-component vector colour states. From this, the quark current at a QCD vertex (portrayed in Figure 18) can then be shown to be

$$j^\mu = \bar{u}(p_3)c_j^\dagger\{-\frac{1}{2}ig_S\lambda^a\gamma^\mu\}c_i u(p_1),$$

where c_i and c_j are the associated colour wavefunctions of the quarks, and the label a refers to the gluon corresponding to the generator T^a. In this quark current form, the 3×3 λ matrices will act on the three-component colour states and the 4×4 γ matrices will act on the four-component spinor.

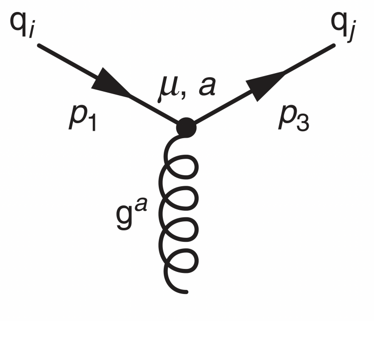

Figure 18: The quark-gluon vertex in QCD, depicting the interaction of colour charged quarks with a gluon of type a [3].

Now that the mathematical basis of QCD has been briefly defined, it is possible to look at some of the physical consequences/requirements of the theory. It has already been mentioned that no free quarks have been experimentally observed, only colourless bound states known as hadrons - which is known as colour confinement. The interaction between the quarks in the bound state occurs via the exchange of virtual gluons. It is then hypothesized that the confinement can arise due to the gluon-gluon self-interactions, where the attractive interaction between the exchanged virtual gluons results in squeezing the colour field between the quarks into a confined "tube" topology. When considering a large distance between the quarks, the energy density stored in the tube can be taken to be constant. This means that the energy stored in the tube will be proportional to the distance between the quarks, resulting in the potential having the form

$$V(\bar{r}) \propto \kappa r,$$

where κ is known experimentally to be on the order of 1 GeV/fm. Since the energy stored in the tube increases linearly with distance, it would require an infinite amount of energy to separate the two quarks to infinity. This results in the phenomena of colour confinement, where the quarks will arrange themselves into colourless hadronic bound states. How this is modelled in theoretical simulations will be discussed briefly in sections 2.2.5 and 2.2.6.

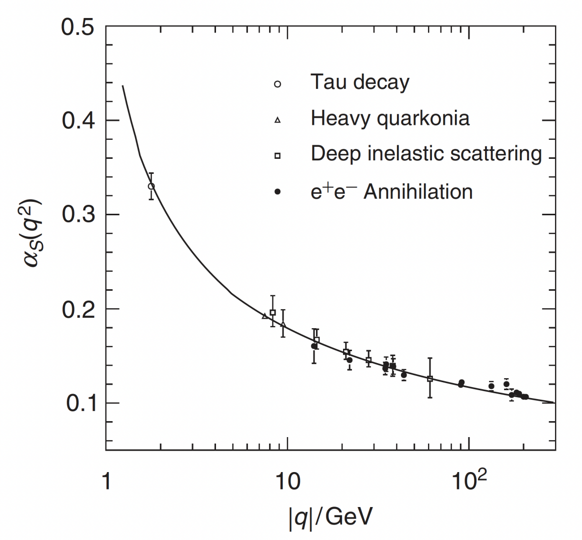

Figure 19: Experimental measurements of α_S at different interaction energy scales [3].

As shown in Figure 19, it is experimentally known that the coupling constant of QCD (α_S) is in fact not a constant, but rather changes as a function of the interaction energy scale. This is known as the 'running coupling' of QCD, which is closely related to the mathematical method of renormalisation - will not be discussed in this work. The evolution of α_S as a function of the interaction energy scale (q^2) can then be given as [32],

$$\alpha_S(q^2) = \frac{12\pi}{(11N_C - 2N_f)\ln(|q^2|/\Lambda^2_{QCD})} \quad \text{for} \quad (|q^2| >> \Lambda^2_{QCD}),$$

where it is defined such that $\ln(\Lambda^2_{QCD}) = \ln \mu^2 - 12\pi/[(11N_C - 2N_f)\alpha_S(\mu^2)]$, where μ is a reference energy scale chosen such that $\alpha_S(\mu^2) < 1$; while also having $N_C = 3$ for the number of colour charges and $N_f \leq 6$ for the number of quarks. From this it is clear that α_S drops off as a function of the interaction energy. The result of this is that QCD can be divided into two regimes, namely the non-perturbative low-energy regime (soft-QCD) and the perturbative high-energy regime (hard-QCD) - which is an important concept within this work.

2.2 Modelling Proton-Proton Collisions

In the previous section, the fundamental particle physics basis of the Standard Model was introduced. It was briefly shown how the differential cross-section of physics processes of interest can be computed mathematically from the Feynman diagrams. In this section, the focus will be on describing how these fundamentals are applied to model proton-proton collisions at relativistic energies, and how to statistically generate events from these models for analysis purposes. Since this work will make use of POWHEG and Pythia to generate these events, the models used by these MC event generators will be focused on specifically. Figure 20 serves as an encompassing pictorial representation of a simulated proton-proton collision event in Pythia, where the different theoretical components/models used in the simulation are depicted - with the "hardness" of the energy scale being largest in the centre and then decreasing outwards. The components relevant to the analysis in this work will be discussed in more detail in the following sections.

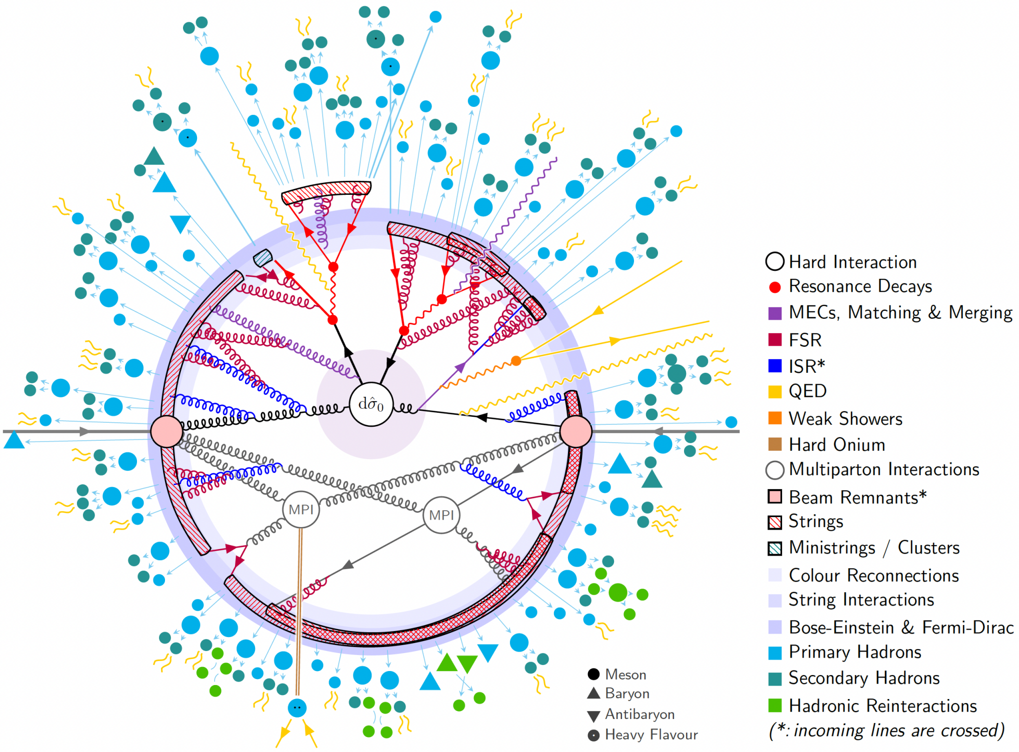

Figure 20: Representative schematic of a proton-proton collision event as modelled in Pythia, showing the contributing model components [19].

2.2.1 Proton-Proton Cross Section

In the case of proton-proton collisions at relativistic energies, the model needs to go beyond just the elastic scattering of protons. In this work, the focus will be specifically on in-elastic collisions that produce new particles. The protons can be seen as being made up of a "sea" of fundamental particles (quarks and gluons), which will be referred to as partons - how the energy/momentum of the proton is distributed between the partons will be the focus in section 2.2.2. In the previous section, it was briefly shown how the cross-section of the scattering of fundamental particles can be computed within the framework of relativistic quantum mechanics. The translation of the cross-section from the fundamental particle scattering to the more complicated case of hadronic bound states colliding is given by the Factorisation Theorem. Considering the case where two hadron beams (A and B) collide, where the partons from the two beams (a and b respectively) interact in the partonic scattering, the Factorisation Theorem is then given as [19]:

$$\frac{d\sigma_{pp}}{d\Omega} = \int dx_1 f_a^A(x_1, Q^2) \int dx_2 f_b^B(x_2, Q^2) \frac{d\hat{\sigma}_{ab}(\hat{s}, Q^2)}{d\Omega}, \tag{8}$$

where $f_a^A(x_1, Q^2)$ and $f_b^B(x_2, Q^2)$ are the relevant PDFs for the incoming beams, which will be elaborated on in the next section. The $d\hat{\sigma}_{ab}/d\Omega$ term is the usual theoretical differential cross-section as defined in section 2.1.2, where $\hat{s} = x_1 x_2 s$ and $s = (p_A + p_B)^2$, and Q^2 is the energy scale of the process [19]. The definition of x_1 and x_2 will be given in detail in the next section. It is important to mention that most of the processes of interest in this work will be perturbative and M can be determined with the Feynman rules as laid out in section 2.1. There are cases, such as QCD processes with low momentum transfers, where the perturbative regime diverges and an alternative approach is required - as discussed in section 2.1.4. To show this more explicitly, consider the factorisation scale given as $Q^2 = {p_\perp}^2$ with the assumption that the partons are massless, and considering only processes with the same initial but different final states to contribute. This will lead to the differential cross-section, as given in equation 8, to be dominated by t-channel gluon exchange [19]. For this cross-section under consideration, there exists an approximation that is given as

$$\frac{d\sigma}{d{p_\perp}^2} \propto \frac{\alpha_s^2({p_\perp}^2)}{{p_\perp}^4}, \tag{9}$$

where α_s is the strong coupling constant as defined in section 2.1.4. It is clear that this will diverge in the limit as $p_\perp \to 0$, as shown by the standard case (no damping introduced) in Figure 21. Thus, it is necessary to introduce a damping factor to tame the divergence as $p_\perp \to 0$, which will be defined as

$$\left(\frac{\alpha_s^2({p_{\perp,0}}^2 + {p_\perp}^2)}{\alpha_s^2({p_\perp}^2)} \frac{{p_\perp}^2}{{p_{\perp,0}}^2 + {p_\perp}^2} \right)^2, \tag{10}$$

where $p_{\perp,0}$ is a new free parameter that can not be derived from first principles. From fits to experimental data, a value for $p_{\perp,0}$ can be obtained - which varies with the centre-of-mass energy of the proton-proton collisions being considered. It is important to note that this value is also sensitive to the PDF set being used, especially the small Bjorken-x region of the gluon distribution at small Q^2 [19]. The result from including the damping factor to the cross-section can be seen as the damped curve in Figure 21.

Now it is possible to define the hardest partonic interaction of the proton-proton collision event, as denoted by $d\hat{\sigma}_0$ in Figure 20. Simply put, the hardest interaction is the partonic scattering, as calculated by equation 8, with the largest momentum transfer in the collision event. In the simulation process, the hardest interaction is very important, as it defines the relevant energy scales of the event. The other processes are evolved forwards and backwards in time from the hardest interaction, with the available phase-space being defined by the nature of the hardest interaction [19]. It is important to note that this is not the only hard partonic interaction that can take place in the event, subsequent partonic scatterings will be described by the modelling of multiparton interactions (MPIs) - which will be elaborated on in section 2.2.4.

2.2.2 Parton Distribution Functions

In the previous section, the Parton Distribution Function $f(x, Q^2)$ (PDF) was introduced as a factor in the Factorisation Theorem - which is used to obtain the cross-section of a process in a hadronic collision from the more fundamental partonic interactions. When probing the hadronic nucleus at an energy scale of Q^2, the PDF set gives the probability distributions of finding different partons with a fraction x (known as Bjorken-x) of the four-momentum of the hadron [19]. In Figure 22, it shows the distributions for various partons from the NNPDF3.0 (NNLO) set at two different energy scales [35]. It is clear that at higher energy scales the probability of finding valence quarks with a large momentum fraction decreases, where the opposite is true for gluons. It can also be seen that the uncertainty bands on the distributions tend to get larger at small values of x.

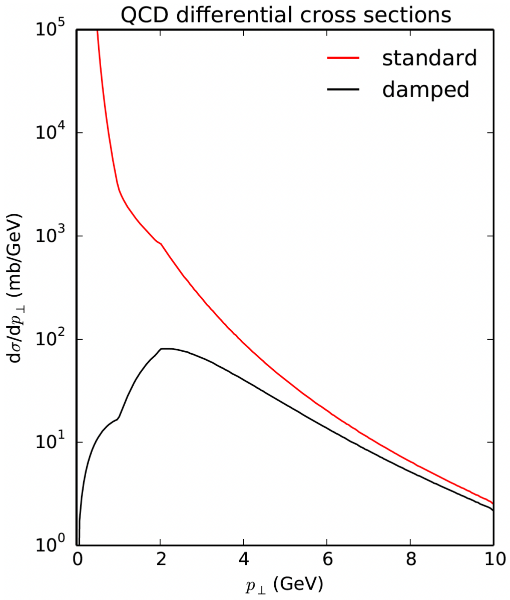

Figure 21: The differential $2 \to 2$ QCD cross-section for proton-proton collisions at $\sqrt{s} = 13$ TeV from standard perturbation theory, showing the effect of including the damping factor given in equation 10 [19].

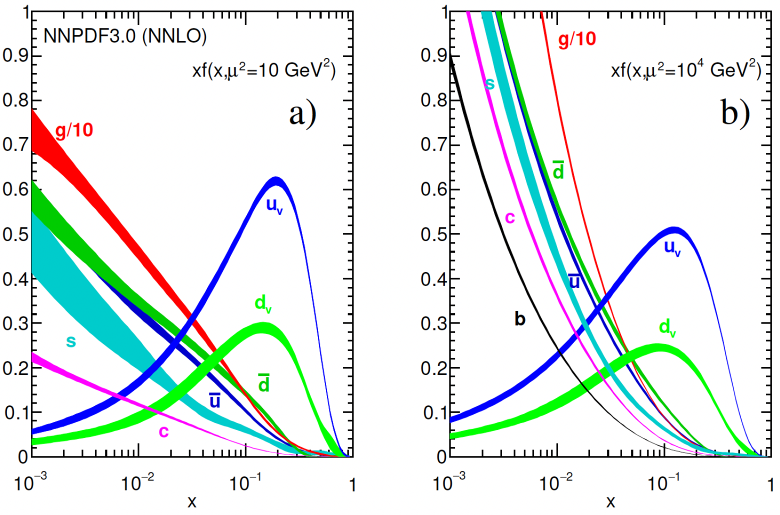

Figure 22: The NNPDF3.0 (NNLO) parton distribution functions at the energy scales of $Q^2 = 10$ GeV^2 (left) and $Q^2 = 10^4$ GeV^2 (right) [26].

To be more explicit, the momentum of the interacting parton p_{parton} can be given in terms of the energy of the colliding hadron E_{hadron} (in the centre-of mass frame where $E = \sqrt{s_{hadron}}/2$) and Bjorken-x as [3],

$$p_{parton} = xE_{hadron}(1, 0, 0, \pm 1), \tag{11}$$

where the hadron is considered to be moving in either the $\pm z$ direction. For two hadrons colliding head-on, it can then be shown that the centre-of-mass energy of the partonic interaction (s_{parton}), with incoming four-momenta p_1 and p_2, is given as

$$s_{parton} = (p_1 + p_2)^2 = E_{hadron}(x_1 + x_2, 0, 0, x_1 - x_2)^2 = 4x_1x_2E^2_{hadron}. \tag{12}$$

From this, it can then be concluded that $s_{parton}/s_{hadron} = x_1x_2$, which shows that the fraction of the energy of the hadronic collision carried by the partonic interaction is simply given by the product of the Bjorken-x momentum fractions of the partons and the hadron energy squared. Now when considering the kinematic variable rapidity (y), which is defined in terms of the collision kinematics (the energy E and momentum component p_z) as [20],

$$y = \frac{1}{2}\ln\left(\frac{E + p_z}{E - p_z}\right). \tag{13}$$

In the centre-of-mass frame of the partonic scattering this then becomes

$$y = \frac{1}{2}\ln\left(\frac{E(x_1 + x_2) + E(x_1 - x_2)}{E(x_1 + x_2) - E(x_1 - x_2)}\right) = \frac{1}{2}\ln\left(\frac{x_1}{x_2}\right). \tag{14}$$

After some algebra and using equation 12, it can be shown that the Bjorken-x of the partons are related to the rapidity as

$$x_{1,2} = \frac{\sqrt{s_{parton}}}{2E}e^{\pm y}. \tag{15}$$

From equation 15, it is clear that the case of $y = 0$ (perpendicular to the z-axis) would correspond to $x_1 = x_2$, which is expected from the conservation of momentum in the z-direction. It can also be seen that large values of y (the forward rapidity region) will lead to x_2 being small. This serves as a clear motivation for why it is meaningful to study the production of particles, created in the hard partonic scattering (such as the vector bosons), in the forward rapidity region. These particles can serve as a good probe of the relevant PDFs that contribute to the production, at the small Bjorken-x scale.

In order to determine the PDFs at different energy scales Q^2, the non-perturbative aspects firstly need to be fitted to a large set of experimental data at an initial energy scale [19]. Figure 23 shows the contributions from different experiments to the dataset used for the fitting of the NNPDF2.3 set - also showing how they contribute to different kinematic regions. After fitting at an initial energy scale, the Dokshitzer–Gribov–Lipatov–Altarelli–Parisi (DGLAP) equations can be used to evolve the PDFs to the different energy scales as required [19]. The technicalities of how the fitting and evolution is done will be outside the scope of this work. It is merely important to note that experimental data, especially at small Bjorken-x scales where the uncertainties are the largest, is currently strictly required as input for the determination of PDFs - where the electroweak boson measurements play a critical role.

2.2.3 Radiation and Beam Remnants

In addition to the partonic scattering process, there can also occur radiation processes during the initial and final stages of the collision - as depicted by initial-state radiation (ISR) and final-state radiation (FSR) in Figure 20. For example, a gluon can be emitted from a parton during ISR before interacting in the hard scattering process. This gluon can then in turn split into a quark-anitquark pair, which will be important in the context of heavy-flavour pair production in this work. The radiation will also contribute to the charged-particle multiplicity, as additional hadron showers can result from the radiated gluons. The radiation also contributes to free colour charges that need to be accounted for when resolving the colour aspects of the resulting event topology - which will be discussed in more detail in section 2.2.6. All the possible radiation

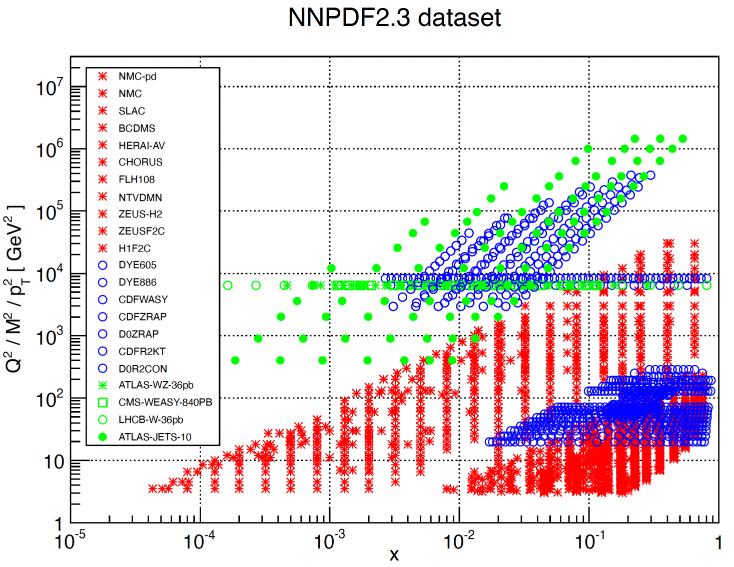

Figure 23: The kinematic coverage of the experimental data contributions used for the NNPDF2.3 PDF set determination [35].

processes will not be discussed at length, as it does not contribute to the production of $W^{\pm}$ bosons - which is the primary process of interest in this work.

After the relevant partons have been "removed" from the hadrons to undergo hard partonic scattering, including multi-parton interactions described in the next section, the collection of partons that remain are known as the beam remnants [19]. The remnants will not undergo any further interactions with large momentum transfers, so they they only contribute to the non-perturbative soft scale. In Pythia, the approach for dealing with beam remnants is to add the minimum number of remnant partons that are required to maintain the conservation of the quantum numbers of the original beam hadrons. The remaining momentum, which is not carried by the hard scattering partons, is then distributed among the remnant partons. The details of how this is implemented will not be of relevance in this work, but it is important to mention that the remnant partons will also carry colour charges that need to be taken into account when considering the colour aspects of the resulting event topology.

2.2.4 Multi-Parton Interactions

The hardest interaction was defined in section 2.2.1 as the hard partonic scattering with the largest momentum transfer, which sets up the energy scale for the rest of the underlying event. As the proton is made up of multiple partons that carry fractions of the total momentum (given by the PDFs), it is safe to assume that there can be more than only a single hard partonic interaction that takes place. Since there is limited energy/momentum available in the collision, which needs to be distributed among the hard partonic interactions and rest of the underlying event (such as ISR and FSR), it becomes a challenge to correctly order all these processes in time, and to assign them parts of the phase-space. In this section, the basics of the approach used by Pythia to overcome this challenge when implementing multi-parton interactions (MPI) will be discussed.

In Pythia, the generation process for MPIs is formulated as an evolution downward in $p_\perp$ from the hardest interaction [19]. Considering n partonic interactions to take place in the event, the ordering will then look like $\sqrt{s_{parton}}/2 > p_{\perp,1} > p_{\perp,2} > ... > p_{\perp,n} > 0$. With this, an iterative process can then be used for the evolution of the partonic interactions - where a probability is calculated for each subsequent partonic interaction to occur while evolving downward in $p_\perp$. It is also important to assign momentum fractions to the multiple interacting partons when moving along the evolution. Purely from momentum conservation, the first restriction requires that the assigned momentum fractions for a single proton's partons can not add up to more than unity. The standard PDFs can be used to assign x for the hardest interaction, but a repeated use of the same PDFs for subsequent interactions can result in violating the momentum conservation - or even allowing the repeated colliding of the limited valence quarks that have already been assigned [19]. Thus, it is necessary to gradually modify the PDFs for the subsequent partonic interactions - the technical aspects of the modification will not be discussed in this work.

It is important to mention for the evolution discussed above, that it is also necessary to account for the flavour aspects of the available constituents of the colliding protons. To achieve this, the PDF framework as discussed in section 2.2.2 is extended to include flavour counting. This is achieved by assuming that the quark distributions can be split up into a valence and sea part, as shown in equation 16 - which can then be used to determine the probability whether a kicked-out quark is valence or sea. It is also assumed that the sea part is flavour-antiflavour symmetric.

$$f(x, Q^2) = f_{valence}(x, Q^2) + f_{sea}(x, Q^2) \tag{16}$$

In the full framework of MPIs, it is not as simple as purely considering isolated $2 \rightarrow 2$ hard scatterings evolving downward in $p_\perp$ - as done so far. It is also necessary to account for the ISR and FSR showers - where each partonic interaction can also come with it's own additional ISR and FSR. Since the ISR also needs to be assigned momentum/energy from the beam and can change the flavour content, it needs to be accounted for in the MPI procedure. If the partonic scatterings are generated first, then they will be maximized and not leave enough energy/momentum for the showers, and vice-versa if the showers are generated first. Since there is no clear method given by the time-ordering of the processes, it is specifically chosen to first generate the hardest interaction correctly, and then use $p_\perp$ as a common evolution scale for the rest of the subsequent processes - which are generated backwards and forwards in time [19]. An interleaved approach is also used to determine the probability of what the next process will be in the downward evolution - the more technical aspects of the interleaved approach will not be discussed in this work.

Another influencing aspect of the MPI framework that has not been touched on, is the issue of colour flow. Each parton that participates in the hard interaction will carry a colour charge, and leave behind a corresponding anti-colour in the beam remnant. In the case where many MPIs are being generated, this results in unrealistically complicated beam remnants that need to be dealt with. In Pythia, the situation is simplified by firstly associating colour and anti-colour charge pairs between the participating MPI partons, and then associating remaining colour charges with the beam remnant partons [19]. The mechanism used to reconnect these colour charges in a meaningful way is known as Colour Reconnection (CR), which will be discussed in more detail in section 2.2.6.

From the presented description of the MPIs framework, it becomes more clear how the final-state charged-particle multiplicity is affected by the MPI model - as was shown in Figure 3. By introducing the possibility for multiple partonic scatterings to take place, the available energy in the collision will be distributed among the increased number of particles that are produced by the multiple scatterings - as opposed to only the limited products of a singular partonic interaction. This results in the multiplicity distribution being skewed towards higher multiplicity values when introducing the MPI model. In the context of the $W^\pm$ boson production, it has already been mentioned that they will be produced only in the hard partonic scattering. Since the $W^\pm$ boson has such a large mass, it will take a large chunk of the available energy to be produced - limiting what is available for the additional partonic scatterings. Thus, it is expected for the $W^\pm$ boson cross-section to drop off at higher multiplicities - investigating this will be the focus of section 4.3.3.

2.2.5 Hadronisation

In the previous sections, a brief overview was given about the perturbative partonic interactions of relativistic proton-proton collisions. It has been shown that a result of these processes are free quarks that carry a colour charge. The next sections will be aimed at looking at the "softer" non-perturbative processes involved, that are responsible for the transition of free colour charges from the partonic interactions to a multi-particle final state. It will briefly be shown how Pythia implements hadronisation, which handles this process of transitioning free colour charges into colourless hadronic bound states - as well as the formation of multi-particle hadronic jets. As this transition is in the non-perturbative regime, an additional model needs to be formulated to theoretically describe the process - in Pythia it is known as the Lund string model [19].

In the Lund string model, the confining force field between a colour and anti-colour charge pair is viewed as a flux tube, where the potential energy increases linearly between the two colour charges, as shown in section 2.1.4 - which is then referred to as a string. As the colour-charged partons at the ends of the string move apart, the energy is transferred from the partons to the string itself - with a linear energy density of $\kappa \approx 1$ GeV/fm. In the simple case of a quark and anti-quark ($q\bar{q}$) pair, this description gives rise to what is referred to "yoyo" modes for $q\bar{q}$ dipoles in 1+1 dimensions - where the string oscillates by continuously transferring the available energy between the quarks and the string - this is identified as mesons in the string picture. In the case of longer strings, new $q\bar{q}$ pairs will break up the string to form multiple hadrons - which accounts for the observation of multi-particle hadronic jets. The model assigns a probabilistic description for the string to break up into a state of n hadrons, which depends on a new parameter noted as b.

When viewing the string breaking mechanism as an iterative process, and imposing the constraint that the same result should be obtained on average when fragmenting from either the left or right end of the string for consistency, the distribution of the momentum fraction (z) taken by each hadron is obtained as [19],

$$f(z) \propto \frac{(1-z)^a}{z} \exp\left(-\frac{bm^2}{z}\right), \tag{17}$$

where m is the mass of the associated hadron and a is a new parameter related to b. This distribution is referred to as the Lund symmetric fragmentation function, and plays a crucial role in the model. In Pythia, the fragmentation function in equation 17 is used by default with set values for the a/b parameters. Depending on the application and requirements, the fragmentation function can still be modified further - discussing this will not be within the scope of this work.

2.2.6 Colour Reconnections

In the previous section, the Lund string model was introduced as a model to describe the hadronisation process as a linear confining potential that arises between a colour and anti-colour charge pair - known as a string. In section 2.2.4, it was also shown how multiple "free" colour charges are produced in the MPIs of the event - which makes the colour dynamics of the resulting event topology complicated to deal with. Thus, it is necessary to introduce an additional model to deal with the complex system of many free colour charges that need to be connected to form strings - which will hadronise to produce hadronic showers. In this section, the Colour Reconnection (CR) approach used in Pythia will be briefly introduced.

In order to simplify the arising colour dynamics of the event, all perturbative processes (including MPIs, ISR and FSR) are dealt with in the Leading Colour (LC) limit - where the probability for two randomly selected colour charges to be the same tends to zero. To be more explicit, this is formally done by considering the limit as $N_c \to \infty$, while keeping $\alpha_s N_c$ fixed to ensure that the amplitudes calculated with QCD retain their $N_c = 3$ normalisations [19]. The LC limit then results in eliminating effects that are suppressed by factors of $1/N_c^2 \to 0$, as well as allowing for a simplified representation of gluons in colour space. Taking the LC limit also allows for the representation of Feynman-diagram amplitudes in colour space as the product of independent "colour lines" between colour-charged partons - where each colour line will conserve distinct colour charges. This is important in the context of the Lund string model, as it can be shown that each colour line that emerges from a perturbative process in the event can be uniquely mapped to a hadronising string. The term 'Colour Reconnections' then formally refers to any aspect that will result in changing this map between colour-charged partons, which defines the initial configuration of the hadronising strings in the event.

In Pythia, the first large-scale application of CR was within the MPI framework - as introduced in section 2.2.4. One of the requirements of CR was to explain the increasing mean transverse momentum $\langle p_T \rangle$, with an increase in the charged-particle multiplicity (N_{ch}) - as observed in experiments. It was seen that if all the MPI interactions were allowed to form strings in the same manner, the $\langle p_T \rangle (N_{ch})$ distribution would become essentially flat. This resulted in CR specifically being implemented in such a way as to attempt to reduce the total string length, by a complete merge of the partons of separate MPI systems. The probability for two MPIs to be reconnected (P_{reco}) is specifically given as,

$$P_{rec}(p_\perp) = \frac{(R_{rec} p_{\perp,0})^2}{(R_{rec} p_{\perp,0})^2 + {p_\perp}^2}, \tag{18}$$

where $p_\perp$ is the lower scale of the two interactions and $p_{\perp,0}$ is the damping parameter introduced in equation 10. A new phenomenological parameter R_{reco} is also introduced. The reconnections are then done in an iterative process, staring from the MPI with the smallest $p_\perp$ and then moving upward in the scale - where the probability to reconnect is determined for each MPI in the chain. This method results in an implicit dependence on the $p_\perp$ scale. The effects of introducing the CR implementation to reduce the total string length can be seen in Figure 9, where it is clear that that the CR model will lead to a drop-off of the self-normalised charged-particle multiplicity as a function of the self-normalised number of MPI.

The described MPI-based model of colour reconnections is still currently the default used in Pythia today. There are also alternative models available, such as a newer scheme which also relies on the full QCD colour configuration of the beam remnants. This scheme allows for the QCD colour rules to also be incorporated into the reconnection procedure, where it will affect the probability that a reconnection will occur. In addition to the newer scheme, there is also the gluon-move CR model that is implemented in Pythia. Simply put, this model allows for the locations of gluons to be moved around in such a manner as to aid in reducing the total string length. There are many other CR models that have been developed, but they will be outside the scope of this work.

2.2.7 Decays

Now that it has been introduced how particles interact and get produced in relativistic proton-proton collision, it is relevant to consider how produced particles that are unstable and "short-lived" will decay. As already mentioned, in this work the interest will be on heavy-flavour mesons and charged vector bosons that decay leptonically to muons. In Pythia, the resulting unstable particles can be divided into different classifications - where three of these classifications are primarily of interest [19]. The first possibility is to classify unstable particles by their lifetime, which is specifically useful for particles with colour charge - whether this is above or below the hadronisation time. A second possibility is if the particle's partial or total width can be calculated with perturbation theory. The third and most important classification is if the unstable particle is only produced in the hard scattering and not anywhere else - which is the case in this work for the $W^\pm$ boson. These classifications become important when considering how the decays are treated.

By default in Pythia, all states with a mass above 20 GeV are treated as resonances - which is always the case for the $W^\pm$ boson. All other states that do not carry a colour charge, such as leptons and hadrons, are just treated as particles; while the quark and gluon states are treated as partons. It is important to mention that the resonance states are sequentially decayed during the hard process, where the calculated cross-sections of the resonance states will depend on the possible decay channels. Thus, when considering the calculated cross-sections for resonances produced in the hard scattering, the relevant branching ratios are already incorporated into the cross-section. This is also the case in POWHEG, where the muonic decay is already included in the calculation of the hard scattering matrix element. There are exceptions that can arise in the described scheme, such as J/ψ hadrons that can be produced either in the hard scattering or as decays from other particles - these will not be considered in this work.

When it comes to then implementing the decays of unstable particles, there are many complications and technicalities that can arise. In this work, these technicalities will not be covered and the decay strategies will only be mentioned briefly. In most cases, the masses, widths and decay channels with their respective branching ratios can be simply set from the experimentally measured values - without doing any complicated calculations. The unstable particles of interest can then be decayed by randomly selecting one of the decay channels with a probability proportional to its branching ratio, where the use of random numbers will be discussed in the next section. After the decay channel is selected, the available energy and momentum can be distributed among the decay products according to the phase space. Handling the generation of phase space for decays with more than three products is not trivial and more sophisticated algorithms may be required. More details about the configuration of decays in Pythia will be discussed in section 3.1.4.

2.2.8 Monte Carlo Event Generation

Due to the probabilistic nature of the quantum mechanical processes that occur in relativistic proton-proton collisions, the produced particles and their properties will vary from collision to collision. Thus, it is necessary to capture the probability distributions of these variations - if aiming to simulate physical collisions. The probability distributions can either be inferred from studying data, such as PDFs, or can be theoretically calculated or modelled - such as the number of multi-parton interactions. From these distributions, it is then possible to simulate ensembles of varying collision events - which can be compared to data. To achieve this, a numerical algorithm needs to be developed that can generate many random sequences of collision events from the probability distributions, which is known as an 'event generator' [19] - where it has already been mentioned that the Pythia event generator will be used in this work. Event generators provide many useful applications, such as allowing the testing of different theoretical models and studying detector effects on measured data in the experimental context - both will be looked at in this work.

It is important to note that the results obtained from event generators serve only as approximations and not exact solutions, there are many sources of systematic and statistical uncertainties - which will be discussed in more detail in section 4.1. Even though there are parts of the simulation that can be expressed analytically, such as the perturbative matrix element calculation of the hard partonic scattering, there are many other parts that need to be calculated using numerical methods. For this, different Markov Chain Monte Carlo (MCMC) algorithms are used as the main ingredient - where these algorithms rely on the generation of random numbers. On a deterministic computer it is not possible to obtain truly random numbers, so only pseudo-random numbers are generated using deterministic algorithms. This has the benefit of allowing the user to manually set the random seed to either reproduce events with the same seed or generate new ones with a different seed.

In Pythia, there are two main cases in which random numbers can be used. Namely, one where there is memory of previous evolutions in time, and one where there is not. The latter case is the simplest, where the random numbers can be sampled as usual from a known probability distribution. The former case is less simple and requires what is known as a veto algorithm to generate ordered sequences of state changes/transitions, such as the modelling of MPIs in proton-proton collisions. For most of Pythia's evolution algorithms, where the physics is formulated in momentum-space, the ordering in the evolution is done in terms of transverse momentum, from high to low - as already illustrated for the iterative evolution of MPIs in section 2.2.4. The mentioned algorithms are then used in combinations/steps to simulate the physics processes that have been discussed in the previous sections. This forms the full Monte Carlo event generator, which will be configured and used extensively in this work to simulate relativistic proton-proton collisions - further details about the algorithms and generation structure/flow is outside the scope of this work.

3 Software Tools

For the analysis presented in this work, multiple software tools are utilized to perform different tasks - depending on the analysis of interest. In this section, the configuration and usage of these software tools will be discussed. Since the primary objective is the simulation of high-energy proton-proton collisions, the main focus will be to discuss the Pythia Monte Carlo event generator.

3.1 Pythia

Pythia is a scientific coding library written primarily in C++, which is widely used for the generation of high-energy particle collisions where the inclusion of strong nuclear force effects is of importance. It implements a comprehensive set of models (such as MPIs and Lund string fragmentation) to simulate the evolution from a few-body hard-scattering process to a more complicated final state [19]. In this work, Pythia version 8.3 will be used to simulate and generate events of proton-proton collisions at centre-of-mass energies of 5.02 TeV and 5.36 TeV. In the case of the vector boson analysis, Pythia will only be used for the underlying event and partonic showering, as the hard-partonic scattering will be calculated using POWHEG. Even though the models and simulation pipeline is fully implemented in Pythia, there is still a lot of freedom for the user to configure and implement Pythia as desired for the analysis. Thus, in this section the focus will be to discuss the configuration and implementation specifics used in this analysis.

In order to run a Pythia simulation, it is required to firstly configure Pythia for the specific user requirements. The two first important configurable parameters are the collision system and centre-of-mass energy. Setting the collision system, in this work it will always be proton-proton collisions, initializes a whole set of relevant model parameters (such as the PDF) that can also be further configured for each collision system type - this is known as tuning and will be discussed more in the next section.

3.1.1 Tunes

For each collision system of interest, there are many free parameters that need to be set and adjusted according to the context that the simulation is being applied to. These are specifically parameters that can not be derived from first principles with our current physics models and understanding, such as hadronisation and MPI model parameters. Even though these free parameters can be adjusted independently, the requirement of the simulation to describe a set of experimental data leads to correlations and anti-correlations between the free parameters [19]. Thus, the requirement of tunes is introduced, where groups of free parameters are adjusted simultaneously to tune the simulation to more accurately describe distributions of a specific set of experimental data.

There are many tunes available in Pythia for different collision systems, where there has been an "evolution" of the tunes as new experimental data becomes available. The desired tune can be set, from a collection of existing options, when configuring the Pythia. The tune that will be primarily used in this work is the Monash 2013 tune [36], which is a widely used tune when performing proton-proton simulations relating to LHC energies. One of the aims of the Monash tune is to re-evaluate the constraints given by data from e^+e^- experiments such as LEP and SLD, in order to manually tune the parameters related to final-state radiation and hadronisation - as opposed to an automated approach used in previous tunes. Since the initial state of an e^+e^- collision is much cleaner than a hadron collision, it is best suited to tune these parameters that are related to the final-state [19]. The approach of the Monash tune is to then use minimum-bias, Drell-Yan, and underlying-event data from the LHC to manually tune the parameters related to the initial-state radiation and multi-parton interactions, where the NNPDF2.3 LO PDF set is also used.

3.1.2 Process Selection

Now that the collision system and centre-of-mass energy of choice has been set and tuned, it is necessary to specify the processes of interest to be generated and included into the total generated cross-section. By default in Pythia, all processes are switched off and the user is required to specify all the processes to be included. Pythia provides a long list of available processes, including Standard Model processes (up to LO or NLO) and even beyond the Standard Model, such as dark matter processes. In this work, the interest will be primarily on the Standard Model QCD processes, where the electroweak processes for the vector boson analysis will be generated using POWHEG.

The QCD processes available in Pythia are divided into two categories, namely soft and hard QCD. The soft-QCD processes encapsulates all elastic, diffractive and "minimum-bias" events that cover the total cross-section for all QCD processes [19]. In this simulation context, "minimum-bias" is strictly referring to all inelastic and non-diffractive events, which is slightly different from the experimental procedure of applying a minimal bias selection to the events that are recorded experimentally. In this work, the interest will be to study non-diffractive events, as these are the events where new particles of interest will be produced - such as HF quarks. Thus, only non-diffractive processes will be turned on when using soft-QCD. The soft-QCD processes are best suited for events that have a small momentum transfer in the hard partonic interaction. Thus, it is required to make use of hard-QCD to generated events with a larger momentum transfer in the hard partonic interaction. The transition between these two processes will be investigated more clearly in section 4.1.1.

The hard-QCD processes in Pythia encapsulates all the perturbative QCD processes of interest in this work, such as the $2 \rightarrow 2$ hard scattering that produces heavy-flavour quarks. It is important to note that the perturbative regime diverges in the limit as $p_T \rightarrow 0$, which will also be investigated in section 4.1.1. Thus, a minimum phase-space cut must be specified with $\hat{p_T}_{min}$ when making use of these processes to avoid divergent cross-sections, where soft-QCD can then be used to populate the rest of the phase-space. Since the soft-QCD framework also includes the implementation of the MPI model, it allows for a high-p_T tail [19]. Thus, it is important to not mix the hard-QCD and soft-QCD processes, as this will result in double counting. It is also possible to only turn on a subset of hard-QCD processes of interest, such as HF quark pair creation at LO. In this work, mainly the "minimum-bias" case will be considered for inclusivity - where all the hard-QCD processes will be turned on.

3.1.3 Phase Space Cuts and Re-weighting

It has already been mentioned that a phase-space cut needs to be applied to hard-QCD, in order to account for the divergence in the $p_T \rightarrow 0$ limit. For the $2 \rightarrow 2$ processes of interest, the $\hat{p_T}$-scale serves as a convenient classification of the event to perform a phase-space cut with, where $\hat{p_T}$ is the transverse-momentum transfer of the hardest process of the event [19]. Using $\hat{p_T}_{min}$ and $\hat{p_T}_{max}$, the total hard-QCD production cross-section can be split into non-overlapping segments. This is useful as a re-weighting technique, as events with a larger $\hat{p_T}$-transfer can be "forced" in order to obtain more events at the high-p_T tail of the desired distributions.

In this work, the events generated with hard-QCD will be split up into multiple bins using the described phase-space cuts. Each bin will cover a specific $\hat{p_T}$-range of the total hard-QCD production cross-section, and will be appropriately re-weighted by normalising with the bin's generated cross-section - which will be adjusted as necessary by Pythia for the applied phase-space cuts. This will have the benefit of obtaining more high-p_T events in order to improve the statistics at the tails of the desired distributions, as will be shown in section 4.1.4.

3.1.4 Decays

Unstable particles produced in Pythia have an associated decay table that contains the possible decay channels with their respective branching ratios. Each decay channel is described by a list of properties, such as specify whether the channel is turned on/off and allowed to happen or not, and the branching ratio of the channel [19]. Even though the decay tables are populated and configured by default in Pythia, the user has the freedom to change the decay properties of a particle of interest to adapt to the desired implementation.

It has already been shown in section 1.1.5 that a key interest in this work will be to investigate production of muons from HF hadrons in the forward rapidity region. Since the inclusive branching ratio of for example the D^+ meson to decay into a muon (plus anything else) is currently known to be $(17.6 \pm 3.2)\%$ [26], there are other possible decays that will happen that are not of interest. Thus, the decay table can be adjusted to improve the desired statistics by first turning off all possible decays, and then turning on only the decay of interest - in this example only muon channels will be turned on. It is important to mention that unlike the case of phase space cuts, the generated cross-sections are not automatically adjusted by Pythia when the user changes any of the decay properties. Thus, it is the responsibility of the user to scale the relevant cross-sections of the adjusted particles with the correct branching ratios at the analysis level.

Even though having the freedom to manually adjust decays as desired can have many benefits, such as being able to significantly improve the statistics of the process of interest; it can also lead to unexpected complications and incorrect results. For example, in the context of the HF muon production it can be naively thought that all D/B mesons can be forced to decay into muons and after scaling by the branching ratios it will give great improved statistics and the correct HF → μ cross-section. But, it has been shown that the $B \to D \to \mu$ channel is also of interest when considering the HF → μ cross-section. Thus, this channel's contribution will be lost if the B mesons are forced to decay directly into muons only. As in most cases, with great power comes the responsibility to use it with awareness and caution.

3.1.5 Event Information

Once the Pythia object has been configured as desired, it can then be used to generate as many events as the user wants for their analysis purposes. A generated event essentially refers to a list of generated particles (initial, final or intermediate) known as an event record, which can be iterated over and analysed as desired. There is a long list of classes and methods available in Pythia that can be used to access the desired physics information from the event record [19]. Each particle listed in the event record is represented with the `Particle` class, which can be used to access information about the particle. For example, the unique identified (ID) can be used to access the PDG code [26] of the particle, and the status property can be used to obtain information about what stage of the collision the particle was produced. There are also many other methods to access all of the available kinematics, and also importantly the decay daughters and originating mothers. In this work, these methods will be used in a variety of ways depending on the context of the analysis.

The full event itself is represented by the event record, which is made up of two main parts - namely the 'process' and 'event'. The main difference between the two is that 'process' contains only information about the hardest process, where the 'event' contains the full information about the rest of the event history [19]. The individual particles of the event record, as explained above, can then be iterated over and accessed individually. From this, the desired particle information can then be accessed with the mentioned available methods, such as the PDG code. From this, it is clear that a Pythia analysis will always have an 'event loop', where the full event record is iterated over to query all the produced particles of the generated collision event. Inside the event loop is where the unique algorithm for the specific analysis needs to be developed independently by the user to achieve their physics goal.

3.1.6 Total Generated Cross-section

Once all the events have been fully generated by Pythia, as configured, the final total event generation information can be accessed. For example, the statistics of the generated events can be outputted directly via the terminal - such as the number of generated events and total cross section for each separate process that was turned on during the process selection. The total generated cross-section of all the processes can be accessed, as well as its associated statistical error - which will be discussed more in section 3. The weighted sum of events is also important to access for normalisation purposes, especially in the case of making use of re-weighting when generating events - in the case of unweighted events this will simply be equal to the number of generated events [19]. In the case of generating events in different $\hat{p_T}$-bins, as outline in section 2.1.3, the total generation information will be accessed for each bin individually.

Now from the number of occurrences of an arbitrary process (N_{occur}), which is counted across all events during the event-loop analysis as outline in the previous section, the estimated cross-section of the arbitrary process of interest ($\sigma_{estimate}$) can then be obtain by first normalising with the weighted sum of events (N_{events}) and then scaling by the generated cross-section (σ_{gen}) - as shown in equation (3).

$$\sigma_X = N_{occur} \times \frac{\sigma_{gen}}{N_{events}} \tag{19}$$

3.1.7 User Hooks

Another available feature in Pythia that is important to mention is user hooks. Simply put, is it a software class that the user can derive from as a template and use to “step in” during different parts of the generation process - for example, to access the event record between the parton-level and hadron-level steps. This can be useful in many different scenarios, as it gives the user the freedom to make decisions such as to veto undesirable events and even collect statistics during the event generation process. A list of the available routines to step in at different stages of the generation process can be found in [19]. In this work, an already implemented user hook will be used to read in the generated hard partonic scattering event information for NLO vector boson production outputted by POWHEG, and then match it to Pythia's showering scheme to generate the rest of the event.

3.2 POWHEG BOX

The POWHEG BOX event generator will be used in this work to simulate the hardest scattering events of $W^{\pm} \to \mu^{\pm}$ production in high-energy proton-proton collisions at next-to-leading-order (NLO), for the analysis in section 4.3. Simply put, the POWHEG BOX program is a software framework used to implement NLO calculations for processes in Shower Monte Carlo (SMC) programs such as Pythia, according to the POWHEG (Positive Weight Hardest-Emission Generator) method [37]. The framework has been extended to include applications for many different processes, such as the electroweak processes of interest in this work.

3.2.1 The POWHEG method

With the evolution of theoretical studies for comparison to the data collected by collider experiments, it has become standard practice to use NLO computations as a tool for comparison. In the context of general purpose SMC programs, leading-order (LO) calculations have been used as the primary tool. Due to the positive success of theoretical tests at NLO, it has become highly encouraged for SMC programs to be improved to include NLO calculations. This would result in a large amount of the knowledge of the NLO corrections to become more directly available to experimentalists that perform simulation studies [38] - where this benefit will be directly applicable in this work.

The main problem that arises when attempting to merge NLO calculations with SMC programs is to not over-count, as there are SMC programs that already implement approximate NLO corrections to the obtained cross-sections [38]. The first solutions that were developed to account for this problem made use of a subtraction method, where the corrections from the SMC program can be calculated and subtracted from the obtained cross-sections to avoid over-counting. The subtraction term can be calculated analytically and only needs to be determined once, since it turns out to be process-independent. With the subtraction method, there is nothing that prevents the result from being negative, which means that events with negative weights can be generated. The POWHEG method was then proposed as a strategy to prevent the generation of negatively weighted events. Simply put, the POWHEG method achieves this by generating the hardest radiation first, with some additional techniques that guarantees the events to be positively weighted. This then gives advantage of being able to interface the output from POWHEG with any SMC program that is p_T-ordered - as is the case for Pythia.

3.2.2 LHAPDF

The core ingredient that needs to be inputted to POWHEG is the PDF of choice. Unlike the case of Pythia, there aren't many default options for PDF sets to be use in POWHEG - the PDF of interest in this work is not available by default. Thus, an additional library is required to retrieve, manage and interface the additional PDF sets with POWHEG. In this work, the LHAPDF 6 library [39] will be used to serve this purpose. It is a software library, written in Fortran, that provides standardised access to parton distribution functions for both experimental and theoretical studies. The 6th edition of the library offers a range of improvements, such as improved CPU performance. Thus, it will be used in this work to input the NNPDF2.3 QCD+QED LO PDF set to POWHEG.

3.2.3 Pythia Matching

As already mentioned, POWHEG serves as a NLO calculation of the hardest process that can be used as input to Pythia to generate the rest of the event. Since both programs are based on evolutions that are p_T-ordered, they can be matched in an ideal manner [19]. The main challenge that arises when matching/merging POWHEG with Pythia is that the "hardness" of the event is defined differently in each program. This can result in potential mismatches or double-counting occurring if the matching is not done carefully. Due to this, there are also additional free parameters that arise from the matching procedure. As recommended in the documentation, the default parameters will be used in this work to avoid any of the potential complications.

3.3 O^2 Software Framework

The Online-Offline (O^2) Software Framework was developed by the ALICE Collaboration as part of the upgrades for the Run 2 data-taking period. The upgrade was aimed at addressing the challenge of reading out lead-lead collisions at a rate of 50 kHz and proton-proton collisions up to 200 kHz. Combined with an improvement to the tracking precision in both the central and forward rapidity regions, this results in the data volume of lead-lead collisions being on the order of 100 times larger than in Run 1 [40]. Thus, the O^2 software framework was developed in order to serve as the full data-processing pipeline from online detector reconstruction to offline physics analysis, to refine and reduce the amount of data that needs to be read out to storage and also provide efficient analysis tools. The complete O^2 software can be found at `https://github.com/AliceO2Group/AliceO2`. Even though it is publicly available as a github repository, the user is required to have the relevant certificate to have access to run it locally.

The O^2 software framework can roughly be divided into four main parts. The most important part is the "core" O^2 repository, which is responsible for the majority of the online and offline processing of the data - such as all the detector reconstruction. The "core" part is a necessary base that needs to be installed for all the other parts to function. The second part is the O^2-Physics software, which provides all the functionality for the experimentalists to perform physics analysis on the data that gets outputted by the reconstruction pipeline - the data will be in the format of Analysis Object Datafiles (AOD). The third part is the Quality Control (QC) software, which runs in parallel with the reconstruction pipeline in order to monitor the quality of the data along each step. The final and most relevant part is the O^2-Simulation software, which will be used in this work and discussed in more detail in the next section.

3.3.1 Simulations

The objective of the O^2-Simulation software is to generate large samples of simulated hadronic collisions with a "realistic" detector response, to resemble real experimental data as closely as possible. To achieve this, there are multiple steps involved. Firstly, the physics of the hadronic collisions need to be simulated from the relevant theoretical models - as outlined for proton-proton collisions in section 2.2. This step is handled mainly by Pythia, which is integrated into the O^2 framework. Secondly, the passage of the simulated particles, produced in the collision, through the detectors needs to be simulated - where the matter distribution needs to resemble the actual detectors as closely as possible (done using GEANT4 [41]). To achieve this, the analogue detector response is firstly simulated, followed by the digitization step to obtain the raw data as outputted by the detector. Using this, the simulated events can then be reconstructed and analysed in the same manner as real experimental data 3.3.1. The advantage this provides is that the Monte Carlo information is available in addition to the reconstructed data, which can be used to study properties of the detectors - such as the resolution and efficiency.

In this work, the O^2-Simulation software will be used to simulate the detector response of generated $W^\pm \to \mu^\pm + \overset{(-)}{\nu}_\mu$ events. The stand-alone events generated by POWHEG can be used as input, where the rest of the simulation pipeline is handled by the O^2 software. Even though the software provides a lot of customisability to be configured for many applications and collisions systems, the default for proton-proton collisions with Pythia (Monash Tune) is used. An additional software trigger is developed to only simulate the detector response for events where the produced μ lies in the η-region of the muon spectrometer. The feature to only simulate the response of detectors of interest is currently still under development. Thus, the transport of all produced particles through the full detector is simulated - this results in the simulation being extremely computationally expensive. Finally, the simulation output (in the AOD format) can be accessed and analysed with the O^2-Physics software - the results of the analyses will be presented in section 4.4.

3.4 High-Performance Computing Environment

All of the simulation and analysis software used to produce the results in this work, with the exception of O^2-simulations, was run on the University of Cape Town's ICTS High Performance Computing (HPC) cluster [42]. This provided critical computing resources to run the computationally intensive simulations. Within the HPC environment, computing jobs can be allocated with multiple computing cores, which can be utilized by Pythia to run many events in parallel - this advantage will be emphasized in section 4.2.3. In addition to computing cores, large storage space is also provided to store the simulation output files.

4 Analysis and Results

All the results presented in this section was constructed using the MC event generators and software libraries discussed in section 3. The developed code used to run the simulations, analyse the results and format the plotting can be found at: `https://github.com/comrademarvin/Pythia-Analysis`.

Unless stated otherwise, the default tune used to configure Pythia for proton-proton collisions (no other collision system is considered) will be the Monash 2013 Tune - as introduced in section 3.1.1. In the case of POWHEG, the same PDF set as the Monash tune (NNPDF2.3 LO) will be used in the configuration to generate the $W^{\pm} \to \mu^{\pm}+\overset{(-)}{\nu}_{\mu}$ events. When matching to Pythia for showering, the suggested default matching parameters will be used and the Monash tune will also be set to configure the rest of Pythia to generate the underlying event and partonic showering.

In section 4.2.1 it will be shown how the "minimum-bias" (Pythia definition for QCD processes) events are generated within Pythia, which will be used to obtain the results presented in the heavy-flavour and primary charged-particle multiplicity sections. After this, POWHEG+Pythia matching will be used to obtain full $W^{\pm} \to \mu^{\pm}+\overset{(-)}{\nu}_{\mu}$ events, which can be used in combination with the minimum-bias multiplicity results to obtain the multiplicity dependence for the $W^{\pm}$ boson production. The stand-alone POWHEG events are also used as input to the O2 simulations to generate the "detector realistic" events of reconstructed muons originating from $W^{\pm}$ decays - where O2 also uses Pythia for showering. Before presenting the simulation results, the relevant uncertainties that will be included in the presented results will be discussed in the coming section.

4.1 Uncertainties in the Analysis

Roughly speaking, the uncertainties encountered in an analysis can be split into two categories - statistical and systematic uncertainties. The former refers to the spread in the results that arises when conducting the same experiment many different times, keeping the conditions and choice of parameters the same. Ideally, the statistical uncertainty can always be improved to increase the precision of the result by repeating the experiment as many times as possible to obtain more statistics. For example, in high-energy collider experiments, many hadron collisions are performed at a high luminosity in order to obtain as many events of interest as possible to increase the precision of the desired observable - like the measured mass of the vector boson mentioned previously. In the context of this thesis, computational techniques (like multi-threaded programming) are employed in order to simulate as many events of interest as possible, while also minimizing the required computational resources and runtime.

In the case of systematic uncertainties, things are unfortunately more complicated. This category of uncertainties refers to a spread in the results that arises when measuring the same quantity with a different experimental setup or varying the values of the free parameters. Unlike the case of statistical uncertainties, systematic uncertainties can be seen as intrinsic "flaws" of the experimental or simulation procedure. Thus, they cannot be improved or eliminated by merely repeating the experiment more times [43]. For example, in a physics simulation the results can be biased by selecting a specific value for a parameter that is free to take on a range of values - like the selection of a value for α_s. The effects of this bias will persist in the results, no matter how many repetitions of the simulation is performed.

In this section, the statistical and systematic uncertainties present in the physics simulations and analysis of this work will be discussed. Specifically, if and how they are accounted for in the results presented in this section.

4.1.1 Simulation Systematic Uncertainties

The majority of the analysis in this work will be done with pure Monte Carlo physics simulations, where detector effects will only be included in section 4.4. Thus, the contributing systematic uncertainties will arise from the theoretical models used in the simulation. It has already been shown in section 3.1.1 that there is a long list of free model parameters that need to be tuned when configuring the simulation. By selecting a specific set of free parameter values with a tune, the results are being biased. Ideally, this needs to be accounted for by considering the relevant systematic uncertainties that arise due to these free parameters. As already mentioned for the case of matching between POWHEG and Pythia, this gives rise to additional free parameters, where there is no obvious way to estimate the systematics from this. One way to account for the simulation model systematics is to re-run the simulation many times for a range of values of a free parameter, to estimate the uncertainty that arises in the obtained results. Unfortunately, this is not a very realistic approach, as it requires a large amount of computational resources and time.

Even in the case of the more "fixed" inputs to the simulation, there are inherent measurement or theoretical uncertainties attached to them - such as those given for the particle masses and decay branching ratios in [26]. The PDFs that are used also come with associated uncertainty bands that arise due to the limitations of the available data used for the fits. This is why a primary motivation in this work is the measurement of the $W^{\pm}$ boson in the forward region, to aid with constraining the PDF uncertainties as small Bjorken-x. Thus, it will not be within the scope of this work to properly account for all the relevant systematic uncertainties present in the simulation. It will merely be shown how the final resulting distributions change when making use of different tunes.

As already mentioned in section 3.1.2, there is an error estimate that is provided for the total generated cross-section of the considered processes in Pythia. It is important to mention that this provided error estimate does not take any of the mentioned systematic effects of the simulation into account, it purely represents the statistical uncertainty associated with the number of events that were generated to determine the cross-section [19]. Even though this statistical error becomes negligible in most cases, as the number of generated events is large, it is still propagated into the analysis when scaling the obtained distributions with the generated cross-section. The rest of the relevant statistical and propagated uncertainties will be discussed in the next section.

4.1.2 Statistical and Propagated Uncertainties

In the context of the analysis, where many simulated events (order of millions) of proton-proton collisions will be considered, and with the interest being mostly about cross-section probability distributions of processes/observables, it's only natural to make use of histograms. Due to this, it is important to consider the statistical uncertainties associated with making use of histograms to count the events/particles of interest. Even though the variable of interest can be a continuous variables (like transverse momentum), there will always only be a finite amount of statistics available. Therefore, it is necessary to make use of a finite binning approach to investigate an approximated distribution of the continuous variable - there will always be uncertainties associated with this approach!

Depending on the number of variables of interest at a given time, histograms with different dimensionalities can be utilized. In this work only histograms with one or two dimensions will be used, where the one-dimensional case will be discussed first. Consider a continuous variable X, which is defined in the range $x_{min} \leq x < x_{max}$. For example, the rapidity of a particle measured in a detector, where the rapidity range is restricted by the rapidity acceptance region of detector. The approach of the histogram is then to segment this range into an arbitrary choice of M bins, numbered here by $j = 1, ..., M$. The widths of the bins can then be equally assigned as $\Delta x = (x_{max} - x_{min})/M$. There is also the freedom to alternatively choose bin widths that are not equal in width, which will be seen in some of the figures in the analysis.

Now that a discretely binned range of X has been defined, the dataset x_i (labeled as $i = 1, .., N$ for N entries) can be be filled into the histogram by assigning each entry to a unique bin. After this is done, each bin will have a yield H_j, corresponding to the count of entries assigned to that bin. At this stage it is already possible to normalise the obtained histogram by the number of entries N, to obtain the relative frequency for each bin h_i as

$$h_i = \frac{H_i}{N}. \tag{20}$$

In most cases, the relative frequency h_i represents the probability p_i of an occurrence of the variable X lying within the range $x_{min,i} \leq x < x_{max,i}$. In the case where $N \to \infty$, the relative frequency will represent the integral (over a bin) of the continuous probability distribution function (here denoted by $\rho(x)$) of the variable of interest as

$$\lim_{N\to\infty} h_i = p_i \equiv \int_{x_{min,i}}^{x_{max,i}} \rho(x)\, dx. \tag{21}$$

The fundamental theorem of calculus states that there exists a value $x_{i,0}$ within the bin range such that

$$\int_{x_{min,i}}^{x_{max,i}} \rho(x)\, dx = \rho(x_{i,0})\Delta x_i, \tag{22}$$

which then yields a description of the PDF at the point $x_{i,0}$ as

$$\rho(x_{i,0}) = \frac{p_i}{\Delta x_i}, \tag{23}$$

where this will correspond to an estimate of the probability distribution function in the case of finite N as

$$\rho_{estimate}(x_{i,0}) = \frac{h_i}{\Delta x_i}. \tag{24}$$

In reality, there will never be infinite statistics available. Thus, it is necessary to consider the uncertainty associated with h_i, in order to quantify how well it estimates p_i. Considering the case where there are no bin-to-bin correlations, such that successive measurements of x are uncorrelated, the statistical fluctuation of the entries in each bin H_i will follow a Poisson distribution, with some mean μ_i. From the properties of the Poisson distribution, the variance of the bin is then given by $Var[H_i] = \mu_i \approx H_i$ - which yields a standard error (one standard deviation) of $\sqrt{H_i}$. The relative error on $\rho_{estimate}$ can then be shown to be [43]

$$\frac{\delta\rho_{estimate}}{\rho_{estimate}} = \frac{\sqrt{h_i/N}}{h_i} = \frac{1}{\sqrt{N}}\frac{1}{\sqrt{h_i}} = \frac{1}{\sqrt{H_i}}. \tag{25}$$

It is clear that the relative error will decrease as the available statistics increases, as claimed earlier. In this work, the statistical uncertainties will be determined by the ROOT library, which applies the error of $\sqrt{H_i}$ as outlined above [44]. Since the simulated events being analysed are generated in isolation from another, they can be taken to be statistically independent and it is valid to consider the bins as being Poisson distributed. In the case of histograms with higher dimensionalities, the same result can be shown to hold for each bin [43].

After the histograms have been filled with entries, they are normalised by the total number of events and bin widths to obtain an estimate of the distribution of the process of interest. The relevant statistical error is then determined for each bin as explained above. When any kind of operation or arithmetic is then applied on the normalised histograms, ROOT will propagate the statistical uncertainties accordingly [44].

For example, to obtain a cross-section for the process of interest from the normalised histogram, it is scaled by the total generated cross-section given by Pythia. The statistical error estimates given for the generated cross section and the resulting bin errors are then propagated as needed by ROOT.

Another special case of statistical uncertainties that is important to talk about is when constructing a profile histogram. This is a method of visualizing a two-dimensional histogram (with parameters X and Y) by taking the average of the Y-values for each X-bin. Since an average is being considered, there is an uncertainty associated that depends on how the Y-values are distributed. In ROOT, there are a few options available to determine the relevant error when constructing a profile histogram. The default option considers the Y-values to be Poisson distributed, and thus calculates the error as $\sqrt{Y}/\sqrt{N}$, where N is the number of Y-values per X-bin [44]. This will be relevant in the analysis when considering the yield of decay muons from $W^{\pm}$ boson as a function of p_T and the charged-particle multiplicity.

The last source of uncertainties to consider will be that which arises when applying a fit to the resulting distributions. Only a weighted linear fit will be used in this work, which will implement the Chi-square fit method. As the fit will be applied to distributions given by histograms, the input weights will be given by the associated bin errors as outlined in this section. The resulting uncertainties on the fit parameters can then be accessed via the outputted covariance matrix given by the fit results [44].

4.2 Minimum Bias

In this section, “minimum-bias” (MB) will refer to the Pythia definition of inclusive QCD processes - as presented in section 3.1.2. It is important to mention that this does not include electroweak boson production - this will be generated separately with POWHEG up to NLO for section 4.3. In order to reliably and correctly generate minimum-bias events with Pythia, it is first necessary to look into the interplay between the available soft-QCD (non-perturbative) and hard-QCD (perturbative) processes in the following section - where the necessity for the distinction was introduced in section 2.1.4.

At this stage it is important to mention that the term ‘minimum-bias’ is an experimental concept, where it refers to a minimally biased trigger. For example, in ALICE, the minimum-bias trigger is sensitive to the total production of inelastic collisions (non-diffractive) [45]. Thus, it can be argued that generating inclusive non-diffractive QCD processes and referring to it as “minimum-bias” is not very far off from the experimental definition, and the two can be meaningfully compared.

4.2.1 Total Production Cross-section

In section 3.1.3, it was argued that the $\hat{p_T}$-scale serves as a convenient classification of the event - which can be used to reliably perform phase-space cuts. In Figure 24, it shows the $\hat{p_T}$-dependence of events generated with non-diffractive soft-QCD and inclusive hard-QCD separately at $\sqrt{s} = 5.36$ TeV - where both represent the full minimum-bias cross-section. It can be clearly seen that the hard-QCD starts to diverge below $\hat{p_T}$ values of approximately 10 GeV, which is to be expected - as argued in section 2.1.2. Thus, this can be used as a cut-off value (labelled as $\hat{p_T}_{switch}$), where non-diffractive soft-QCD will be used to generate events with $\hat{p_T} < \hat{p_T}_{switch}$ and hard-QCD will be used to generate events with $\hat{p_T} >= \hat{p_T}_{switch}$ - in order to avoid a divergence of the total production cross-section. Using this technique, the final total production cross-section of minimum-bias events at $\sqrt{s} = 5.36$ TeV can be seen in Figure 25. Despite switching between processes with a phase-space cut, the curve of the total generated cross-section is still “smooth” and without any kinks or irregularities around $\hat{p_T}_{switch}$ as desired. It is important to mention that the $\hat{p_T}_{switch}$ value will change as a function of $\sqrt{s}$, so it needs to be redetermined when changing the centre-of-mass energy - as shown for $\sqrt{s} = 13.6$ TeV in Figure 48.

In addition to using the $\hat{p_T}_{switch}$ value as a cut-off to switch between processes, it is also possible to use the same $\hat{p_T}_{min}$ and $\hat{p_T}_{max}$ phase-space cuts to further sub-divide the generation of hard-QCD events into $\hat{p_T}$-bins - the same is not possible for the soft-QCD events. The main advantage this provides is to “force” more events with larger $\hat{p_T}$ values, while then normalising properly to obtain accurate cross-sections

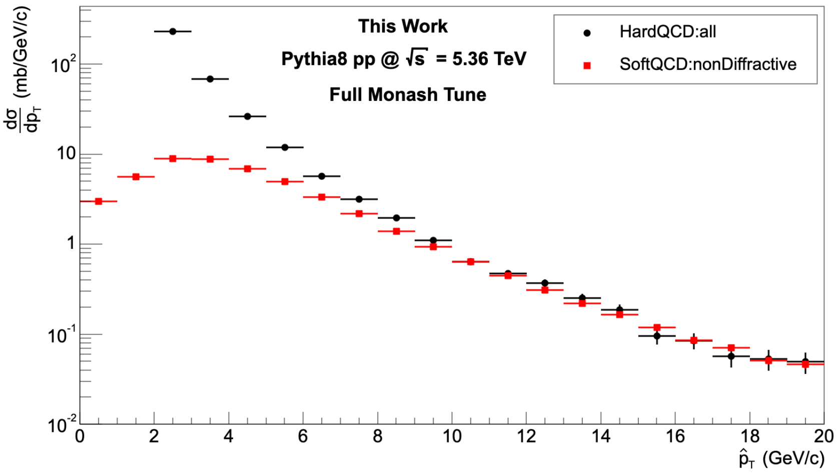

Figure 24: The $\hat{p}_T$-differential cross-section of the soft (non-diffractive) and hard QCD processes in Pythia at $\sqrt{s} = 5.36$ TeV.

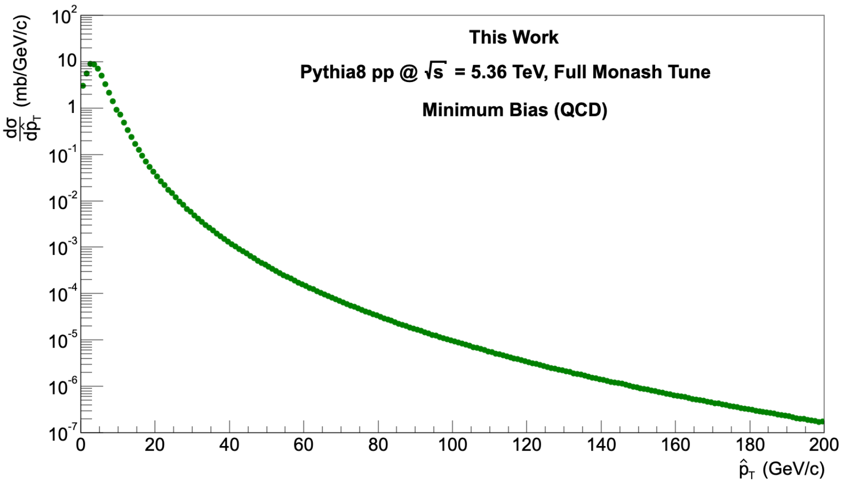

Figure 25: The $\hat{p}_T$-differential cross-section of the total generated minimum-bias (QCD) cross-section in Pythia at $\sqrt{s} = 5.36$ TeV.

- this will become useful in section 4.2.3. It also has the advantage of allowing the different $\hat{p}_T$-bins to be generated in parallel, which can particularly utilize the multi-core environment of a computing cluster to reduce the runtime required to generate a large number of events - as introduced in section 3.4. There can be drawbacks to using this approach, so it is important to choose the $\hat{p}_T$-bin ranges carefully. Otherwise, there can be kinks or discontinuities in the obtained cross-section distributions, which can arise from binning effects - such as large uncertainties at the end of the bin range.

4.2.2 Charged-Particle Multiplicity

As mentioned in section 1.2.4, in this work ALICE's definition of primary charged-particle multiplicity will be considered. For this, an algorithm was developed to follow the pseudo-code laid out in [24] - to count the number of primary charged particles per event (N_{ch}), where only events with $N_{ch} > 0$ will be considered. As introduced in section 1.3.2, there are two detectors used in ALICE to estimate the primary charged-particle

Table 3: Mean and RMS values for the minimum-bias multiplicity distributions in Figure 27.

	Full	MPI off	CR off
$< dN_{ch}/d\eta >$	6.31	3.04	8.40
RMS of $dN_{ch}/d\eta$	4.97	1.69	7.67

multiplicity (ITS and V0C) - which cover different η-regions. In Figure 26, it shows the obtained primary charged-particle multiplicity distributions for three different ALICE detector η-regions; where the muon spectrometer region has been included to aid with the discussion that will follow in section 4.3.4. It can be seen that the ITS in the central region and V0C in the forward region produce almost identical distributions, where the slight differences are not relevant - as the multiplicity will be normalised in the coming sections. The argument to specifically choose the central region for multiplicity estimation in this study will be laid out more clearly in section 4.3.4.

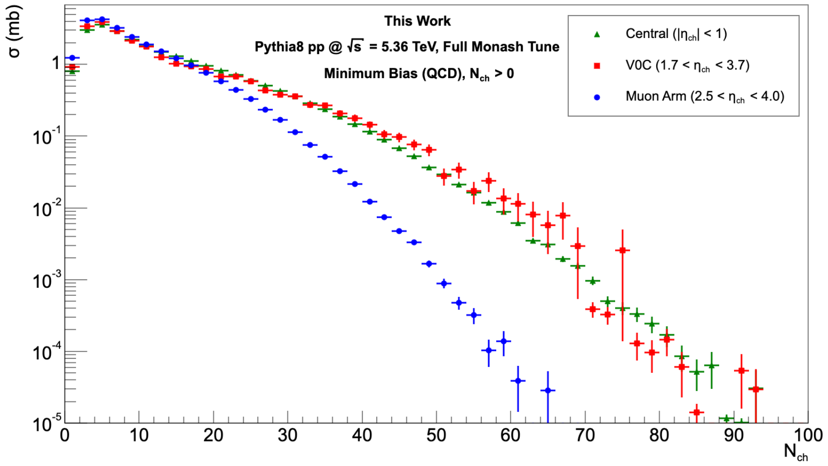

Figure 26: Minimum bias charged-particle multiplicity distributions, for different ALICE detector η-regions, at $\sqrt{s} = 5.36$ TeV using Pythia.

Now focusing only on the central region, in Figure 27 it shows the same multiplicity distribution of minimum-bias in the central region (using the full Monash 2013 Tune); as well as the multiplicity distributions when turning off the MPI and CR models individually - which can be compared to Figure 3 as a reference. Even though the centre-of-mass energies are different, the shapes of the obtained distributions seem to be consistent. The obtained averages and root-mean-square errors (RMS) of the multiplicity per unit of η ($< dN_{ch}/d\eta >$) distributions are listed in Table 3 - where $dN_{ch}/d\eta = \Delta N_{ch}/\Delta\eta = N_{ch}/\Delta\eta$ and $\Delta\eta$ is the range of the η-region ($\Delta\eta = 2$ for the central region). The averages will become important later, for normalisation purposes in section 4.3.3. It can be expected that turning off only MPI would result in a much faster drop-off of the minimum-bias multiplicity distribution, as only the hardest interaction, initial/final state showers and beam-remnants would contribute to the production of charged particles - as opposed to additional multiple partonic scatterings also contributing. From the discussion in section 2.2.6, it is also to be expected for the multiplicity distribution to instead drop-off slower when turning off only CR, as the CR model is implemented to minimize the string lengths through reconnection strategies between the colour charges - where a reduced string length will results in a reduced number of charged hadrons being produced in the shower.

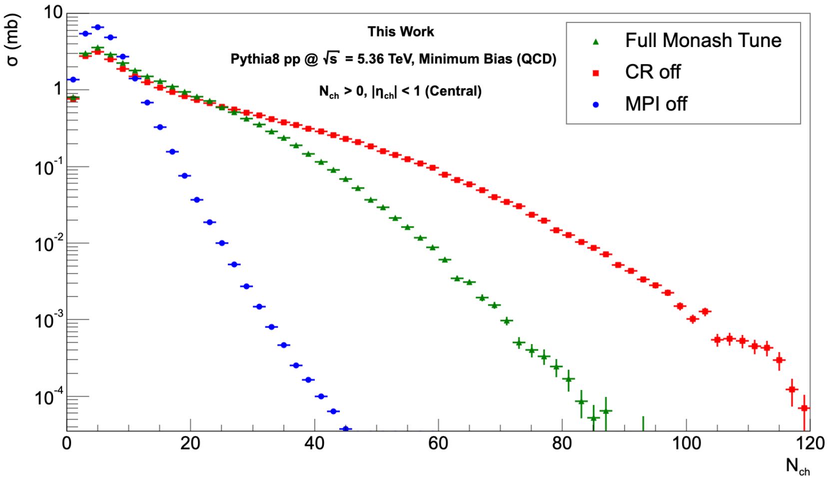

Figure 27: Minimum bias charged-particle multiplicity in the central region ($|\eta| < 1$), showing the effects of turning off MPI and CR respectively.

4.2.3 Heavy-Flavour Mesons

It has been motivated that the focus in this work will be specifically on decay muons that can be detected in the forward region of the ALICE muon spectrometer. Thus, only final-state muons in the $2.5 < \eta < 4.0$ region will be considered from this point onwards. In Figure 28, it shows the contributing sources to the forward muon production in minimum-bias. Due to a lack of statistics, it is not possible to extend the upper-bound of the p_T of the decay muons higher than 40 GeV - where an upper-bound of 80 GeV would have been preferable to compare more clearly at high-p_T with the production of muons from HF and $W^{\pm}$ boson decays in Figure 31. It is clear that the dominant source of muons in the considered region is from the HF meson decays, which will be the focus in this section. There are also other sources, such as light hadrons (containing only up, down and strange valence quarks), different baryon species, lepton decays (tau) and boson decays (specifically photons in the minimum-bias case). These additional sources in minimum-bias will not be focused on in this work, as they will not contribute significantly to the background for the $W^{\pm} \rightarrow \mu^{\pm} + \overset{(-)}{\nu}_{\mu}$ process at high-p_T values - which will be discussed more in section 4.3.1. It is important to mention that by default in Pythia, pions and kaons (both light hadrons) are set to not decay. Thus, their contribution to the background is not shown in Figure 28. In this work, it will also be assumed that they are long-lived enough to be stopped by the front absorber of the ALICE muon spectrometer - before being able to decay into muons that can be detected. When aiming for a fully realistic study of the forward muon production in data, this assumption will not exactly hold and the contribution from pions/kaons needs to be considered.

Now focusing only on HF mesons decays, the approach developed to identify the HF$\rightarrow \mu$ processes within the Pythia event record can be briefly discussed. It is firstly important to mention that full minimum-bias events, as discussed in section 4.2.1, were generated in order to extract the HF$\rightarrow \mu$ processes. Even though it is possible to force events with HF pair production in the hardest interaction (as mentioned in section 3.1.2), this would exclude the contribution from events where HF quarks are created during other stages of the collision, without there being HF pair production in the hardest interaction - such as initial and final state showers. In order to also obtain an accurate cross-section at low-p_T, it is necessary to make use of soft-QCD processes to tame the divergence in this region. The contribution to the HF$\rightarrow \mu$ cross-section from the different $\hat{p}_T$-bins is shown in Figure 49. It can be seen that the contribution falls off as a function of $\hat{p}_T$, making it valid to have an upper-limit for $\hat{p}_T$ as an approximation. As anticipated, it can also be seen that soft-QCD serves as the dominant contribution in the low-p_T region. Thus, it needs to be included to obtain a full and accurate cross-section.

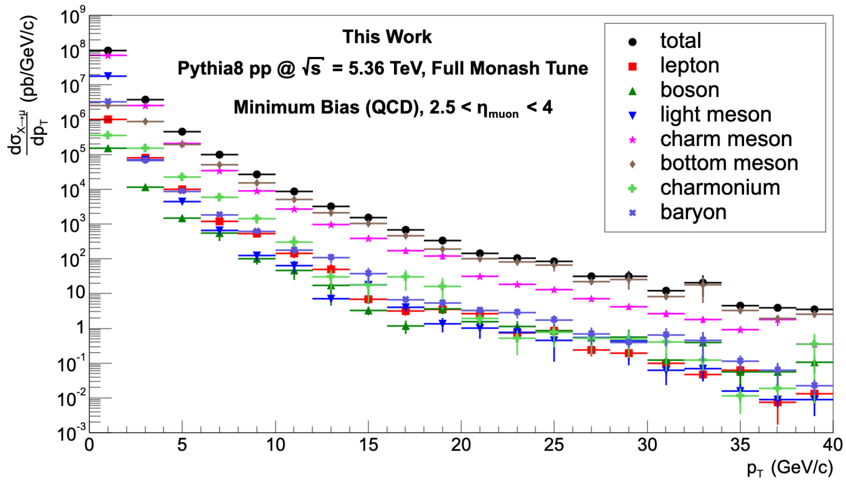

Figure 28: Contributions to production of muons from decays in the forward η-region of proton-proton collisions, at $\sqrt{s} = 5.36$ TeV with Pythia.

Now, identifying the HF$\rightarrow$ μ processes can be looked at more closely. For this, a "backwards" approach is used, where final-state muons are looked for first - the tree of mothers is then backtracked along to look for HF mesons. After identifying the final-state muon, it is also necessary to first backtrack along a chain of "copy" muon entries - which can result from the decay muon emitting photons and losing some energy. Once the direct decay muons are identified, it is backtracked along the mother tree to look for the following processes: $c \rightarrow D' \rightarrow ... \rightarrow D \rightarrow \mu$, $b \rightarrow B' \rightarrow ... \rightarrow B \rightarrow \mu$ and $b \rightarrow B' \rightarrow ... \rightarrow B \rightarrow D' \rightarrow ... \rightarrow D \rightarrow \mu$. Here D'/B' are the HF mesons formed directly by the hadronisation process of the c/b quarks that originate from any of the production mechanisms discussed in section 1.2.5. It is also possible for the D'/B' mesons to have a chain of "copies" that result from other non-decay process, such as transitioning from an exited state, where D/B are then the final entries of the mesons that decay leptonically into muons. With the inclusion of these processes, the theoretical HF$\rightarrow$ μ cross-section in proton-proton collisions at $\sqrt{s} = 5.02$ TeV can be obtained using Pythia.

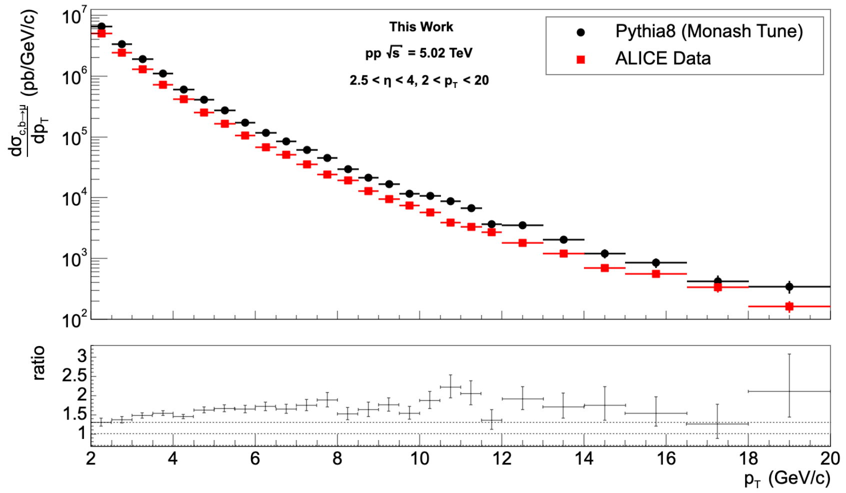

Figure 29: The p_T-differential cross-section of HF$\rightarrow$ μ in the forward region of proton-proton collisions at $\sqrt{s} = 5.02$ TeV with Pythia (Monash Tune), compared to the experimentally published results by ALICE [27]

As full minimum-bias events are being generated to extract the described HF→ μ cross-section, this strongly increases the number of events that need to be generated in order to obtain good statistics. To aid with increasing the statistics, the D^0 and $D^{\pm}$ will be forced to decay into muons, as described in section 3.1.4 - where the cross-section is then correctly scaled by the branching ratio to obtain the correct result. In additional to this, the $\hat{p}_T$-bins are run in parallel as separate jobs on the high-performance computing cluster - which reduces the runtime by a factor of the number of $\hat{p}_T$-bins used. The events in each bin can further be generated in parallel using multiple computing cores for each job on the cluster, with the inclusion of the Pythia-parallel library - this will further reduce the runtime by a factor of the number of cores used per job. With the combination of the listed strategies, the HF→ μ statistics can be significantly increased by running many minimum-bias events in parallel and forcing muonic decays.

In Figure 29, the obtained theoretical HF→ μ cross-section, using Pythia minimum-bias, is given in comparison to the published ALICE results from Run 2 data [27]. Even though the obtained Pythia result is on the same order as the experimental data, it is slightly larger by a factor of roughly 1.5-2 times in most of the p_T-bins. A reason for the difference could be due to detector effects, since these effects were not included in the "pure" Pythia simulation. However, it is shown in [27] how the result from data is adjusted for detector effects, such as scaling the measured cross-section by the efficiency of the detector - this efficiency will also be further investigated for the $W^{\pm} \rightarrow \mu^{\pm} + \overset{(-)}{\nu}_{\mu}$ process in section 4.4.1. Thus, it can be expected that the measured cross-section should match closely to the theoretical simulated cross-section from Pythia.

At this point it is important to remember that the uncertainties given for the Pythia simulation results only represents the relevant statistical uncertainties, as laid out in section 4.1.2. Thus, it does not include any of the systematic uncertainties associated with the free parameters of the models used in the simulation - as mentioned in section 4.1.1. To investigate this further, the same HF→ μ cross-section was determined using different tunes available in Pythia - as discussed in section 3.1.1. In Figure 30, it can be seen that using different tunes will bias the obtained HF→ μ cross-section to an observable extent. This enforces the argument that the simulation systematic uncertainties can not be considered negligible when hoping to achieve an accurate representation of the all relevant uncertainties of the result. It also emphasizes the importance of using the correct tune when hoping to accurately obtain specific physics results. Since the Monash Tune serves as a "general purpose" tune, it is not optimised for HF processes and can lead to the observed deviation - assuming there are no other systematic errors in the algorithm.

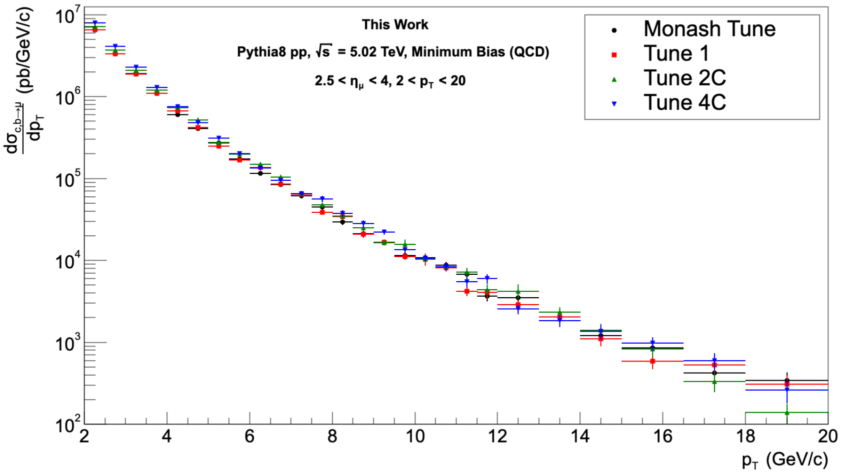

Figure 30: The p_T-differential cross-section of HF→ μ in the forward region of proton-proton collisions at $\sqrt{s} = 5.02$ TeV with Pythia, showing the effects of using different Pythia tunes.

4.3 Vector Boson

For this section, the $W^{\pm} \rightarrow \mu^{\pm} + \overset{(-)}{\nu}_{\mu}$ events will be generated up to NLO using POWHEG - as previously discussed. The default configuration provided in POWHEG for LHC-energies will be used, with the addition of the LHAPDF library to set the required PDF (same set used in the Monash 2013 Tune) - as introduced in section 3.2.2. It is important to mention that POWHEG generates $W^{+} \rightarrow \mu^{+}$ and $W^{-} \rightarrow \mu^{-}$ independently. Thus, in the analysis they will also be treated separately, up until the point where they can be combined at the cross-section level - as it is important to first properly normalise before combining them. For the multiplicity analysis, it is also necessary to implement the POWHEG+Pythia matching/merging hook to generate the rest of the event with Pythia - as introduced in section 3.1.7. As also discussed in section 3.2.3, the matching/merging procedure introduces additional free parameters that need to be set. In this work, the recommended default parameters will be used.

4.3.1 Hadronic Background

In section 4.2.3, the HF→ μ cross-section in the forward η-region of proton-proton collisions was presented. It was also argued that the HF meson muonic decays will serve as the dominant background for the decay muons from $W^{\pm}$ decays in this η-region - especially at high-p_T. Within the experimental context it is critically important to consider the background contributions. It might be fairly trivial in simulations to distinguish between the contributing processes, as there are identifying labels available for all particles, but in the realistic detector case it is not nearly as simple. The detector will merely detect and identify muons, it is then the task of the analyser to develop techniques to distinguish between the different sources. There exist multiple strategies to extract the desired signal from the inclusive experimental data. One of the classical approaches is to use the simulated cross-sections of the known background contributions to subtract them from the inclusive experimental cross-section to obtained the desired signal - this is known as background subtraction. Thus, investigating the relevant background contributions with simulations can already serve as a useful step to perform the data analysis.

In Figure 31, it compares the obtained theoretical HF→ μ and $W^{\pm} \rightarrow \mu^{\pm} + \overset{(-)}{\nu}_{\mu}$ cross-sections in the forward region at $\sqrt{s} = 5.36$ TeV, using POWHEG and Pythia. At this stage, the upper p_T-limit has been extended up to 80 GeV/c - it can be extrapolated from Figure 28 that it is valid to assume only HF meson decays will contribute strongly in this region. From Figure 31, it is clear that the HF muons serve as a non-negligible background when looking for muons from $W^{\pm}$ boson decays - even in the high-p_T region. Up until roughly 30 GeV/c, the HF background is the dominant contributor to the inclusive forward muon cross-section. For p_T-bins larger than this, the muons from $W^{\pm}$ boson decays become the dominant contributing process - due to the drop-off of the HF cross-section as a function of the decay muon p_T. Thus, the production of muons from $W^{\pm}$ decays can meaningfully be studied in the high-p_T region. This also motivates introducing a lower p_T cut of 30 GeV/c when looking for muons from $W\pm$ boson decays - which will be implemented when performing the multiplicity analysis. From experimental motivations, an upper-p_T cut of 60 GeV/c will also be introduced for the multiplicity analysis.

Up until now, only the contributing background from minimum-bias events has been considered. What about muons that originate from other electroweak processes? Or even quarkonia? The most important other sources to mention are the neutral weak boson (Z^0) and J/ψ (bound state of $c - \bar{c}$ pair) decays. In both case, the decay will be to a pair of oppositely charged muons. As this process has a different decay topology, it should in principle be easier to distinguish from the $W^{\pm} \rightarrow \mu^{\pm} + \overset{(-)}{\nu}_{\mu}$ events and will not be considered in this work - in a realistic experimental study these sources must be considered. It is clear that one of the primary challenges when performing this study on data will be to obtain as pure of a $W^{\pm} \rightarrow \mu^{\pm} + \overset{(-)}{\nu}_{\mu}$ signal as possible. Performing the lower p_T cut will not be sufficient enough and other tools, such as background subtraction or potentially machine learning, will have to be employed to efficiently get rid of the background contributions.

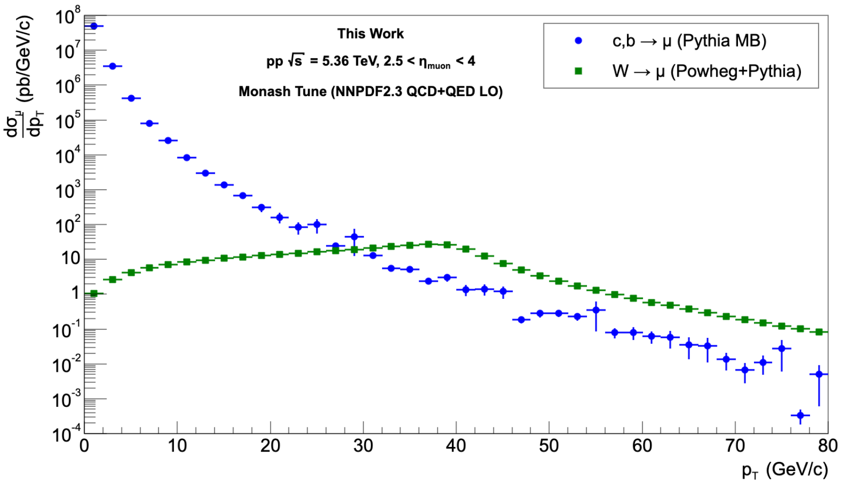

Figure 31: The p_T-differential cross-sections of $W^{\pm} \rightarrow \mu^{\pm}+\overset{(-)}{\nu}_{\mu}$ and HF$\rightarrow \mu$ in the forward region of proton-proton collisions at $\sqrt{s} = 5.36$ TeV with POWHEG and Pythia.

4.3.2 Charge Asymmetry

As already mentioned, POWHEG generates $W^+ \rightarrow \mu^+$ and $W^- \rightarrow \mu^-$ events separately. In this section, the physical importance of the differences between these two oppositely charged contributions to the $W^{\pm} \rightarrow \mu^{\pm}+\overset{(-)}{\nu}_{\mu}$ process will be briefly investigated. It might be initially expected from symmetry that these parts will have equal and matching cross-sections, and for the resulting μ^+ and μ^- decays to be produced in equal amounts. In Figure 32, it can be seen that this is not the case. There is a charge asymmetry that arises between the production of the two oppositely charged contributions to the $W^{\pm} \rightarrow \mu^{\pm}+\overset{(-)}{\nu}_{\mu}$ cross-section. There are two observed aspects to the charge asymmetry, where the first is an angular asymmetry of the distributions as a function of rapidity. This angular asymmetry can be attributed to the V-A form of the weak interaction for the $\mu - W$ coupling [46] - as introduced in section 1.2.6. The second asymmetry is with respect to the total production of μ^+ and μ^- from $W^{\pm}$ boson decays. When integrating the full distributions in Figure 32, it is obtained that $\sigma(W^+)/\sigma(W^-) \approx 1.56$. This asymmetry in the $\mu^{\pm}$ production will be the focus in this section.

In Figure 33, the respective $W^{\pm}$ boson cross-sections are considered as a function of p_T - where only muons in the forward region are being considered (as indicated by the dashed red lines in Figure 32). When integrating over the distributions in this case, it is obtained that $\sigma(W^+)/\sigma(W^-) \approx 0.89$. To understand why this production asymmetry arises, it is necessary to refer back to the PDFs of the colliding protons - as presented in section 2.2.2. It was mentioned in section 1.2.6 that the the leading order production of $W^{\pm}$ bosons in relativistic proton-proton collisions is given by the $u\bar{d} \rightarrow W^+$ and $d\bar{u} \rightarrow W^-$ processes. In Figure 22 on the right, it can be seen that the $\bar{d}(x)$ and $\bar{u}(x)$ quark probability distributions in the proton at relativistic energies are roughly equivalent. The same does not hold for the the valence quark distributions - $u(x)$ and $d(x)$. Thus, the asymmetry that arises in the production of W^+ and W^- bosons can be attributed to the difference in these PDFs of the proton at relativistic energies. This enforces the motivation that measuring the oppositely charged contributions of the $W^{\pm} \rightarrow \mu^{\pm}+\overset{(-)}{\nu}_{\mu}$ process can be meaningfully used to probe the valence PDFs of the proton - specifically at small Bjorken-x in the case of the forward region, as shown by equation 15.

4.3.3 Multiplicity Dependence

In section 1.2.6, it was argued that it is meaningful to investigate the primary charged-particle multiplicity (referred to as just 'multiplicity' from this point) dependence of the $W^{\pm}$ boson production, as this observable is expected to be sensitive to initial-state effects of proton-proton collisions. In this section, the normalised

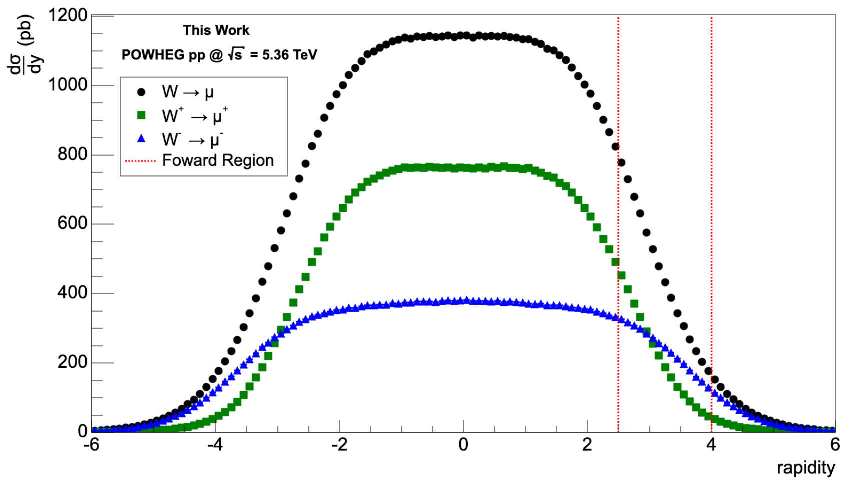

Figure 32: The rapidity dependence of muons from $W^{\pm}$ decays in proton-proton collisions at $\sqrt{s} = 5.36$ TeV, using POWHEG - also showing the angular charge asymmetry between the $W^+ \to \mu^+$ and $W^- \to \mu^-$ contributions.

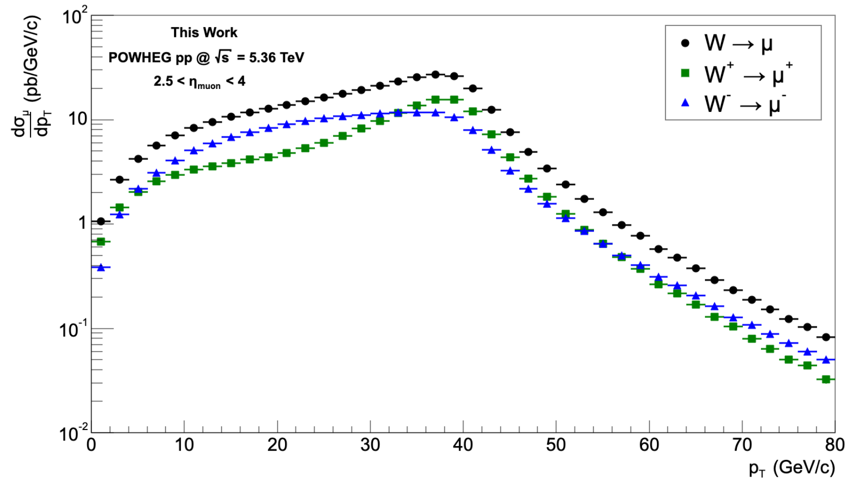

Figure 33: The p_T-differential cross-section of muon from $W^{\pm}$ decays in the forward rapidity region, showing the charge asymmetry between the $W^+ \to \mu^+$ and $W^- \to \mu^-$ contributions.

multiplicity dependence of the self-normalised $W^{\pm}$ boson production observable will be concretely defined. It will then be investigated in the coming sections which models of the proton-proton collision this observable is sensitive to. In this section, the multiplicity will be estimated in the central region specifically (as presented for minimum-bias in Figure 26), where the choice of this region will be motivated in section 4.3.4. As mentioned before, the muon production from $W^{\pm}$ boson decays will be considered in the forward rapidity region - where the additional cut of $30.0 < p_T < 60.0$ will also be applied. The lower p_T-limit was motivated in section 4.3.1, where the upper p_T-limit is added to agree with the experimental constraints followed in [29] - where the p_T value of the muon is taken from the Pythia event record after the matching.

After matching POWHEG+Pythia to generate the full collision event, the multiplicity dependence of the stand-alone generated $W^{\pm} \to \mu^{\pm} + \overset{(-)}{\nu}_{\mu}$ events is obtained and presented in Figure 34 - in comparison to the already obtain multiplicity dependence of minimum-bias events. As expected, the cross-section of

$W^{\pm} \to \mu^{\pm}+\overset{(-)}{\nu}_{\mu}$ events is much lower than minimum-bias events, since the production of muons from $W^{\pm}$ decays is a rare process. What is more interesting to observe is the difference in the shapes of these distributions - in terms of how the production scales as a function of the event multiplicity. To investigate this further, the ratio between the minimum-bias and stand-alone $W^{\pm} \to \mu^{\pm}+\overset{(-)}{\nu}_{\mu}$ multiplicity distributions is considered - which is shown in Figure 35. For this figure, the multiplicity axis has already been scaled to rather represent the multiplicity per unit of η - where different binning has also been applied to avoid large statistical uncertainties later in the analysis. A positively sloped linear trend is observed for the ratio, indicating that the multiplicity dependence of minimum-bias events drops off faster (in a linear manner) than the $W^{\pm} \to \mu^{\pm}+\overset{(-)}{\nu}_{\mu}$ events. Put differently, $W^{\pm} \to \mu^{\pm}+\overset{(-)}{\nu}_{\mu}$ events become more likely at higher multiplicities w.r.t minimum-bias. It will soon be shown that the linear shape of the ratio carries a physical significance, which can be used to investigate the modelling of the initial state of the collision.

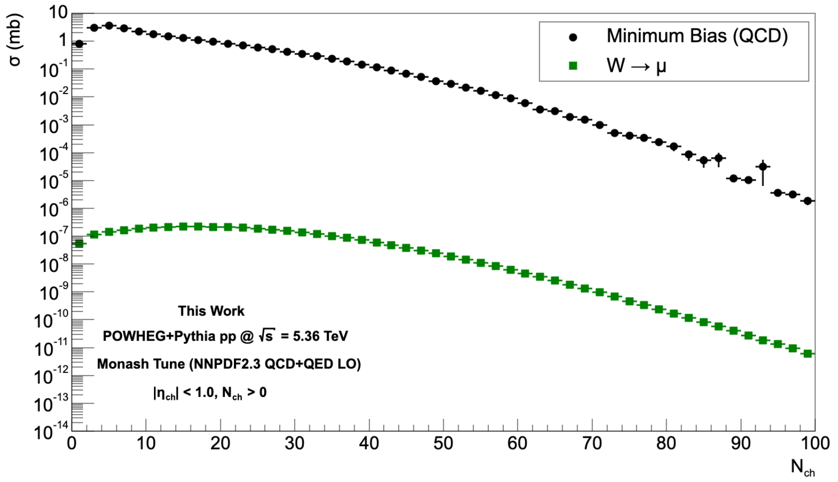

Figure 34: The multiplicity distributions of minimum-bias and $W^{\pm} \to \mu^{\pm}+\overset{(-)}{\nu}_{\mu}$ events in proton-proton collisions, at $\sqrt{s} = 5.36$ TeV using POWHEG and Pythia.

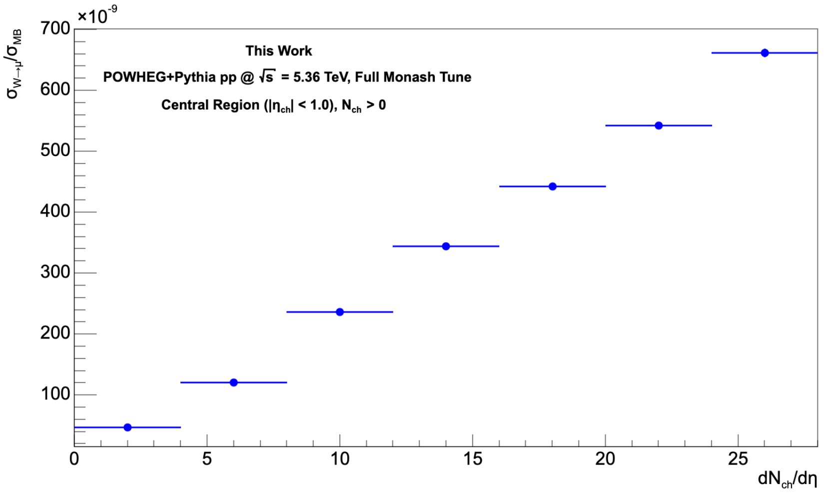

Figure 35: Ratio between the multiplicity distributions of generated $W^{\pm} \to \mu^{\pm}+\overset{(-)}{\nu}_{\mu}$ and minimum-bias events, in the relevant multiplicity bins.

It is important to consider that the multiplicity dependent yield of stand-alone generated $W^{\pm} \rightarrow \mu^{\pm} + \overset{(-)}{\nu}_{\mu}$ events is not enough by itself. As shown by the multiplicity distribution of minimum-bias events, not an equal weighting is given to each multiplicity bin. When generating stand-alone $W^{\pm} \rightarrow \mu^{\pm} + \overset{(-)}{\nu}_{\mu}$ events, the multiplicity scaling of events in the context of fully inclusive minimum-bias is not accounted for. Thus, to obtain an experimentally accurate multiplicity dependent yield of muons from $W^{\pm}$ boson decays in minimum-bias events, it is necessary to scale the obtained stand-alone $W^{\pm} \rightarrow \mu^{\pm} + \overset{(-)}{\nu}_{\mu}$ multiplicity distribution by the obtained ratio presented in Figure 35. From this, the more "realistic" multiplicity dependent scaling of muon production from $W^{\pm}$ boson decays in minimum-bias events can be obtained - as shown in Figure 36. In this case, the area of the distribution is also normalised to unity, so either considering the yield (N_{events}) or the cross-section will give the same result. The multiplicity axis has also been further scaled by the obtained average of the minimum-bias multiplicity distribution, as presented in Table 3. Thus, the production is considered as a function of the normalised multiplicity $(dN_{ch}/d\eta)/<dN_{ch}/d\eta>$ from this point onward.

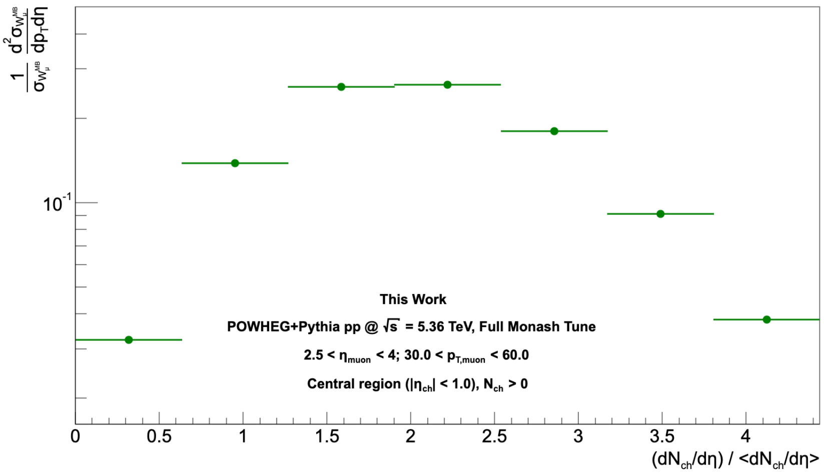

Figure 36: The minimum-bias scaled muon production from $W^{\pm}$ boson decays in the forward region as a function of the self-normalised multiplicity, in proton-proton collisions at $\sqrt{s} = 5.36$ TeV using POWHEG+Pythia.

The next step is to obtain the average of the muon production from $W^{\pm}$ boson decays, per multiplicity bin. For this, the muon production from $W^{\pm}$ boson decays in the forward region, in each multiplicity bin, is considered as a function of the muon p_t - as shown in Figure 37. These distributions are then additionally normalised by the full $W^{\pm} \rightarrow \mu^{\pm} + \overset{(-)}{\nu}_{\mu}$ cross-section in the forward region. From this, the p_T-bin entries for each multiplicity bin can be used as input to a profile histogram - in order to obtained an average for the forward muon production from $W^{\pm}$ boson decays $< d\sigma^2/d\eta dp_T >$ in each multiplicity bin. In Figure 37, it also becomes clear that the available statistics leads to an upper-limit of the multiplicity that can be considered. When considering bins at larger multiplicities, the statistics will reduce and lead to larger statistical uncertainties - which gets amplified by the fact that a weighted average is being considered for each bin. The multiplicity bins have also been considered to have equal width for simplicity. Choosing different multiplicity bins should produce the same result, as the obtained profile histogram of the average production is properly normalised by the multiplicity-bin widths.

Now it is possible to divide the minimum-bias scaled production of muons from $W^{\pm}$ boson decays in the forward region (given in Figure 36), by the average of the production per multiplicity-bin (obtained from Figure 37) - including all the discussed normalisations. This yields the desired observable of the self-normalised production of muons from $W^{\pm}$ boson decays in the forward region as a function of the normalised multiplicity. The obtained result is given in Figure 38, where the multiplicity is estimated in the central region and the full Monash 2013 Tune is used - this will be relevant in the coming sections. It is seen that

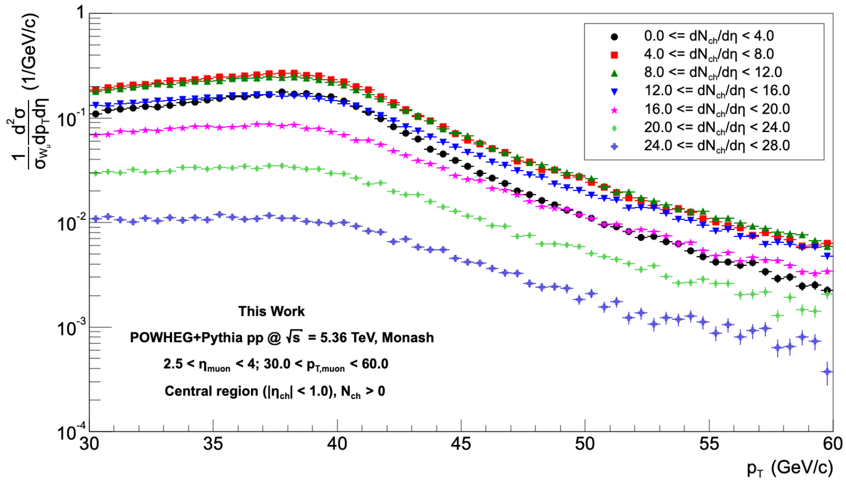

Figure 37: The p_T-differential cross-section of muons from $W^\pm$ boson decays in the forward region, split into the different multiplicity bins and normalised by the total $W^\pm \to \mu^\pm + \overset{(-)}{\nu_\mu}$ cross-section.

the same linear trend is obtained as for Figure 35, but the gradient is now normalised to be unity - shown by the linear weighted best fit. The values of the best-fit parameters for all the presented distributions in this section are given in Table 4. This is the key observable that is aimed at to be defined and investigate in this work. It was mentioned that the ratio in Figure 35 already carries significance, which becomes more clear now. It seems that the trend of interest is already determined by the ratio of the stand-alone generated $W^\pm \to \mu^\pm + \overset{(-)}{\nu_\mu}$ events and the minimum-bias events in each multiplicity-bin under consideration - the rest of the steps that follow are merely normalisations to scale each axis by the averages to obtain a gradient of unity (in the linear case). The obtained result can also be compared to the ALICE result given in Figure 10. In both cases a positively sloped linear trend is obtained, with the key different being in the slope of the linear trend - in the case of the ALICE result, the slope is slightly greater than unity.

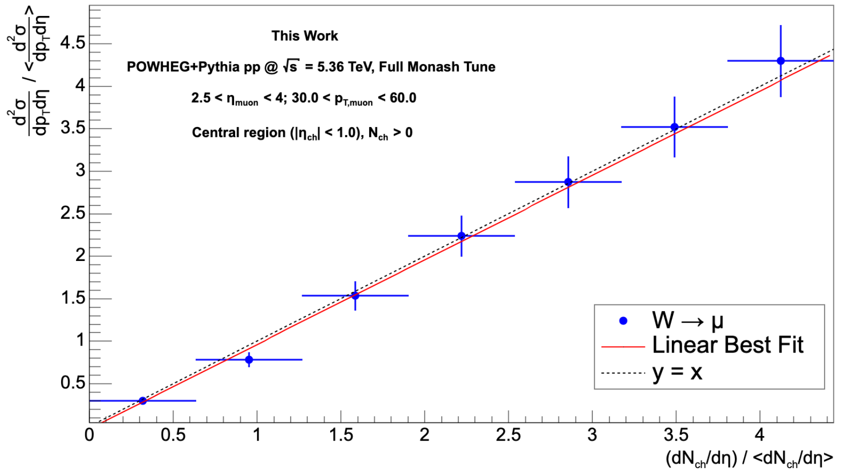

Figure 38: The self-normalised multiplicity dependence (estimated in the **central** region) of the self-normalised production of muons from $W^\pm$ boson decays, in the forward region of proton-proton collisions at $\sqrt{s} = 5.36$ TeV using POWHEG+Pythia.

The obtained linear trend can be understood from the fact that the $W^{\pm}$ boson of interest is always produced in the hardest partonic scattering of the collision, and that the full $W^{\pm} \rightarrow \mu^{\pm} + \overset{(-)}{\nu}_{\mu}$ process does not interact strongly. A stronger than linear increase would indicate that the process of interest is dominated by the hard interaction scale, as the production would increase faster than the average at higher multiplicities - since it was shown that the multiplicity scales with the number of MPI in Figure 9. Conversely, a weaker than linear trend would indicate that the production of the process is dominated by the soft scales, as the production would be "suppressed" at higher multiplicities - due to the increased number of colour charges present that will interact at the soft scale. As the muon production from $W^{\pm}$ boson decays isn't dominated by either of the scales, it isn't sensitive to the evolution between the two scales and a linear trend is obtained. This enforces that it can serve as a meaningful baseline measurement to perform when also considering the normalised multiplicity dependence observable for other processes in proton-proton collisions - in order to isolate initial-state effects.

4.3.4 Auto Correlations

Before investigating the model effects on the normalised multiplicity dependence of the self-normalised production of muons from $W^{\pm}$ boson decays observable, it is first necessary to motivate the choice of specifically estimating the charged-particle multiplicity in the central region. As was shown in Figure 26 and discussed in section 1.3.2, it is possible to estimate the multiplicity in two different η-regions experimentally - namely in the central region of the ITS and forward region of the V0C. In Figure 38, it was shown that a linear trend with gradient of unity is obtained for the observable of interest when estimating the multiplicity in the central region. In Figure 39, it shows the result obtained when following the exact same procedure as outlined in the previous section, but changing the multiplicity to be estimated in the forward region of the V0C detector. It is seen that a fully linear trend is no longer obtained, where the trend starts to slightly drop-off towards larger multiplicity bins - which can also be seen from the best-fit line having a slope of slightly less than unity. The key aspect that has changed, which leads to this deviation from linearity, is that the multiplicity estimation region and the decay muon production measurement region now have an overlap in η. To investigate this phenomenon further, an impractical case will be considered of estimating the multiplicity in the exact same region as the decay muon production - so that there is a full overlap in η.

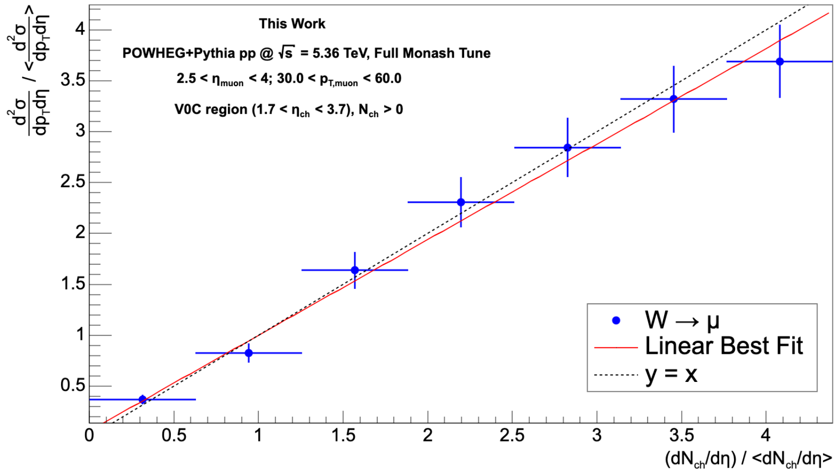

Figure 39: The self-normalised multiplicity dependence (estimated in the ALICE **V0C** region) of the self-normalised production of muons from $W^{\pm}$ boson decays in the forward region of proton-proton collisions, at $\sqrt{s} = 5.36$ TeV using POWHEG+Pythia.

In Figure 40, it shows the result obtained for the normalise multiplicity observable when estimating the multiplicity in the exact same region as the decay muon production. It is seen that a similar deviation from linearity is obtained as in Figure 39, but the effects are more pronounced with the trend dropping off faster - in this case it is visually not meaningful to perform a linear fit any more. There also appears to be a slight increase in the trend at the low to central multiplicity-bins, before the drop-off then takes over at the higher multiplicity-bins. This observed phenomenon is known as an auto-correlation, which arises from the fact that the decay muon production and multiplicity are being estimated in the same region. In the lower multiplicity-bins, the slight increase in the slope can be attributed to the fact that the charged muon from the $W^{\pm}$ boson decay will always contribute to the multiplicity and slightly bias it to a larger value - which will "shift" these events to a larger multiplicity-bin. In the higher multiplicity bins, the bias from a single charged muon becomes negligible and the faster than linear trend starts to drop-off and have a less than linear slope. To understand this drop-off, it is necessary to think about the phase space of available energy in the collisions - which produces a massive $W^{\pm}$ boson. A large chunk of the available momentum and energy in the forward η-region of the collision will be taken up by the production of the massive $W^{\pm}$ boson, and then carried by the muon and neutrino after the decay. Thus, there will be less of the phase space available in this region of the collision to produce showers of additional charged particles. From this, it is clear that estimating the multiplicity in the central barrel region of the ALICE ITS is the correct choice - in order to avoid the observed auto-correlation effects.

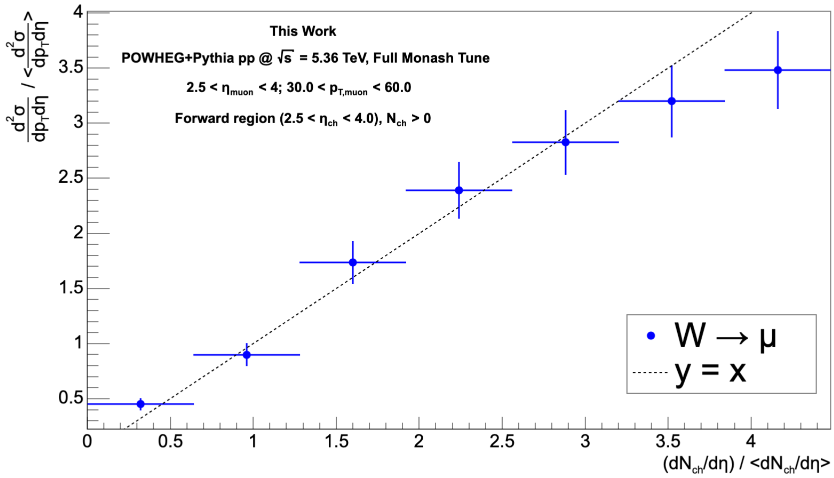

Figure 40: The self-normalised multiplicity dependence (estimated in the **Muon Spectrometer** region) of the self-normalised production of muons from $W^{\pm}$ boson decays in the forward region of proton-proton collisions, at $\sqrt{s} = 5.36$ TeV using POWHEG+Pythia.

4.3.5 Model Effects

In order to investigate and understand how the normalised multiplicity observable (defined in section 4.3.3) is sensitive to initial state of the proton-proton collision, it is meaningful to investigate the effects on the observable by varying these models. In this section, the focus will be specifically on the MPI and CR models; where the effects of individually turning off these models will be investigated - as already done for the minimum-bias multiplicity distribution in Figure 27. In the case of CR, it has been hypothesized that a variation in this model is expected to have no effect - as the $W^{\pm} \rightarrow \mu^{\pm} + \overset{(-)}{\nu}_{\mu}$ process does not interact strongly and the production should remain unaffected. In Figure 41, it shows the obtained result for the normalised multiplicity dependence of the self-normalised muon production from $W^{\pm}$ boson decays when using the Monash Tune with CR switched off - with the multiplicity estimated in the central region as motivated in the previous section. It is seen that there is a similar drop-off at the higher multiplicity-bins - as was observed in the case of auto-correlations. This deviation from linearity when turning off CR is not as hypothesized, so the source of this effect is unknown. A possible explanation can be explored by the fact that the CR model used in the Monash Tune is the MPI-based model - as mentioned in section 2.2.6. Even though the $W^{\pm} \to \mu^{\pm} + \overset{(-)}{\nu}_{\mu}$ process does not interact strongly, it is produced in the partonic scatterings - which CR has a connection to in the MPI-based model. In order to investigate this further, the case of using a different CR model instead of fully turning it off can be considered - namely the gluon-move model.

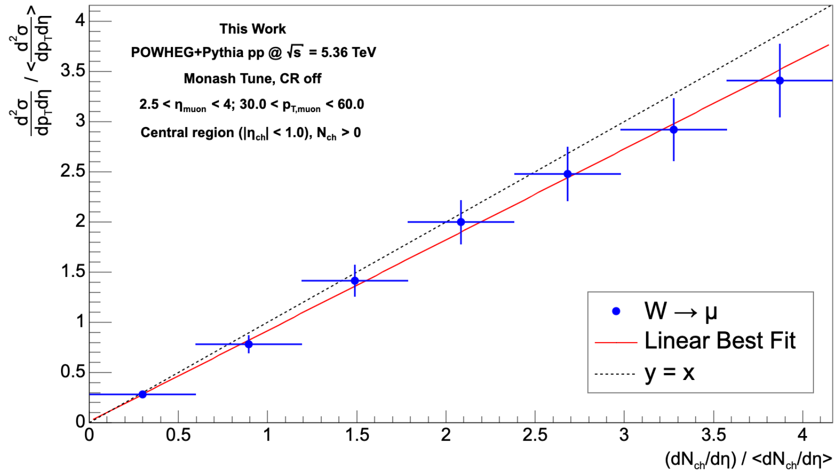

Figure 41: The self-normalised multiplicity dependence (estimated in the **central** region) of the self-normalised production of muons from $W^{\pm}$ boson decays in the forward region of proton-proton collisions, at $\sqrt{s} = 5.36$ TeV using POWHEG+Pythia - with the Monash Tune and **Colour Reconnections** turned off.

In Figure 42, it shows the result for the normalised multiplicity observable when using the Monash tune with the gluon-move model for CR (as introduced in section 2.2.6) - instead of the default MPI-based model. It can be seen that the drop-off in the trend is slightly less when using the gluon-move model, compared to the case of turning off CR completely. This indicates that changing the CR model can lead to a deviation from linearity, even though it is not significant and the slope only becomes slightly less than unity. At this point, it is important to mention that it is not always valid to keep the same tune when changing model parameters. In the same way that it is necessary to use a different tune when changing the PDF, it might also be necessary to adjust the tuning when changing the CR or MPI models - which could serve as an alternative explanation for the deviation from linearity. Despite the effect of the full tune not being fully understood, it is still meaningful to investigate the potential effects of adjusting the model parameters of the tune.

In contrast to the CR model, it is expected that turning off the MPI model will lead to an observable effect in the slope of the normalised multiplicity dependence of the muon production from $W^{\pm}$ boson decays - as the $W^{\pm}$ boson is produced in the hard partonic scattering. In Figure 43, it is seen that this expectation is verified, where a large deviation from linearity (stronger than linear increase) is observed when turning off the MPI model. This agrees with the previous interpretation that processes dominated by the hard scale will show a faster than linear increase. When MPI is switched off and there is only a singular partonic interaction, this will lead to the $W^{\pm}$ boson production being biased by the hard scale and result in a faster than linear increase. This again illustrates why the self-normalised muon production from $W^{\pm}$ boson decays as a function of the normalised multiplicity can serve as a meaningful baseline measurement in proton-proton collisions. A strictly linear trend with a slope of unity can be interpreted as depicting a "balance" between the MPI and CR models on the $W^{\pm}$ boson and multiplicity production - to produce the observed scaling of the produced charged particles in an event. This observable will be maximally sensitive to the initial-state MPI model, and can thus be used to obtain information about the scaling of MPIs in relativistic proton-proton collisions.

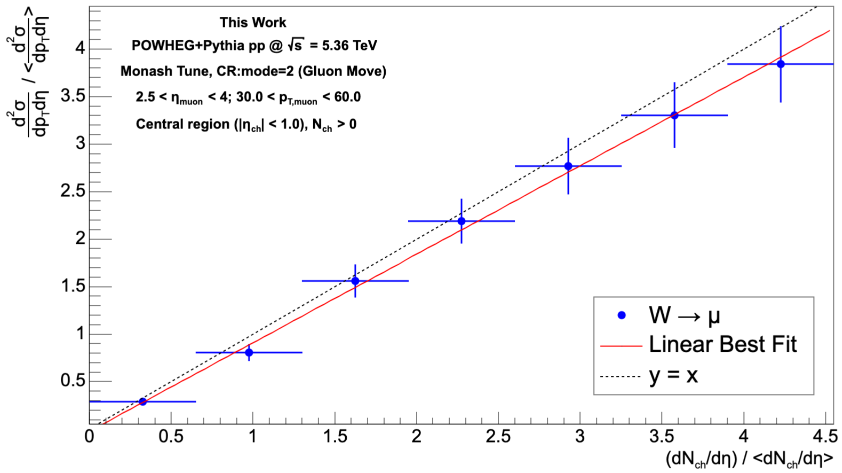

Figure 42: The self-normalised multiplicity dependence (estimated in the **central** region) of the self-normalised production of muons from $W^{\pm}$ boson decays in the forward region of proton-proton collisions, at $\sqrt{s} = 5.36$ TeV using POWHEG+Pythia - with the Monash Tune and **Colour Reconnections** set to the **gluon-move** model.

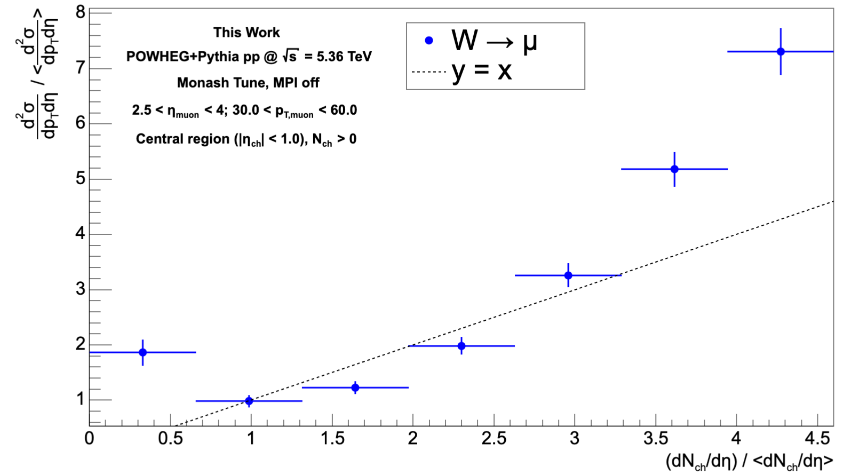

Figure 43: The self-normalised multiplicity dependence (estimated in the **central** region) of the self-normalised production of muons from $W^{\pm}$ boson decays in the forward region of proton-proton collisions, at $\sqrt{s} = 5.36$ TeV using POWHEG+Pythia - with the Monash Tune and **Multi-Parton Interactions** turned off.

In Table 4, the linear best-fit parameters for all the considered cases of the normalised multiplicity dependence of the muon production from $W^{\pm}$ decays in the forward region in this section are presented - also including the cases where it was argued that a linear fit is no longer fully valid. It is seen that the slope obtained for the observable of interest can noticeably vary when adjusting the initial-state model parameters - specifically MPI and CR. It is important to point out that the auto-correlation effects can be ambiguously mistaken for model effects that arise from CR. Thus, it is necessary to estimate the multiplicity and decay muon production in different η-regions to avoid this ambiguity in the results. Without auto-correlations present, the self-normalised multiplicity dependence of the muon production from $W^{\pm}$ boson decays can be meaningfully used as an experimental observable to study initial-state effects in relativistic proton-proton

Table 4: Linear best-fit parameters for the normalised multiplicity dependence of the self-normalised muon production from $W^{\pm}$ boson decays results.

Tune	N_{ch} Region	Gradient (m)	Intercept (c)
Full Monash Tune	Central (ITS)	0.99 ± 0.05	-0.03 ± 0.04
Full Monash Tune	Forward (Muon Arm)	0.88 ± 0.05	0.16 ± 0.06
Full Monash Tune	Forward (V0C)	0.94 ± 0.05	0.06 ± 0.05
Monash Tune (CR:mode=2)	Central (ITS)	0.93 ± 0.05	-0.02 ± 0.04
Monash Tune (CR off)	Central (ITS)	0.91 ± 0.05	0.01 ± 0.04
Monash Tune (MPI off)	Central (ITS)	1.19 ± 0.07	-0.23 ± 0.14

collisions - while serving as a reference measurement for other collision systems.

4.4 Outlook for Data Analysis

As mentioned in section 1.1.3, one of the aims of this work is also to serve as a feasibility study to perform the same analysis with ALICE Run 3 data. For this very reason, aspects of the ALICE detector have already been incorporated into the analysis - such as considering the ALICE definition of the primary charged-particle multiplicity and considering only the viable η-regions of the ALICE detectors. Before it is possible to obtain a realistic estimate of the statistics that will be available from the ALICE Run 3 proton-proton reference data, it is first necessary to look into some of the relevant detector effects - which will bias how many events are observed.

It is important to mention that no uncertainties will be presented for the results in this section. The available statistics are limited and will only serve as a very rough estimate. The main goal is to have a first glance at the feasibility of performing the study with data. For a more rigorous approach, such as determining the acceptance/efficiency of the detector as a function of η and p_T, much more statistics will be required.

4.4.1 Detector Effects

In the analysis up until now, only “pure” simulations of proton-proton collisions have been considered. In order to achieve a more realistic experimental picture of what can be measured to what extent, it is necessary to briefly look into the contributing detector effects. In the context of measuring the $W^{\pm} \to \mu^{\pm} + \overset{(-)}{\nu}_{\mu}$ process, the muon spectrometer in the forward η-region of ALICE will be used. As already mentioned, it is only possible to measure the decay muon, since the produced $W^{\pm}$ boson is too short-lived. In order to incorporate the relevant detector effects into the simulation, it is necessary to make use of the O2 simulation software (O2sim) as introduced in section 3.3.1 - where the detector geometries are defined and GEANT4 is used to simulate the transport of the particles through the detectors. The same stand-alone $W^{\pm} \to \mu^{\pm} + \overset{(-)}{\nu}_{\mu}$ events (generated with POWHEG) used for the analysis in section 4.3.3 can be used as input to O2sim - which will then simulate the resulting detector response. Since simulating the transport of particles through the detector is extremely computationally expensive, a software trigger is also implemented to only select events where a muon from $W^{\pm}$ boson decay is produced specifically in the relevant forward η-region. Despite the additional software trigger, it was still only possible to simulate 100 events for each $W^{+} \to \mu^{+}$ and $W^{-} \to \mu^{-}$ in this work - which can still function as a meaningful test sample.

In Figure 44, it shows the side-by-side comparison of the two-dimensional η and p_T distributions of the pure simulated muon tracks (left), and measured information from the detector reconstructed tracks (right). It is clear that not all the muons originating from the $W^{\pm}$ boson decays are successfully reconstructed by the muon detector. This is known as the reconstruction efficiency of the detector, which is crucial to take into account when aiming for a realistic comparison between theoretical simulations and experimental data. For

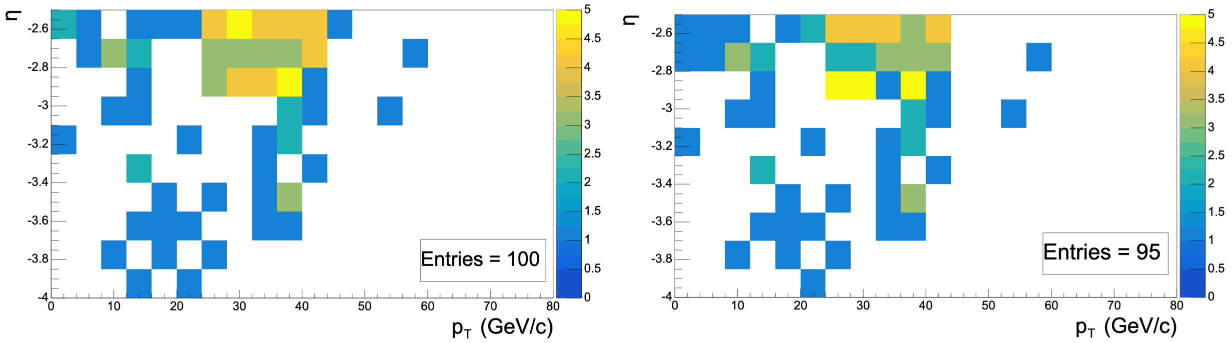

(a) Pure simulated muons.

(b) Reconstructed muon tracks.

Figure 44: The p_T and η distribution of muons decaying from W^+ bosons, showing the difference between the true simulated and detector reconstructed tracks - using ALICE 0^2 simulations.

example, the experimentally measured cross-section needs to be divided by the determined detector efficiency - in order to account for the measurement inaccuracy. In this work, the estimation of statistics presented in the next section needs to be scaled by the efficiency - in order to obtain a more realistic estimate of how many tracks the detector will physically measure. Ideally, the efficiency can be accurately obtained as a function of η and p_T and then be used to scale the obtained two-dimensional distributions. Due to the limit statistics, this will not be possible in this work. Alternatively, the efficiency will be taken as a conservative constant value of 95% - which is motivated from the results in Figure 44. In reality, the efficiency will most likely be lower, especially since the purity of the signal is not being taken into account - which will not be considered in this work.

Another aspect that needs to be considered, is how accurately the detector measures the kinematic values of the tracks which are successfully reconstructed. In Figure 45, it shows the transverse-momentum resolution of the reconstructed muon tracks - from both W^+ (left) and W^- (right) boson decays. The momentum resolution is simply determined by considering the absolute different between the p_T of the simulated and reconstructed muon track. It is seen that the detector does not measure the p_T of the track precisely accurately, since there is a non-negligible width for the resolution distribution. There are also a few tracks with large differences at the tail of the distribution. This can be attributed to the fact that some of the muons will undergo coulomb scatterings in the absorber, and also potentially emit photons along the way. This results in a loss of momentum from the point where the muon is produced in the decay, to the point where it is measured and reconstructed by the detector. The momentum resolution of the detector will be an important factor to consider when conducting the experimental analysis, as it has been shown in section 4.3.3 that the p_T of the muon tracks play a role in the multiplicity analysis of interest. If the momentum resolution is too large, this can contribute to large uncertainties in the analysis results.

4.4.2 Statistics Estimate

Now, all of the pieces are in place to obtain an approximated estimate of the available statistics for the $W^{\pm} \rightarrow \mu^{\pm} + \overset{(-)}{\nu}_{\mu}$ process from the ALICE Run 3 proton-proton reference data at $\sqrt{s} = 5.36$ TeV. The theoretical cross-section for muons from $W^{\pm}$ boson decays in the forward region (presented in Figure 33) can be combined with the experimental integrated luminosity (presented in Figure 1), and equation 2 to obtained an expected number of events. The conservative estimate for the detector efficiency of 95%, as motivated in the previous section, will also be used to scale the obtained number of events. The resulting estimate of statistics for muons from $W^{\pm}$ boson decay, in the forward region of ALICE Run 3 proton-proton reference data, is given in Figure 46. The estimate is considered as a function of p_T, as it has been made clear in section 4.3.3 that p_T cuts will be performed, and it is additionally necessary to consider the yield as a function of p_T for each multiplicity bin to determine the average - as shown in Figure 37.

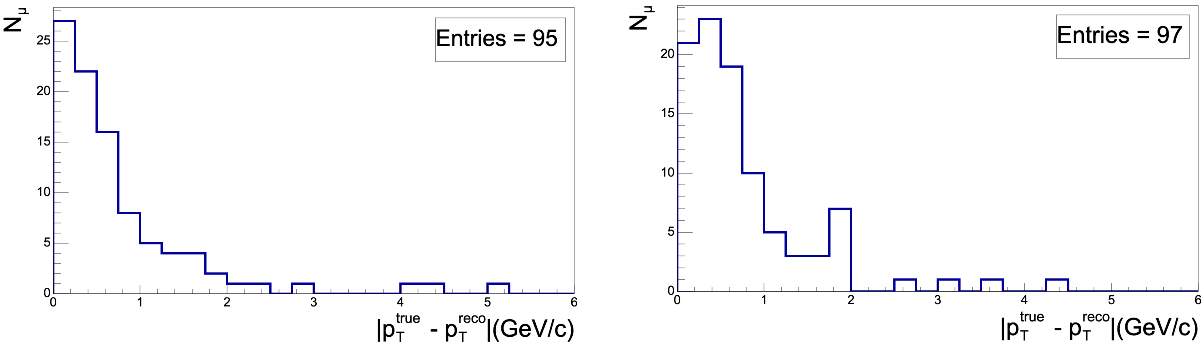

(a) Muons from W^+ boson decays.

(b) Muons from W^- boson decays.

Figure 45: The transverse-momentum resolution $|p_T^{true} - p_T^{reco}|$ of simulated muon tracks from $W^{\pm}$ boson decays, reconstructed in the ALICE Muon Spectrometer using 0^2 simulations.

From this, it can be obtained that the estimated number of events in the region of $30.0 < p_T < 60.0$ GeV/c is on the order of 10^3. Considering that the statistics for muons from $W^{\pm}$ boson decays used in section 4.3.3 for the multiplicity analysis was on the order of 10^5, the estimate does not seem encouraging at a first glance. Further dividing the events into multiplicity bins will lead to even larger statistical uncertainties. The statistics restriction is primarily due to the small amount of data that is collected for proton-proton reference collisions in ALICE, considering that the data collected for lead-lead collisions in Run 3 so far is on the order of 10^3 times more - not taking into account that the $W^{\pm} \to \mu^{\pm} + \overset{(-)}{\nu}_{\mu}$ cross-section will be different in this case. Even though it has been shown that the analysis in reference proton-proton collisions can serve as a meaningful baseline measurement for other collision systems, it might be more realistic to first perform the multiplicity analysis with proton-lead or lead-lead data - due to the currently available statistics. Thus, a similar feasibility study in the other collision systems can be a meaningful next step to motivate doing the multiplicity analysis with ALICE Run 3 data. Even though the multiplicity analysis might not seem feasible with reference proton-proton data, it can still be meaningful to measure just the $W^{\pm} \to \mu^{\pm} + \overset{(-)}{\nu}_{\mu}$ cross-section - which can be directly compared to the same cross-sections obtained from the other collision systems.

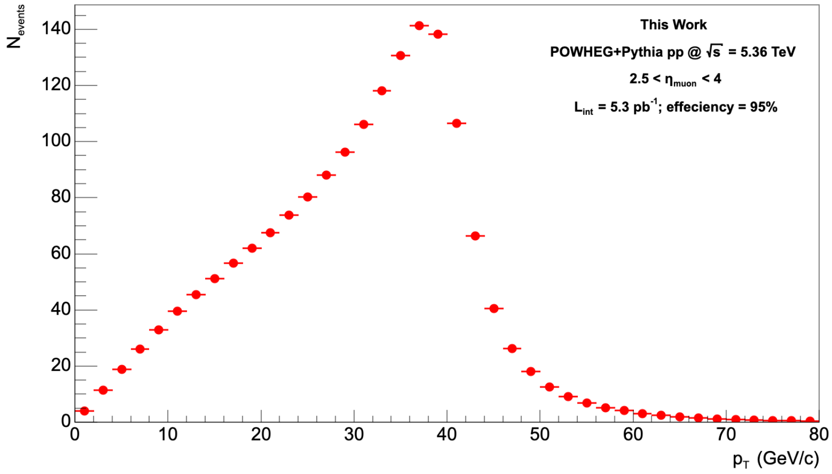

Figure 46: Estimate of the available statistics for muons from $W^{\pm}$ boson decays in the forward rapidity region, in the ALICE Run 3 proton-proton reference data at $\sqrt{s} = 5.36$ TeV.

5 Conclusion and Outlook

The primary aim of this work was to investigate the muon production from $W^{\pm}$ boson decays in simulated relativistic proton-proton collisions, at $\sqrt{s} = 5.36$ TeV - as laid out in section 1.1. Throughout sections 1.2 and 2.2, it was theoretically motivated that the $W^{\pm} \to \mu^{\pm} + \overset{(-)}{\nu}_{\mu}$ perturbative process can serve as a meaningful probe to study the initial state of the collision - as it is always produced in the hard partonic scattering and carries no colour charge. In section 2.2 specifically, a closer look was given at the implementation and influence of the PDF, MPI and CR models on the initial-state of the collision - where it was argued that the muon production from $W^{\pm}$ boson decays should be sensitive to these models. The primary charged-particle multiplicity, which was shown to be dominated by non-perturbative processes, was also introduced as an observable of interest - where it was shown how it is sensitive to the MPI and CR models. It was then motivated that it is meaningful to study the multiplicity dependence of the muon production from $W^{\pm}$ boson decays, which can serve as a baseline measurement in proton-proton collisions to isolate the initial-state effects - which can be used as a reference for other collision systems such as proton-lead and lead-lead.

In section 1.3, ALICE was introduced as the reference experiment of interest - where the key physics motivations of the experiment and relevant results were briefly introduced. In section 1.1.3, it was motivated that the simulation study in this work will also serve as a feasibility study for the same measurement to be done with the ALICE Run 3 proton-proton reference data. Throughout the presented analysis, aspects of the ALICE detector were incorporated into the simulation - such as considering the ALICE definition of the primary charged-particle multiplicity. The ALICE Muon Spectrometer was also introduced as the detector of interest to measure the muon production from $W^{\pm}$ boson decays, where the forward η-region of this detector was also incorporated into the analysis. It was additionally argued that considering the production in this forward region would carry a physical significance, where it was shown in equation 15 that it would correspond to the small Bjorken-x region of the PDF set. The detectors that are used in ALICE to experimentally estimate the charge-particle multiplicity were also introduced, where it was shown in Figure 26 that the multiplicity can be estimated in either the central or forward rapidity regions.

After introducing the core software and configurations that were used to generate and analyse the relevant simulations in section 3, the results were then presented in section 4. To set up the simulation results, it was shown in section 4.2.1 how the total minimum-bias cross-section can be generated in Pythia - where the focus was on showing how the non-perturbative (soft-QCD) and perturbative (hard-QCD) regimes contribute. With this in hand, the minimum-bias multiplicity distribution was determined and presented in section 4.2.2 - where it was shown how the distribution is effected by the chosen estimation region and the altering of the MPI/CR models. In section 4.2.3, it was then shown how the $HF \to \mu$ cross-section can be obtained from the Pythia minimum-bias events. It was additionally shown how different Pythia tunes will bias the obtained $HF \to \mu$ cross-section, which can not be neglected when considering the inclusive simulation systematic uncertainties. The $HF \to \mu$ cross-section obtained with the Monash Tune was then compared to the ALICE experimental data result from Run 2 in Figure 29, which provided a level of confidence that the obtained simulation result is reasonable - only overestimating the data by a factor of roughly 1.5-2. Using this, it was then argued in section 4.3.1 that the $HF \to \mu$ processes serves as the dominant and non-negligible background for the production of muon from $W^{\pm}$ boson decays in the forward region of proton-proton collisions.

In section 4.3.2, the separate contributions of the $W^{+} \to \mu^{+}$ and $W^{-} \to \mu^{-}$ processes to the $W \to \mu$ production was investigated. From these results, it was argued that the arising asymmetry between the two charge contributions can be used to study the ratio between the up and down quark PDF distributions - with a focus on the small Bjorken-x regime in the forward region. Using the inclusive $W \to \mu$ production in the forward region, the multiplicity dependence was then investigated in section 4.3.3. Throughout this section, it was shown how the normalised multiplicity dependence of the self-normalised $W \to \mu$ production observable is defined and computed. The obtained result, when using the full Monash Tune and estimating the multiplicity in the central region, was presented in Figure 38. It was argued that the obtained linear slope, which agrees with the ALICE result of the same observable for $W \to e$ in the central region, can be expected from the fact that the $W^{\pm} \to \mu^{\pm} + \overset{(-)}{\nu}_{\mu}$ processes carries no colour charge. It was explained in section 2.2.6 that the MPI-based model is used in the default Monash Tune for CR, where the partons from the hard scattering are reconnected first. Thus, since the $W^{\pm}$ boson is produced in the hard scattering and not effected by CR, it's production can be expected to scale linearly with the multiplicity - as motivated by Figure 9. To motivate the choice of the central region to estimate the multiplicity, it was shown in section 4.3.4 that auto-correlation effects can arise when estimating the multiplicity and decay muon production in the same η-region - which influences the result by changing the linear slope. In section 4.3.5, it was then shown how turning off MPI and CR separately would also change the obtained trend and slope of the multiplicity observable - which enforced the initial motivation that the observable would be sensitive to the models of the initial state of the collision. The results of the multiplicity analysis of the muon production from $W^{\pm}$ boson decays was then summarized in Table 4, by listing all the obtained linear-fit parameters of the different considered conditions for the multiplicity observable of interest.

Finally, a first look at the experimental detector effects was presented in section 4.4.1 - using O^2 simulations to include the transport of the particles through the detector. From this, it was seen that the ALICE muon spectrometer will not successfully reconstruct all of the simulated muons from $W^{\pm}$ boson decays - which indicates that the detector has a non-negligible reconstruction efficiency. It was also seen that the transverse-momentum resolution distributions have a non-zero width, indicating that there is also a non-negligible uncertainty on the measured p_T of the successfully reconstructed muon tracks. Using an approximated efficiency and the integrated luminosity of the collected Run 3 proton-proton reference data in ALICE, an initial estimation of the expected $W \to \mu$ statistics in the forward region was presented in Figure 46. From this, it was argued that the estimated statistics are adequate to determine the $W \to \mu$ cross-section, but it is most likely not feasible to perform the multiplicity analysis - as further dividing the available statistics into multiplicity bins will result in very large statistical uncertainties. It was then motivated that the available Run 3 lead-lead statistics is on the order of 10^3 times more than the proton-proton reference data, which means that the multiplicity study would be more feasible in this collision system - as well as physically interesting. For future work, it can be meaningful to first obtain the $W^{\pm} \to \mu^{\pm} + \overset{(-)}{\nu}_{\mu}$ cross-section from the proton-proton reference data - where a lot of the technical challenges will most likely arise when trying to find a clean $W^{\pm} \to \mu^{\pm} + \overset{(-)}{\nu}_{\mu}$ signal. After this, a similar feasibility study can be performed for the multiplicity analysis to be done in lead-lead collisions - where the obtained cross-section from the proton-proton reference data can be used as a meaningful baseline measurement. Even though the multiplicity study might not be feasible with the proton-proton reference data at $\sqrt{s} = 5.36$ TeV, it can be feasible to do the study with the Run 3 proton-proton data at $\sqrt{s} = 13.6$ TeV - which also has more statistics available. It might not serve as a direct reference for lead-lead collisions, but is still meaningful as a baseline measurement for the multiplicity dependence.

References

[1] J. Adam et al. “W and Z boson production in p-Pb collisions at $\sqrt{s_{\mathrm{NN}}} = 5.02$ TeV”. In: *Journal of High Energy Physics* 2017.2 (Feb. 2017). ISSN: 1029-8479. DOI: `10.1007/jhep02(2017)077`. URL: `http://dx.doi.org/10.1007/JHEP02(2017)077`.

[2] ALICE Collaboration. *Recorded integrated luminosity in pp reference run @ 5.36 TeV in 2024*. ALICE Figure Repository (ID: ALI-PERF-588550). Accessed: 2025-02-04. 2024.

[3] Mark Thomsom. “Modern Particle Physics”. en. In: *Contemporary Physics* 55.3 (July 2014), pp. 251–252. ISSN: 0010-7514, 1366-5812. DOI: `10.1080/00107514.2014.907354`.

[4] CERN. *The Standard Model*. en. Oct. 2024. URL: `https://home.cern/science/physics/standard-model` (visited on 10/03/2024).

[5] Natalie Wolchover +2 authors Samuel Velasco Lucy Reading-Ikkanda. *A New Map of All the Particles and Forces*. en. Oct. 2020. URL: `https://www.quantamagazine.org/a-new-map-of-the-standard-model-of-particle-physics-20201022/` (visited on 12/16/2024).

[6] ALICE Collaboration. “The ALICE experiment: a journey through QCD”. In: *The European Physical Journal C* 84.8 (Aug. 2024). ISSN: 1434-6052. DOI: `10.1140/epjc/s10052-024-12935-y`. URL: `http://dx.doi.org/10.1140/epjc/s10052-024-12935-y`.

[7] *The Nobel Prize in Physics 1979*. en-US. URL: `https://www.nobelprize.org/prizes/physics/1979/summary/` (visited on 10/03/2024).

[8] CERN. *Four decades of gluons*. en. Oct. 2024. URL: `https://home.cern/news/news/physics/four-decades-gluons` (visited on 10/03/2024).

[9] CERN. *The Higgs boson*. en. Oct. 2024. URL: `https://home.cern/science/physics/higgs-boson` (visited on 10/03/2024).

[10] *The Nobel Prize in Physics 2013*. en-US. URL: `https://www.nobelprize.org/prizes/physics/2013/summary/` (visited on 10/03/2024).

[11] CERN. *W boson: Sunshine and stardust*. en. Oct. 2024. URL: `https://home.cern/science/physics/w-boson-sunshine-and-stardust` (visited on 10/03/2024).

[12] E. M. Riordan. “The Discovery of quarks”. In: *Science* 256 (1992), pp. 1287–1293. DOI: `10.1126/science.256.5061.1287`.

[13] H. W. Kendall. “Deep inelastic scattering: Experiments on the proton and the observation of scaling”. In: (1993). Ed. by T. Fraengsmyr and G. Ekspong, pp. 676–708.

[14] CERN. *The Large Hadron Collider*. en. Oct. 2024. URL: `https://home.web.cern.ch/science/accelerators/large-hadron-collider` (visited on 10/29/2024).

[15] *ATLAS*. en. Oct. 2024. URL: `https://home.cern/science/experiments/atlas` (visited on 10/30/2024).

[16] *LHCb*. en. Oct. 2024. URL: `https://home.cern/science/experiments/lhcb` (visited on 10/30/2024).

[17] *ALICE*. en. Oct. 2024. URL: `https://www.home.cern/science/experiments/alice` (visited on 10/30/2024).

[18] *The Large Electron-Positron Collider*. en. Oct. 2024. URL: `https://home.cern/science/accelerators/large-electron-positron-collider` (visited on 10/31/2024).

[19] Christian Bierlich et al. *A comprehensive guide to the physics and usage of PYTHIA 8.3*. 2022. arXiv: `2203.11601 [hep-ph]`. URL: `https://arxiv.org/abs/2203.11601`.

[20] Deepak Kar. *Experimental Particle Physics*. 2053-2563. IOP Publishing, 2019. ISBN: 978-0-7503-2112-9. DOI: `10.1088/2053-2563/ab1be6`. URL: `https://dx.doi.org/10.1088/2053-2563/ab1be6`.

[21] Simon White et al. “First Luminosity Scans in the LHC”. In: *Conf. Proc. C* 100523 (2010). Ed. by Akira Noda et al., MOPEC014.

[22] S. G. Weber et al. “Elucidating the multiplicity dependence of J/ψ production in proton–proton collisions with PYTHIA8”. In: *The European Physical Journal C* 79.1 (Jan. 2019). ISSN: 1434-6052. DOI: `10.1140/epjc/s10052-018-6531-4`. URL: `http://dx.doi.org/10.1140/epjc/s10052-018-6531-4`.

[23] "The ALICE definition of primary particles". In: (2017). URL: `https://cds.cern.ch/record/2270008`.

[24] ALICE Collaboration. "Multiplicity dependence of charged-particle jet production in pp collisions atm$\sqrt{s} = 13\ TeV$". In: *The European Physical Journal C* 82.6 (June 2022). ISSN: 1434-6052. DOI: `10.1140/epjc/s10052-022-10405-x`. URL: `http://dx.doi.org/10.1140/epjc/s10052-022-10405-x`.

[25] E. Norrbin and T. Sjöstrand. "Production and hadronization of heavy quarks". In: *The European Physical Journal C* 17.1 (Oct. 2000), pp. 137–161. ISSN: 1434-6052. DOI: `10.1007/s100520000460`. URL: `http://dx.doi.org/10.1007/s100520000460`.

[26] S. Navas et al. "Review of particle physics". In: *Phys. Rev. D* 110.3 (2024), p. 030001. DOI: `10.1103/PhysRevD.110.030001`.

[27] ALICE Collaboration. "Production of muons from heavy-flavour hadron decays in pp collisions at $\sqrt{s}$ = 5.02 TeV". In: *Journal of High Energy Physics* 2019.9 (Sept. 2019). ISSN: 1029-8479. DOI: `10.1007/jhep09(2019)008`. URL: `http://dx.doi.org/10.1007/JHEP09(2019)008`.

[28] A.D. Martin et al. "Parton distributions and the LHC: W and Z production". In: *The European Physical Journal C* 14.1 (May 2000), pp. 133–145. ISSN: 1434-6052. DOI: `10.1007/s100520000324`. URL: `http://dx.doi.org/10.1007/s100520000324`.

[29] Shingo Sakai for the ALICE collaboration. "Electroweak vector-boson production in hadronic collisions with ALICE". 12th International Conference on Hard and Electromagnetic Probes of High-Energy Nuclear Collisions. 2024. URL: `https://indico.cern.ch/event/1339555/contributions/6040900/`.

[30] ALICE Collaboration. "ALICE upgrades during the LHC Long Shutdown 2". In: *Journal of Instrumentation* 19.05 (May 2024), P05062. ISSN: 1748-0221. DOI: `10.1088/1748-0221/19/05/p05062`. URL: `http://dx.doi.org/10.1088/1748-0221/19/05/P05062`.

[31] Rita Sadek Finot. "MFT commissioning and preparation for Run 3 data analysis with ALICE (LHC, CERN)". Theses. Ecole nationale supérieure Mines-Télécom Atlantique, Oct. 2022. URL: `https://theses.hal.science/tel-04008085`.

[32] David J Griffiths. *Introduction to elementary particles; 2nd rev. version*. Physics textbook. New York, NY: Wiley, 2008. URL: `https://cds.cern.ch/record/111880`.

[33] CMS Collaboration. *High-precision measurement of the W boson mass with the CMS experiment at the LHC*. 2024. arXiv: `2412.13872 [hep-ex]`. URL: `https://arxiv.org/abs/2412.13872`.

[34] M. Awramik et al. "Precise Prediction for the W Boson Mass in the Standard Model". In: *Phys. Rev. D* 69 (2004), p. 053006. DOI: `10.1103/PhysRevD.69.053006`. arXiv: `hep-ph/0311148`.

[35] Richard D. Ball et al. "Parton distributions with LHC data". In: *Nuclear Physics B* 867.2 (Feb. 2013), pp. 244–289. ISSN: 0550-3213. DOI: `10.1016/j.nuclphysb.2012.10.003`. URL: `http://dx.doi.org/10.1016/j.nuclphysb.2012.10.003`.

[36] P. Skands, S. Carrazza, and J. Rojo. "Tuning PYTHIA 8.1: the Monash 2013 tune". In: *The European Physical Journal C* 74.8 (Aug. 2014). ISSN: 1434-6052. DOI: `10.1140/epjc/s10052-014-3024-y`. URL: `http://dx.doi.org/10.1140/epjc/s10052-014-3024-y`.

[37] Simone Alioli et al. "A general framework for implementing NLO calculations in shower Monte Carlo programs: the POWHEG BOX". In: *Journal of High Energy Physics* 2010.6 (June 2010). ISSN: 1029-8479. DOI: `10.1007/jhep06(2010)043`. URL: `http://dx.doi.org/10.1007/JHEP06(2010)043`.

[38] Stefano Frixione, Paolo Nason, and Carlo Oleari. "Matching NLO QCD computations with parton shower simulations: the POWHEG method". In: *Journal of High Energy Physics* 2007.11 (Nov. 2007), pp. 070–070. ISSN: 1029-8479. DOI: `10.1088/1126-6708/2007/11/070`. URL: `http://dx.doi.org/10.1088/1126-6708/2007/11/070`.

[39] Andy Buckley et al. "LHAPDF6: parton density access in the LHC precision era". In: *The European Physical Journal C* 75.3 (Mar. 2015). ISSN: 1434-6052. DOI: `10.1140/epjc/s10052-015-3318-8`. URL: `http://dx.doi.org/10.1140/epjc/s10052-015-3318-8`.

[40] P Buncic, M Krzewicki, and P Vande Vyvre. *Technical Design Report for the Upgrade of the Online-Offline Computing System*. Tech. rep. 2015. URL: `https://cds.cern.ch/record/2011297`.

[41] S. Agostinelli et al. "GEANT4 - A Simulation Toolkit". In: *Nucl. Instrum. Meth. A* 506 (2003), pp. 250–303. DOI: `10.1016/S0168-9002(03)01368-8`.

[42] University of Cape Town, Timothy Carr, and Andrew Lewis. *UCT HPC Facility*. Oct. 2023. DOI: `10.5281/zenodo.10021613`. URL: `https://doi.org/10.5281/zenodo.10021613`.

[43] Claude A. Pruneau. *Data Analysis Techniques for Physical Scientists*. Cambridge University Press, 2017.

[44] CERN. *Histograms*. en. Oct. 2024. URL: `https://root.cern/manual/histograms/` (visited on 10/03/2024).

[45] Eva Sicking for the ALICE Collaboration. *Minimum Bias Measurements with ALICE at the LHC*. 2012. arXiv: `1209.4729 [hep-ex]`. URL: `https://arxiv.org/abs/1209.4729`.

[46] Z. Conesa del Valle. "Electroweak boson detection in the ALICE muon spectrometer". In: *The European Physical Journal C* 49.1 (Nov. 2006), pp. 149–154. ISSN: 1434-6052. DOI: `10.1140/epjc/s10052-006-0110-9`. URL: `http://dx.doi.org/10.1140/epjc/s10052-006-0110-9`.

6 Appendix A

6.1 Matrix Amplitude

As already mentioned, the matrix amplitude M can be calculated from the Feynman rules that are derived separately from the symmetries for each QFT of interest. It will not be in the scope of this work to go into the technical details of how the Feynman rules are explicitly derived for each fundamental force, but rather just to briefly discuss how they are implemented to calculate the matrix amplitude of interest. As well as discussing the resulting physics implications of the derived rules for the electroweak interaction and quantum chromo-dynamics in the next sections. With this goal in mind, a simpler unphysical "toy" theory (as presented in [32]) will be considered first as an example, to give an overview of how the Feynman rules are applied. This theory will consist of having only three spin-0 particles (where each is its own anti-particle), labelled as A, B and C with masses m_A, m_B and m_C; and only one interaction vertex. It will also be assumed that A is heavier than B and C combined, so that it can decay into them while still conserving energy. The general method of calculating M from the Feynman diagrams for the toy theory can then be summarized with the following steps [32]:

1. **Notation**: Firstly label the incoming and outgoing four-momenta (p_i), as well as the internal momenta (q_j). Also give each line an arrow to indicate the direction in time, where it is arbitrary for internal lines.

2. **Vertex factors**: There is a factor of $-ig$ associated with each vertex, where g is the coupling constant as described in section 1.3.1.

3. **Propagators**: There is a factor of $\frac{i}{q_j^2 - m_j^2 c^2}$ associated with each internal line, where m_j is the mass of the particle represented by the internal line.

4. **Energy/momentum conservation**: In order to impose conservation of energy/momentum, there is a delta function of the form $(2\pi)^4 \delta^4(k_1 + k_2 + k_3)$ associated with each vertex. The k_i terms represent the four-momenta of the incoming/outgoing lines of the vertex, where the sign will be positive/negative depending on whether the line is incoming/outgoing respectively.

5. **Integration**: There is another factor of $\frac{1}{(2\pi)^4} d^4 q_j$ associated with each internal line, after which the integration over all internal momenta can be performed.

6. **Collapse the delta function**: Now the delta-function that was included to conserve energy/momentum at each vertex can be collapsed, and the result then multiplied by i to finally obtain M.

Now that the steps to calculate M have been laid out, it is possible to consider the example of $A + A \rightarrow B + B$ scattering within the toy theory. The Feynman diagrams for the lowest order contributions, for which there are only two time-orderings, are given in Figure 13 - the notation from step 1 in the method has already been applied in the diagrams. Considering only the left diagram and applying steps 2-4, the following result is obtained:

$$-iM_1 = -i(2\pi)^4 g^2 \int \frac{1}{q^2 - m_C^2 c^2} \delta^4(p_1 - p_3 - q) \delta^4(p_2 + q - p_4) d^4 q. \tag{26}$$

Now steps 5-6 can be applied, where the integral will be performed and the delta function collapsed to obtain the result for M from the left diagram as,

$$M_1 = \frac{g^2}{(p_4 - p_2)^2 - m_C^2 c^2}. \tag{27}$$

Figure 47: First-order Feynman diagrams for the $A + A \to B + B$ scattering process in the toy theory [32].

The exact same procedure can then be followed for the diagram on the right to compute M_2, from which the total amplitude can then be obtained as the sum of the two contributions as,

$$M = M_1 + M_2 = \frac{g^2}{(p_4 - p_2)^2 - m_C^2 c^2} + \frac{g^2}{(p_3 - p_2)^2 - m_C^2 c^2}. \tag{28}$$

It is important to note that M will always be Lorentz-invariant, as this property is already built into the Feynman rules being applied [32]. Considering the centre-of-mass frame and the simplification that $m_A = m_B = m$ and $m_C = 0$, the result can be simplified to

$$M = -\frac{g^2}{\mathbf{p}^2 \sin^2 \theta} \tag{29}$$

where $\mathbf{p}$ is the incident momentum of p_1, and θ is the scattering angle between the incident p_2 and outgoing p_3 particles. For this first-order process it is clear that $M \propto g^2$, and that more factors of g will be picked up from Rule 2 for higher orders. When g is small, this makes it clear that higher-order processes will contribute less and less; making low-order calculations good approximations for the total amplitude in many cases. This simplified result can then be plugged into equation (5) to obtain the final differential cross-section for the scattering process as,

$$\frac{d\sigma}{d\Omega} = \frac{1}{2} \left(\frac{\hbar c g^2}{16\pi E \mathbf{p}^2 \sin^2 \theta} \right)^2 \tag{30}$$

where $S = 1/2$ has been substituted for the two identical particles in the final-state. This final result already serves as a stepping-stone for a theoretical prediction in a form that can be compared to experimental data, as explained in section 1.1.3. In section 1.4, it will then be elaborated how the theoretically calculated differential cross-section can be used as input in the context of modelling proton-proton collisions.

6.2 Dirac Spinors

The introduction of spin into the required theory adds additional complexities that were not accounted for in the simplified example presented in section 6.1. Thus, in the coming sections of physical theories where the particles will have the property of spin, it is required to represent the wavefunction of the interacting particles as Dirac Spinors. These are derived as a result of requiring the quantum mechanical wavefunction to be Lorentz invariant and to satisfy the Dirac equation [3]. Even though the details op Dirac spinors will not be discussed in this work, it is important to briefly mention the definition of the probability density and current within the Dirac formalism for the coming sections.

In the Dirac formalism, the wavefunction (ψ) is represented as a four-component spinor as

$$\psi = \begin{pmatrix} \psi_1 \\ \psi_2 \\ \psi_3 \\ \psi_4 \end{pmatrix}, \tag{31}$$

where the Dirac Hamiltonian is then a 4×4 matrix of operators that acts on it. The probability density (ρ) and current ($\mathbf{j}$) is then given as

$$\rho = \psi^\dagger \psi, \tag{32}$$

$$\mathbf{j} = \psi^\dagger \boldsymbol{\alpha} \psi, \tag{33}$$

where the components of $\boldsymbol{\alpha}$ are Hermitian matrices of even dimension and zero trace - which contain the Pauli spin-matrices within the Dirac-Pauli representation. By then considering the covariant form of the Dirac equation, the four-vector current can be represented as

$$j^\mu = (\rho, \mathbf{j}) = \psi^\dagger \gamma^0 \gamma^\mu \psi, \tag{34}$$

where μ is the usual Lorentz index of the relevant four-vector and the γ-matrices are analogous to the components of $\boldsymbol{\alpha}$. Within the Dirac formalism, it can then be shown that the four-component spinors naturally describe the intrinsic angular momentum of spin-half particles [3]. The additional details of dealing with spin-1 particles, such as the $W^\pm$ boson, will not be discussed in this work. For the theories that represent physical particles in the following sections, the spinor four-vector currents will be labelled with $u(p)/v(p)$ and $\bar{u}(p)/\bar{v}(p)$ for the hermitian conjugates, where p will represent the four-momenta of the relevant particle.

7 Appendix B

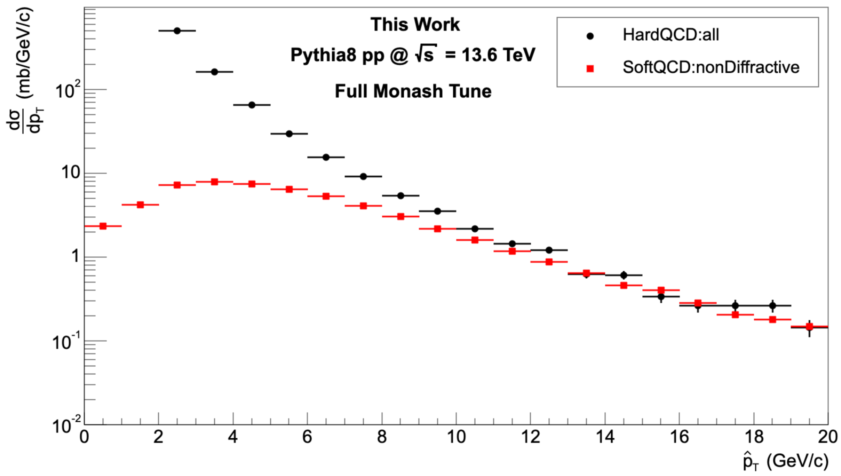

Figure 48: The $\hat{p}_T$-differential cross-section of the soft (non-diffractive) and hard QCD processes in Pythia at $\sqrt{s} = 13.6$ TeV.

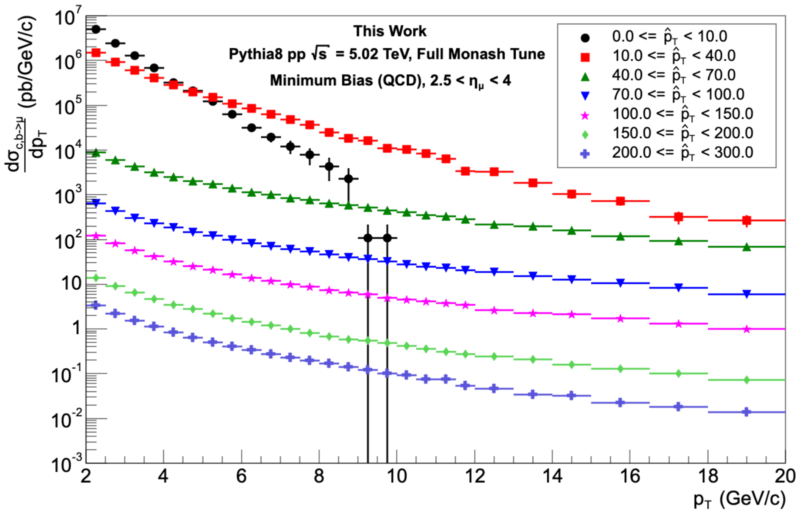

Figure 49: The $\hat{p_T}$-bin contributions to the production of HF→ μ in the forward η-region of proton-proton collisions, at $\sqrt{s} = 5.02$ TeV with Pythia.

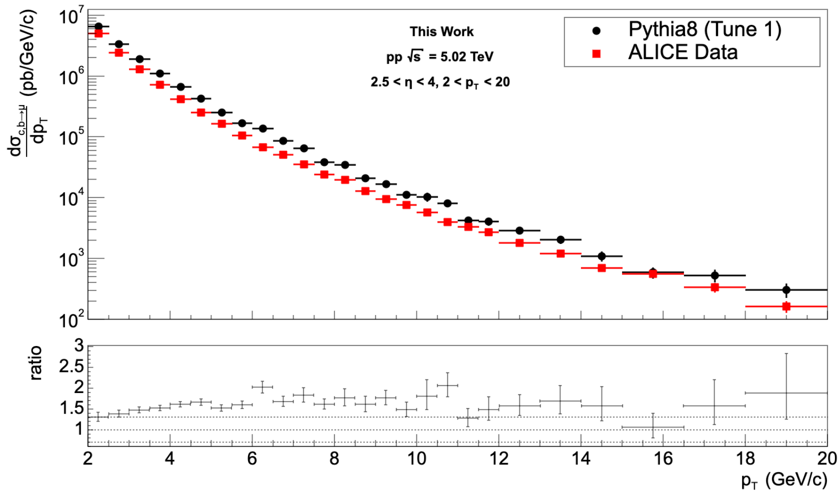

Figure 50: The p_T-differential cross-section of HF→ μ in the forward region of proton-proton collisions at $\sqrt{s} = 5.02$ TeV with Pythia (Tune 1), compared to the experimentally published results by ALICE [27]